UCLA
UCLA Electronic Theses and Dissertations

Title

Control and Optimization of Light Transfer in Photobioreactors Used for Biofuel Production

Permalink

Author

Kandilian, Razmig

Publication Date

2014

Peer reviewed|Thesis/dissertation

UNIVERSITY OF CALIFORNIA

Los Angeles

Control and Optimization of Light Transfer in Photobioreactors Used for Biofuel Production

A dissertation submitted in partial satisfaction

of the requirements for the degree

Doctor of Philosophy in Mechanical Engineering

by

Razmig Kandilian

2014

ABSTRACT OF THE DISSERTATION

Control and Optimization of Light Transfer in Photobioreactors Used for Biofuel Production

by

Razmig Kandilian

Doctor of Philosophy in Mechanical Engineering

University of California, Los Angeles, 2014

Professor Laurent G. Pilon, Chair

Microalgae are tipped as the feedstock for next generation transportation fuels due to their significantly higher photosynthetic efficiency compared to higher plants. These microorganisms can contain large amounts of triglyceride fatty-acids (TG-FAs) that can be converted to biodiesel by transesterification. However, microalgae cultivation in photobioreactors (PBRs) typically suffers from low productivity due to light transfer limitations. To optimize microalgae growth rate and productivity, radiation transfer analysis must be performed in order to optimize light availability in PBRs. Nitrogen starvation coupled with strong illumination has been used to induce large amounts of TG-FA accumulation in microalgae. However, the role of light absorption rate by the microalgae cells on TG-FA productivity is not well understood. This study aims (1) to study the interaction between light and photosynthetic microorganisms and (2) to optimize light transfer conditions in PBRs to maximize microalgal biomass and lipid productivity.

First, the complete set of radiation characteristics and optical properties of the eustegmatophycea *Nannochloropsis oculata*, a promising marine microalgae for biodiesel production, was obtained for cells grown under various light spectra and irradiances. Second, the radiation characteristics of aggregates and colonies of microalgae were studied theoretically. Significant differences were observed in the average absorption and scattering cross-sections of cells either free-floating or aggregated in colonies. Third, a feed-forward inversion control

scheme was designed and experimentally demonstrated for maintaining an optimum incident irradiance on PBRs during batch cultivation. A data-based model-free optimization was utilized to rapidly estimate the optimum average fluence rate set-point value leading to maximum microalgae growth rate. This control scheme increased biomass productivity and reduced lag time compared to batch cultures exposed to constant irradiance throughout the cultivation process. Finally, *N. oculata* were grown under nitrogen starvation conditions and were characterized in terms of their biomass, pigment, and TG-FA concentrations as well as their absorption and scattering cross-sections as a function of time for several batch cultures. The TG-FA production rate correlated to the rate of photon absorption by cells suggesting that the TG-FA production process was limited by light.

The dissertation of Razmig Kandilian is approved.

Chih-Ming Ho

Jennifer Ayla Jay

Jérémy Pruvost

Tsu-Chin Tsao

Laurent G. Pilon, Committee Chair

University of California, Los Angeles

2014

TABLE OF CONTENTS

LIST OF TABLES

a	monomer radius, μm
$<\mathscr{A}>$	mean volumetric rate of energy absorption, μmol$_{h\nu}$/g·s
$\bar{A}_{abs}$	average mass absorption cross-section, m^2/kg
$\bar{A}_p$	aggregate average projected area
b_λ	backward scattering ratio
c	pigment concentration, kg/m^3
$\bar{C}_{abs}$	average absorption cross-section, m^2
$\bar{C}_{ext}$	average extinction cross-section, m^2
$\bar{C}_{sca}$	average scattering cross-section, m^2
$\langle C^a_{abs} \rangle$	orientation averaged aggregate absorption cross-section, μm^2
$\langle C^a_{ext} \rangle$	orientation averaged aggregate extinction cross-section, μm^2
$\langle C^a_{sca} \rangle$	orientation averaged aggregate scattering cross-section, μm^2
D_f	fractal dimension
d_s	equivalent sphere diameter, μm
Ea	*in vivo* pigment specific absorption cross-section, m^2/kg
$[F(\Theta)]$	Stokes matrix
f	number frequency distribution
G_{in}	incident irradiance, μmol$_{h\nu}$/m^2·s
G	fluence rate, μmol$_{h\nu}$/m^2·s
g_λ	Henyey-Greenstein asymmetry factor
I	radiation intensity, W/m^2·nm·sr
k	absorption index
k_f	fractal prefactor
L	PBR thickness, cm
l	cuvette pathlength, cm
m	relative complex index of refraction

N_λ	normalized spectral distribution of light source
n	refractive index
N_s	number of monomers per aggregate
N_T	cell number density, cells/m^3
p	cell size distribution
P_v	volumetric productivity, kg/m^3·day
q	scattering wave vector, m^{-1}
Q_{abs}	absorption efficiency factor
$\langle Q^a_{abs} \rangle$	orientation averaged aggregate absorption efficiency factor
Q_{sca}	scattering efficiency factor
$\langle Q^a_{sca} \rangle$	orientation averaged aggregate scattering efficiency factor
R	areal TG-FA productivity, kg/m^2·day
$\mathbf{r}$	location vector, m
R_g	radius of gyration, μm
$\hat{s}$	direction vector
$\bar{S}_{sca}$	average mass scattering cross-section, m^2/kg
$S(qR_g)$	aggregate structure factor
T	transmittance
t	time, hours
X	biomass concentration, kg/m^3
V	microalgae sample volume, m^3
v	volume of solvent, m^3
V_{ctrl}	voltage supplied to the LED controller, V
V_{out}	voltage output of the concentration sensor amplifier, V
V_T	aggregate total volume, μm^3
w	pigment mass fraction
$[Z(\Theta)]$	Mueller matrix
z	PBR depth coordinate, cm

Greek symbols

β	extinction coefficient, m^{-1}
κ	absorption coefficient, m^{-1}
χ_s	monomer size parameter
ϵ	spectrometer correction factor
λ	wavelength, nm
Ω	solid angle, sr
Φ_λ	scattering phase function
μ	microorganisms specific growth rate, h^{-1}
σ_s	single scattering coefficient, m^{-1}
Θ	scattering angle, degrees
τ	batch cultivation duration, days
ξ	apparent extinction coefficient, m^{-1}
ζ	cell aspect ratio

Subscripts

0	initial
avg	refers to average
cr	critical
f	final
h	normal-hemispherical
i	inner radius
inc	incident
n	normal-normal
o	outer radius
sca	scattered
$V + \bar{A}_p$	volume and average projected area equivalent

$x + c$ xanthophylls and carotenes

Acronyms and abbreviations

ASW   artificial sea water

chl$a$ chlorophyll a

OD   optical density

PAR   Photosynthetically active radiation

PBR   photobioreactor

PPC   photoprotective carotenoids

PS I   Photosystem I

PS II   Photosystem II

RDG   Rayleigh-Debye-Ganz

TG-FA   triglyceride fatty acid

Vita

2009	B.S., Mechanical Engineering, Summa Cum Laude
	University of California Los Angeles
	Los Angeles, CA
2011	M.S., Mechanical Engineering
	University of California Los Angeles
	Los Angeles, CA

PUBLICATIONS AND PRESENTATIONS

R. Kandilian, A Navid, L Pilon, The pyroelectric energy harvesting capabilities of PMNPT near the morphotropic phase boundary, Smart Materials and Structures, Volume 20, Issue 5, 055020, 2011. DOI:10.1088/0964-1726/20/5/055020.

L. Pilon, H. Berberoğlu, R. Kandilian, Radiation transfer in photobiological carbon dioxide fixation and fuel production by microalgae, Journal of Quantitative Spectroscopy and Radiative Transfer, Volume 112, Issue 17, Pages 2639-2660, 2011. DOI:10.1016/j.jqsrt.2011.07.004.

I.M. McKinley, R. Kandilian and L. Pilon, Waste heat energy harvesting using the Olsen cycle on $0.945Pb(Zn_{1/3}Nb_{2/3})O_3 0.055PbTiO_3$ single crystals, Volume 21, Issue 3, 035015, 2012. DOI:10.1088/0964-1726/21/3/035015.

R. Kandilian, E. Lee, L. Pilon, Radiation and optical properties of *Nannochloropsis oculata*

grown under different irradiances and spectra, Bioresource Technology, Volume 137, Pages 63-73, 2013.DOI:10.1016/j.biortech.2013.03.058.

R. Kandilian, J. Pruvost, J. Legrand, L. Pilon, Influence of light absorption rate by *Nannochloropsis oculata* on triglyceride production during nitrogen starvation, Bioresource Technology, Volume 163, Pages 308-319, 2014. DOI:10.1016/j.biortech.2014.04.045.

R. Kandilian, T.-C. Tsao, L. Pilon, Control of incident irradiance on a batch operated flat-plate Photobioreactor, Chemical Engineering Science, Volume 119, Pages 99-108, 2014. DOI:10.1016/j.ces.2014.07.056.

R. Kandilian, J. Pruvost, J. Legrand, L. Pilon, Optimization of triglyceride production with respect to light using *Nannochlorpsis oculata*, The 4th International Conference on Algal Biomass, Biofuels and Bioproducts, 1518 June, 2014, Santa Fe, New Mexico, USA.

CHAPTER 1

Introduction

This chapter presents the motivations and background of this study. First, it discusses energy production in the United States as well as transportation fuel use. Then it presents common methods of producing biomass and converting it to biofuels. Basics of microalgae photosynthesis and radiation transport in photobioreactors are presented. This chapter concludes with the objectives of this study and the scope of the document.

1.1   Motivations

The ever increasing demand for energy combined with concerns over the long term availability and environmental damage caused by fossil fuels has forced societies to seek alternative and sustainable fuel production. Over the last five decades, world population has more than doubled and it is projected to increase by an additional 1.4 billion people by the year 2035 [1]. Figure 1.1 shows the historical trend in energy consumption and CO_2 consumption over the last fifty years and their future projections [1]. Energy demand and CO_2 emissions are projected to increase by 41% and 29%, respectively [1]. Solar radiation supplies the planet with 2,850 PW of energy. Yet, according to the United States Energy Information Administration, renewable energy accounted for only 11% of the total energy generated in the United States in 2013 [2]. Biomass was the source of approximately 49% of all renewable energy production in the U.S. that year. The remaining came from wind (17%), solar thermal and photovoltaic (3.4%), geothermal (2.4%), and hydrothermal (28%). In 2009, transportation was responsible for 29% of the total energy consumption in the United States with approximately 80% of it due to terrestrial transportation. Worldwide use of
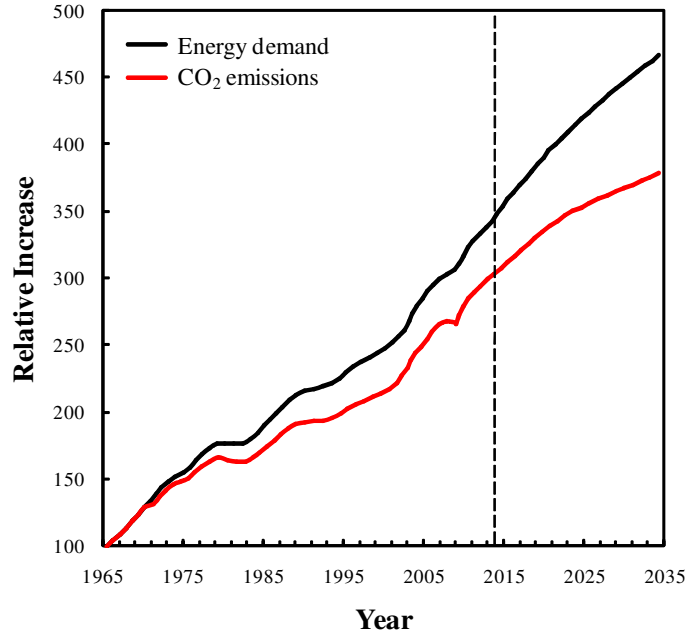
Figure 1.1: Historical trend in energy consumption and CO_2 consumption and their future projections [1].

liquid fuel is projected to rise by 19 million barrels per day in 2035 primarily due to the transportation sector. Despite the introduction of electric cars, the high energy density and ease of storage, liquid petroleum remains difficult to replace by any other commercially available energy source. The vast majority of the petroleum is supplied by fossil fuels which has led to pollution and climate change [3]. Liquid biofuels produced by photosynthetic microorganisms may be one of the renewable energy source that satisfies the transportation fuel needs of the future. Therefore, the Energy Independence and Security Act (EISA) of 2007 established the renewable fuel standards mandating 36 billion gallons of renewable biofuels to be blended with transportation fuels sold in the U.S. by year 2022 [4].

1.2 History of biofuels in the United States

First-generation biofuels were produced by fermentation of sugar, starch, or cellulose to produce ethanol, propanol, and butanol [5]. These use human and animal feed as a feedstock

for biofuel in addition to being unsustainable if mass produced. Therefore, they have been superseded by second-generation biofuels that use soybean, canola, palm, jatropha, corn, as well as waste cooking oil as the feedstock to produce biofuels such as biodiesel. The use of these plants to produce fuels proved controversial due to the use of food crops, freshwater, and large areas of arable land to produce fuels [5]. Table 1.1 shows the potential oil production capacity of various agricultural crops. The best agricultural crop, the palm oil, can yield a maximum of 641 gallons of oil per acre per year. An arable land three times as large as that available in the U.S. is necessary to produce the 220 billion gallon of transportation fuel the country uses yearly using palm oil. Moreover, 30% of the corn grown in the U.S. is used for ethanol production. In excess of 100% of the corn produced in the U.S. must be converted to biofuels to produce the 36 billion gallons of ethanol to meet the 2022 EISA federal mandates. Therefore, at most 15 of the 36 billion gallons of biofuels mandated by EISA are allowed to be bioethanol. The remainder is projected to come from microalgae-based biodiesel [4].

Recent life cycle analysis (LCA) suggests that CO_2 emissions bioethanol produced from corn falls short of the U.S. legislative mandate of 60% reduction in green-house gas (GHG) emission compared to gasoline [6]. LCA analysis by Liu *et al.* [7] demonstrated that microalgae derived biodiesel has significantly lower GHG emission than both bioethanol and petroleum diesel. However, it has an energy return on investment between 1 and 3 which is much lower than petroleum fuels [7]. Microalgae feature productivity ten times larger than higher plants and they can be cultivated in waste-water as well as on arid-land.

These single cell organisms use solar radiation to convert CO_2 to biomass with efficiency 10 to 100 times larger than that of higher plants [5, 8–10]. Figure 1.2 presents a schematic showing the various inputs and outputs of photosynthetic microorganisms. Microalgae use water as their electron source, sunlight as their energy source, and CO_2 as their inorganic carbon source and produce oxygen, starch, carbohydrates, and lipids [10]. Microalgae such as *Chlamydomonas reinhardtii* and cyanobacteria such as *Anabaena variabilis* are also capable of producing hydrogen [11, 12]. This hydrogen gas can be used to generate electricity using electrochemical cells for stationary or mobile applications [8, 13].

Table 1.1: Oil productivity of various agricultural crops [5].

Crop	Gallons of oil/acre/year
Soybeans	43
Sunflower	86
Canola	171
Jatropha	214
Palm oil	641
Microalgae	6,000-10,000
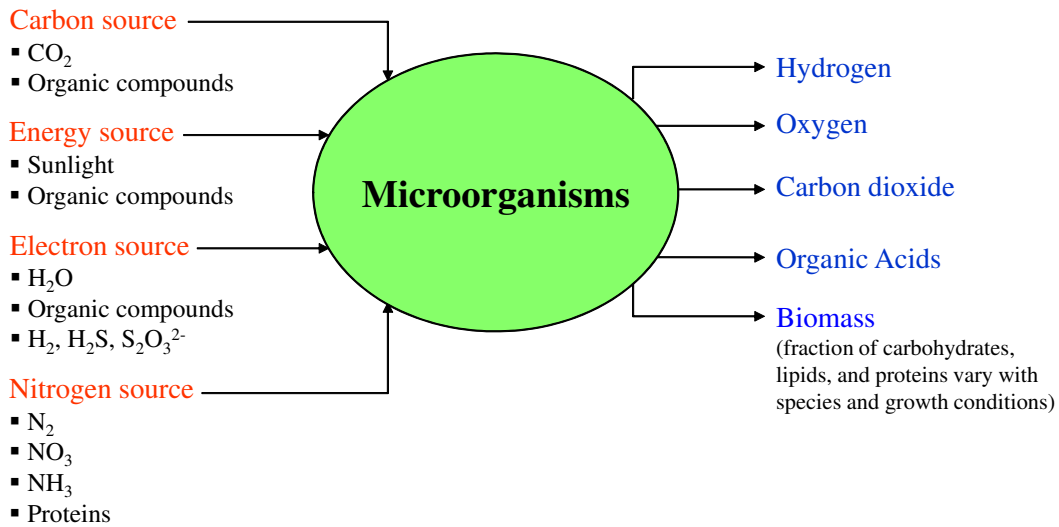
Figure 1.2: Schematic of input and output of photosynthetic microorganisms consuming CO_2 and producing biofuels and biomass.

Some species such as the marine eustigmatophyceae *Nannochloropsis oculata* and the green microalgae *Botryococcus braunii* can contain up to 30 to 70% lipids by dry weight [14, 15]. Microalgal lipids can be extracted from the organisms and converted to biodiesel. For example, triglycerides can be transesterified with short chain alcohols such as methanol and fatty acids can be esterified. The remaining biomass can be fermented to produce biogas or sold as a fertilizer as it is rich in both phosphate and nitrogen. Alternatively,

Table 1.2: Summary of the major commercial products produced by microalgae and their market value and size [2].

Commercial product	Market size (tons/year)	Sales volume (million USD/year)
Health food	7,000	2,500
Aquaculture	1,000	700
Animal feed additive	NA	300
DHA	<300	1,500
Beta-carotene	1,200	280
Astaxanthin	300	150
Phycocyanin	NA	10
Phycoerytherin	NA	2
Fertilizers	NA	5,000

biomass can be converted to crude petroleum by hydrothermal liquefaction. The latter is a process that exposes the wet biomass, 20 wt.% solids, to elevated temperatures (up to 350°C) and pressures (10-20 MPa) to produce petroleum like oil that has a higher heating value between 35 and 40 MJ/kg. However, the oil produced using hydrothermal liquefaction contains nitrogen and oxygen of up to 11 and 6 wt.%, respectively [16]. This is undesirable as it causes in increased NO_x emission when the produced fuel is burnt [16]. Thus, the oil must be treated and excess oxygen and nitrogen removed [16].

1.3   Value-added products

Microalgae are also sought after for the high value chemicals and pharmaceuticals they can produce. Table 1.2 summarizes various products produced using microalgae and the market size and the value they command. For example, pigments such as astaxanthin and β-carotene are used as colorants or antioxidants in the food and pharmaceutical industries [17]. These

secondary products have a much smaller market size. However, they command prices per mass three to four orders of magnitude larger than biodiesel [17].

1.4   Microalgae cultivation systems

The possibility of using microorganisms to produce biofuels has been touted for decades [18]. However, cost, energy efficiency, and scale up remain major challenges [5, 8, 9, 19]. Photosynthetic microalgae are typically cultivated in open-ponds or enclosed photobioreactors (PBRs) [5, 8].

(a)

(b)
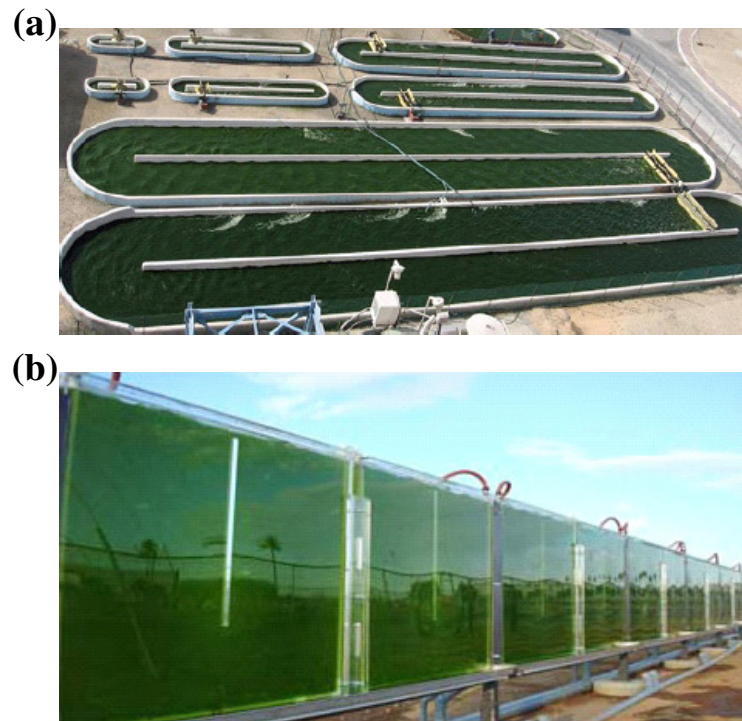
Figure 1.3:   Field demonstration of (a) open-pond PBRs [20] and (b) vertical flat-plate closed PBRs [21].

Figure 1.3 shows examples of open-pond and closed PBRs. Closed PBRs are costly to construct and operate despite being more efficient at converting solar radiation to biomass. On the other hand, open-ponds are more cost effective. However, they suffer from lower

biomass productivity, evaporative loss of water, culture contamination and poor mixing. Currently, it is uneconomical to produce biomass in PBRs exposed to solar radiation. For example, maximum theoretical yield of biodiesel is reported to be 354,000 L/ha·year while actual yields are at best 50,000 L/ha^{-1}yr^{-1} [22]. Similarly, theoretical yields of biomass with lipid mass fraction of 40 dry wt.% is reported to be 0.095 kg/m^2·day while the typical productivity in PBRs in less than 0.025kg/m^2·day [22]. These reductions in biodiesel and biomass productivity are attributed to light limitation in the PBRs [22]. Consequentially, despite its large photosynthetic efficiency, microalgae biodiesel remains approximately three times more expensive to produce than its petroleum counterpart [23]. Chisti [24] determined that the cost of production for biomass composed of 40 dry wt.% lipids must be less than $0.50 for microalgal biodiesel to be economically competitive with $100 per barrel of crude oil. However, current estimates of dry biomass production costs range from $5 to $100 per kilogram [22, 24]. Alternatively, Stephens *et al.* [25] illustrated that biodiesel production by large-scale ($>$ 500 hectare), microalgae production systems may be profitable if they were also used for co-producing high-value products such as acid-hydrolyzed vegetable protein (HVP) or beta-carotene which can be sold for $600/kg. The low productivity of PBRs and the high cost of producing biomass highlight the importance of optimization of PBRs with respect to light.

1.5   Photosynthesis

Photosynthesis is the process that converts light energy into chemical energy in plants, green algae, cyanobacteria, and other photosynthetic microorganisms [10]. Photosynthesis occurs in the thylakoid membrane located inside the chloroplast in the two photosynthetic units called photosystem I (PS I) and photosystem II (PS II) [10]. Both PS I and PS II contain (i) a reaction center carrying out charge separation and electron transport and (ii) antenna featuring pigments responsible for absorbing light. The role of PS II is to split water into protons, oxygen, and electrons. PS I uses the electrons transported from PS II to carry out the redox reactions that result in CO_2 fixation [10]. The two main pigment

molecules responsible for capturing light in photosynthetic green algae are Chlorophylls a and b [10]. The absorbed energy is used to drive reduction of CO_2 and to synthesize hydrocarbon molecules.

Photosynthesis consists of two reactions: a light reaction followed by electron shuttling between the photosystems and a dark reaction [10]. The time scales of the charge separation reactions are in the order of pico- to nanoseconds [10]. Shuttling electrons between the two photosystems takes on the order of micro- to milliseconds [10]. The carbon metabolizing reaction or the dark reaction takes several seconds to complete [10]. In addition, once a photon is absorbed there is a 1 to 15 ms delay before the pigment molecules are ready to accept another photon [10]. The time scale for the various reactions have been illustrated experimentally by exposing various algae to flashes of light lasting microseconds followed by dark periods of up to 40-45 milliseconds. The results established that exposing the microalgae to successive light and dark cycles had efficiency at least as high as when the microalgae were exposed to continuous incident light with the same energy [10, 26].

Exposing microalgae to large irradiance causes photo-oxidative damage in some of the PS II units. This so-called photoinhibition causes a decrease in the photosynthetic efficiency. This is primarily due to the destruction of one of the reaction center proteins, namely the 32 kDa protein D1 [10, 27]. The chloroplast repairs such damage by destroying the affected D1 proteins and synthesizing new ones and integrating them into the affected PS II units. In fact, the cells continuously perform a damage repair cycle to repair the damaged PS II units [27, 28]. However, when the damage rate exceeds the repair rate, inhibition becomes apparent in the cells and the overall efficiency of the cells decreases [10, 27]. In addition, long term exposure to intense light brings about physical changes in the thylakoid membrane such as a reduction in the number of PS I units while maintaining a large number of PS II units. The overall chlorophyll content can also decrease during the growth due to intense incident light. This is sometimes referred to as chlorophyll bleaching [27, 29]. As a result, the photosynthetic rate decreases [10, 27].

1.6   Radiation harvesting pigments

The PS I and PS II require 4 moles of photons of wavelength equal to or smaller than 700 and 680 nm (red), respectively, to fix 1 mole of CO_2 [10]. Chlorophylls (chl) a, b, and c molecules are the primary pigments responsible for absorbing visible photons and transferring the charges to the reaction center. Carotenoids, on the other hand, can be divided into xanthophylls and carotenes [10]. Carotenes are photosynthetic and absorb photons with wavelength corresponding to green and yellow colors and transfer the charges to chlorophyll molecules [10]. Xanthophylls, on the other hand, act to protect the photosynthetic apparatus against excessive light [10]. These photoprotective carotenoids quench poisonous free radicals and convert excess radiant energy into heat [30–32]. *Nannochloropsis oculata* contain the pigments chlorophyll a, β-carotene, and the xanthophylls violaxanthin and vaucherxanthin but lack chlorophyll b [33].

Microalgae experience photoacclimation and chromatic acclimation in response to different incident irradiance and spectrum, respectively [30, 32, 34]. For example, they tend to increase their pigment concentrations in light-limited conditions. However, this may not lead to significant changes in their radiation characteristics as increasing the concentration of chlorophylls also decreases their *in vivo* specific absorption coefficient due to mutual shading of pigment molecules [30]. The latter is partially responsible for what is known as the package effect corresponding to the non-linear relationship between cell pigment concentrations and cell absorption cross-section [35]. In addition, microalgae increase their photoprotective carotenoid concentration in response to large irradiance while reducing the amount of photosynthetic carotenoids through the so-called xanthophyll cycle [30–32]. The latter does not usually lead to changes in the overall carotenoid concentration as changes in the two types of carotenoids compensate each other [30, 31].

Moreover, photoacclimation and chromatic acclimation depend on the microalgae species. Even among *Nannochloropsis* species large difference in pigment expression exists. For example, Gentile and Blanch [32] observed an 80% and 60% decrease in chl$a$ and vioxanthin, respectively, in batch grown *Nannochloropsis gaditana* when the incident irradiance on a

250 ml flask was increased from 70 μmol/m^{2}s to 880 μmol/m^{2}s. Fisher *et al.* [34] found that *Nannochloropsis sp.* grown under 30 μmol/m^{2}s, in continuous cultures, had a steady-state chlorophyll concentration 4.5 times larger than when grown under 650 μmol/m^{2}s. The low light-acclimated cells increased their number of photosynthetic units while the size of individual PSU remained constant. Lubián *et al.* [31] demonstrated that *N. oculata* had lower concentrations of carotenoids canthaxanthin and astaxanthin and larger chlorophyll *a* concentration per cell compared with *N. gaditana* and *N. salina* for cultures grown under the same conditions. The pigment concentrations of *Nannochloropsis sp.* depend also on the PBR thickness and the initial cell concentration [34,36]. Zou and Richmond [36] showed that *Nannochloropsis sp.* had an order of magnitude larger steady-state chl*a* concentration per cell in cultures grown in 3 cm thick PBRs compared with those grown in 1 cm thick PBRs both exposed to 3000 μmol/m^{2}s. However, cells grown in 1 cm thick PBR had a larger carotenoid to chl*a* ratio. In addition, batch cultures of *Nannochloropsis sp.* with low initial cell density experienced a 5 day growth lag time while cultures with high initial cell concentration experienced no lag upon transfer to a PBR exposed to a photon flux density of 3500 μmol/m^{2}s.

1.7 Radiation transfer in photobioreactors

The light utilization efficiency of these PBRs is perhaps the most important parameter affecting the overall efficiency of the biofuel production process. Thus, careful light transfer analysis must be conducted to design, optimize light transport, and operate efficient PBRs for converting solar energy into biofuels using microorganisms [8]. To do so, the spectral radiation characteristics of microalgae are necessary.

Light transfer within absorbing, scattering, and non-emitting microalgal suspension in photobioreactors is governed by the radiative transport equation (RTE) expressed on a spectral basis as [37]

$$\hat{s} \cdot \nabla I_\lambda = -\kappa_\lambda I_\lambda \left(\hat{r}, \hat{s}\right) - \sigma_{s,\lambda} I_\lambda \left(\hat{r}, \hat{s}\right) + \frac{\sigma_{s,\lambda}}{4\pi} \int_{4\pi} I_\lambda \left(\hat{r}, \hat{s}_i\right) \Phi_{T,\lambda} \left(\hat{s}_i, \hat{s}\right) d\Omega_i \qquad (1.1)$$

where $I_\lambda(\hat{r}, \hat{s})$ is the spectral radiation intensity in direction $\hat{s}$ at location $\hat{r}$ (in W/m^2·nm·sr) while κ_λ and $\sigma_{s,\lambda}$ are the effective absorption and scattering coefficients of the suspension (in 1/m). The total scattering phase function of the suspension $\Phi_{T,\lambda}(\hat{s}_i, \hat{s})$ represents the probability that radiation traveling in the solid angle $d\Omega_i$ around direction $\hat{s}_i$ is scattered into the solid angle $d\Omega$ around the direction $\hat{s}$ and is normalized such that

$$\frac{1}{4\pi} \int_{4\pi} \Phi_{T,\lambda}(\hat{s}_i, \hat{s}) \, d\Omega_i = 1. \tag{1.2}$$

The backward scattering ratio, denoted by b_λ, and the Henyey-Greenstein asymmetry factor, denoted by g_λ, for an axisymmetric phase function are defined as [8]

$$b_\lambda = \frac{1}{2} \int_{\pi/2}^{\pi} \Phi_{T,\lambda}(\Theta) \sin\Theta d\Theta \quad \text{and} \quad g_\lambda = \frac{1}{2} \int_0^\pi \Phi_{T,\lambda}(\Theta) \cos\Theta \sin\Theta d\Theta \tag{1.3}$$

where Θ is the scattering angle between directions $\hat{s}_i$ and $\hat{s}$. The effective absorption coefficient κ_λ of a polydisperse microorganism suspension is related to the average absorption cross-sections, denoted by $\bar{C}_{abs,\lambda}$, as [8]

$$\kappa_\lambda = \int_0^\infty C_{abs,\lambda}(d_s) p(d_s) \mathrm{d}d_s = \bar{C}_{abs,\lambda} N_T \tag{1.4}$$

where $p(d_s)$ is the number of cells per unit volume of suspension having diameter between d_s and $d_s + \mathrm{d}d_s$ and $C_{abs,\lambda}(d_s)$ is the absorption cross-section of a single spherical scatterer of diameter d_s. Here, N_T is the cell density defined as the total number of cells per m^3 of suspension. Similarly, the effective scattering coefficient can be written as

$$\sigma_{s,\lambda} = \int_0^\infty C_{sca,\lambda}(d_s) p(d_s) \mathrm{d}d_s = \bar{C}_{sca,\lambda} N_T \tag{1.5}$$

where $C_{sca,\lambda}(d_s)$ is the scattering cross-section of a single spherical scatterer of diameter d_s and $\bar{C}_{sca,\lambda}$ is the average scattering cross-section. Alternatively, the absorption and scattering coefficients can be expressed as the product of the average specific (or mass) absorption and scattering cross-sections $\bar{A}_{abs,\lambda}$ and $\bar{S}_{sca,\lambda}$ (in m^2/kg) and the microorganism mass concentration X (in kg/m^3) so that $\kappa_\lambda = \bar{A}_{abs,\lambda} X$ and $\sigma_{s,\lambda} = \bar{S}_{sca,\lambda} X$. Finally, the extinction coefficient β_λ (in 1/m) is given by $\beta_\lambda = \kappa_\lambda + \sigma_{s,\lambda}$.

The total scattering phase function of polydisperse microalgae cells $\Phi_{T,\lambda}(\Theta)$ can be estimated by averaging the scattering phase function of individual cells of diameter d_s, $\Phi_\lambda(d_s, \Theta)$ according to [37]

$$\Phi_{T,\lambda}(\Theta) = \frac{\displaystyle\int_0^\infty C_{sca,\lambda}(d_s)\Phi_\lambda(d_s,\Theta)p(d_s)\mathrm{d}d_s}{\displaystyle\int_0^\infty C_{sca,\lambda}(d_s)p(d_s)\mathrm{d}d_s} \tag{1.6}$$

Axisymmetric spheroidal microalgae with major and minor diameters a and b can be approximated as spheres with equivalent diameter d_s such that the surface area of the spheroid is equal to that of the equivalent sphere. Then, the equivalent diameter is expressed as [38]

$$d_s = \frac{1}{2}\left(2a^2 + 2ab\frac{sin^{-1}e}{e}\right)^{1/2} \quad \text{where} \quad e = \frac{(\zeta^2-1)^{1/2}}{\zeta}. \tag{1.7}$$

Here, ζ is the spheroid aspect ratio defined as $\zeta = a/b$. The scatterer frequency distribution is denoted by $f(d_s)$ and defined as

$$f(d_s) = \frac{p(d_s)}{\displaystyle\int_0^\infty p(d_s)\mathrm{d}d_s} = \frac{p(d_s)}{N_T}. \tag{1.8}$$

1.8 Objectives of the present study

The objective of this study are to explore novel strategies to increase biomass and lipid productivity by microalgae through optimizing light transfer conditions in PBRs. The tasks to achieve this objective are listed as follows:

1.8.1 Determination of microorganisms radiation characteristics

This study presents the average absorption and scattering cross-sections and the total scattering phase function of *Nannochloropsis oculata* along with their complex index of refraction in the photosynthetically active radiation (PAR) region. It also aimed to assess the dependence of the radiation characteristics on the spectral distribution and the amplitude of the illuminance provided to the PBR during the microalgae growth.

The second objective of the study was to demonstrates that the radiation characteristics of randomly oriented fractal aggregates of monodisperse and polydisperse monomers can be approximated accurately by those of coated spheres with equivalent volume and average projected area. Some microalgae species such as the *Botrycoccus braunii* form colonies and aggregates. The effect of the latter on microalgae suspension absorption and scattering cross-sections has not previously been studies.

1.8.2 Advanced PBR optimization strategies

The third objective was to present a method to identify the optimum average fluence rate in the PBR and to optimize biomass productivity in batch operated PBRs.

The fourth objective of this study was to understand the role of light absorption by the microalgae cells on their lipid accumulation productivity. Illumination was previously identified as the limiting factor in increasing lipid productivity [39]. However, a link between light transfer conditions in the PBR and microalgae lipid or triglyceride productivity was not established.

1.9 Organization of this document

Chapter 2 presents the radiation characteristics and optical properties of marine microalgae *Nannochloropsis oculata* grown under various light spectra and intensities. Chapter 3 establishes an approximate method of predicting the radiation characteristics of microalgae colonies and aggregates. Chapter 4 demonstrates a novel control scheme for optimization of biomass productivity of the microalgae *N. oculata*. Chapter 5 characterizes the effects of light absorption rate by the microalgae *N. oculata* on triglyceride fatty acid productivity. Finally, Chapter 6 summarizes the main contributions of the present study and discusses recommendations and future work.

CHAPTER 2

Radiation and Optical Properties of *Nannochloropsis oculata* Grown Under Different Irradiances and Spectra

This chapter presents the average absorption and scattering cross-sections and the total scattering phase function of *Nannochloropsis oculata* along with their complex index of refraction in the photosynthetically active radiation (PAR) region. It also assesses their dependency on the spectral distribution and the amplitude of the illuminance provided to the PBR during the microalgae growth. The radiation characteristics reported here will be used for radiation transfer analysis and optimization of biomass productivity in Chapter 4.

2.1 Introduction

Bidigare *et al.* [40] and Pottier *et al.* [41] used a predictive method for estimating the spectral absorption coefficient κ_λ by expressing it as a weighted sum of *in vivo* pigment specific absorption cross-sections $Ea_{\lambda,i}$ in (m^2/kg)

$$\kappa_\lambda = \sum_{i=1}^{n} Ea_{\lambda,i} c_i \tag{2.1}$$

where $(c_i)_{1 \leq i \leq n}$ are the mass concentrations (in kg/m^3) of the cell's pigments. The specific absorption coefficient $Ea_{\lambda,i}$ (in m^2/kg) of chl*a*, *b*, and *c*, and β-carotene have been reported in the literature in the spectral range from 400 to 750 nm [42].

Gitelson *et al.* [43] reported the average "specific mass absorption coefficient" (in m^2/kg) of *Nannochloropsis sp.* expressed as the ratio of the absorption coefficient κ_λ to the chloro-

phyll concentration c_{chla}. The authors used high density microalgae cultures with mass concentration X ranging from 1 to 8 kg/m^3 to measure the absorption coefficient in the spectral region from 400 to 750 nm. The microalgae were grown outdoors in 1 to 20 cm thick vertical flat panel photobioreactors using artificial seawater medium. The absorption coefficient κ_λ measurements were performed using an integrating sphere and were corrected for scattering errors according to the procedure outlined by Davies-Colley *et al.* [44]. Unlike what was expected, the specific absorption coefficient reported was not a linear function of chl$a$ concentration for most wavelengths considered. The authors cited incomplete correction of the measurements for scattering errors and large noise as the cause for the non-linearity [43]. We speculate that multiple scattering through such dense suspensions was also in part responsible for these observations.

The present study reports the radiation characteristics of *Nannochloropsis oculata* consisting of the total scattering phase function $\Phi_{T,\lambda}(\Theta)$ at 633 nm, the average absorption and scattering cross-sections $\bar{C}_{abs,\lambda}$ and $\bar{C}_{sca,\lambda}$ between 350 and 750 nm of microalgae grown using white fluorescent light or red LEDs under various illuminances. The corresponding spectral complex index of refraction was also retrieved from the absorption and scattering cross-sections. Finally, the measured spectral absorption coefficient was compared with that predicted by Equation (2.1) using the experimentally measured pigment concentrations.

2.2   Materials and methods

2.2.1   Microalgae cultivation and sample preparation

Microalgae species *Nannochloropsis oculata* UTEX 2164 was purchased from UTEX Austin, TX. Table 2.1 summarizes the experimental and growth conditions used to cultivate the microalgae to measure their radiation characteristics. The microalgae were cultivated in Erdshriber's medium in 2.0 cm thick, 200 ml culture bottles fitted with vented caps exposed to (i) an illuminance of 2,000 lux provided by fluorescent light bulbs (GroLux by Sylvania, USA) or to (ii) an illuminance of 2,000, 5,000, or, 10,000 lux provided by red LEDs

Table 2.1: Summary of experimental conditions used to measure the radiation characteristics of *N. oculata* after 6 days of growth with initial concentration X=0.01 kg/m^3.

Light source	Illuminance (lux)	Medium	Aeration	PBR thickness (cm)	X (kg/m^3)	Mixing
White fluorescent	2,000	Erdshriber	Vented caps	2.0	0.158	Manually twice a day
Red LEDs	2,000	Erdshriber	Vented caps	2.0	0.159	Manually twice a day
Red LEDs	5,000	Erdshriber	Vented caps	2.0	0.084	Manually twice a day
Red LEDs	10,000	Erdshriber	Vented caps	2.0	0.090	Manually twice a day
Red LEDs	2 x 2,500	Artificial seawater	2 v/v% air/CO_2	1.00	1.33	Orbital shaker (95 rpm)
Red LEDs	2 x 5,000	Artificial seawater	2 v/v% air/CO_2	1.00	1.23	Orbital shaker (95 rpm)

(C503B-RAN Cree, USA) with peak wavelength at 630 nm and spectral bandwidth of 30 nm. The conversion between photon flux density and illuminance for the red LEDs and the while fluorescent light source were 47.5 and 33 lux per μmol/m^{2}s, respectively. Mixing of the suspension was performed manually twice a day. The Erdshriber medium had the following composition (per liter of pasteurized seawater): $NaNO_3$ 0.2 g, Na_2HPO_4 0.02 g, $Na_2EDTA \cdot 2H_2O$ 7.5 mg, $CoCl_2 \cdot 6H_2O$ 0.02 mg, $FeCl_3 \cdot 6H_2O$ 0.97 mg, $ZnCl_2$ 0.05 mg, $MnCl_2 \cdot 4H_2O$ 0.41 mg, $Na_2Mo_4 \cdot 2H_2O$ 0.04 mg, Vitamin B12 0.135 mg, and 50 ml soil water: GR+ medium.

Some microalgae were also grown in 1 cm pathlength PBRs exposed from both sides to red LEDs with illuminance of 2 x 2,500 or 2 x 5,000 lux. The artificial seawater medium (ASWM) used had the following composition (per liter of deionized water): NaCl 18 g, $MgSO_4 \cdot 7H_2O$ 2.6 g, KCl 0.6 g, $NaNO_3$ 1 g, $CaCl_2 \cdot 2H_2O$ 0.3 g, KH_2PO_4 0.05 g, NH_4Cl 0.027 g, $Na_2EDTA \cdot 2H_2O$ 0.03 g, H_3BO_3 0.0114 g, $FeCl_3 \cdot 6H_2O$ 2.11 mg, $MnSO_4 \cdot H_2O$ 1.64 mg,

ZnSO$_4$·7H$_2$O 0.22 mg, CoCl$_2$·6H$_2$O 0.048 mg, Vitamin B12 0.135 mg. These cultures were continuously injected with 2 vol.% air/CO$_2$ at 7 ml/min at STP and were placed on an orbital shaker rotating at 95 rpm. Figure 2.1 shows the normalized emission spectrum of both light sources. It also shows the mass absorption cross-sections $Ea_{\lambda,i}$ of photosynthetic pigment chl$a$ as well as carotenoids [42].

Samples used to perform the measurements were taken during the exponential growth phase. Additionally, to avoid absorption and scattering by the growth medium, the microalgae were centrifuged at 10,000 rpm for 2 minutes and washed twice with phosphate buffer saline (PBS) solution and suspended in PBS. The cell size distribution was measured using 2D microscope images captured using a Leica LMIL microscope (Leica Microsystems, Illinois, USA) connected to a CCD camera (Spot Insight Model 4.2, Michigan, USA). The image analysis software imageJ was used to measure the major and minor diameters of cells approximated as axisymmetric spheroids. The data was used to determine the equivalent diameter d_s and the size and frequency distributions $p(d_s)$ and $f(d_s)$.

Microorganism mass concentrations X and cell density N_T were determined using calibration curves relating them to the optical density (OD) of the microalgae suspension at 750 nm. The normal-normal transmittance T_λ and the $OD_\lambda = -lnT_\lambda$ were measured for several concentrations of microalgae at 750 nm in disposable polystyrene cuvettes with pathlength 1 cm using a Fourier transform infrared spectrometer (FTIR) (ThermoNicolet Magna-IR 560). The mass concentration X for five different microalgae dilutions was obtained by filtering the cells through a washed and dried 0.45 nm pore size cellulose membrane filters (HAWP-04700 by Millipore, USA) followed by drying at 60°C in a vacuum oven overnight. The dried filters with the dry cells were weighted immediately after being removed from the oven using a precision balance (model AT261 by Delta Range Factory, USA) with a 0.01 mg precision. The cell density N_T in each dilution was counted using a 20 μm deep Petroff-Hausser counting chamber (Hausser scientific Model 3400, Pennsylvania, USA). The resulting calibration curves were $X = 0.207OD_{750}$ and $N_T = 1.72 \times 10^{14}OD_{750}$ with correlation coefficient R^2 of 0.99 for both calibrations. Here, X and N_T are expressed in dry kg/m^3 and number of

cells/m^3 of suspension, respectively.
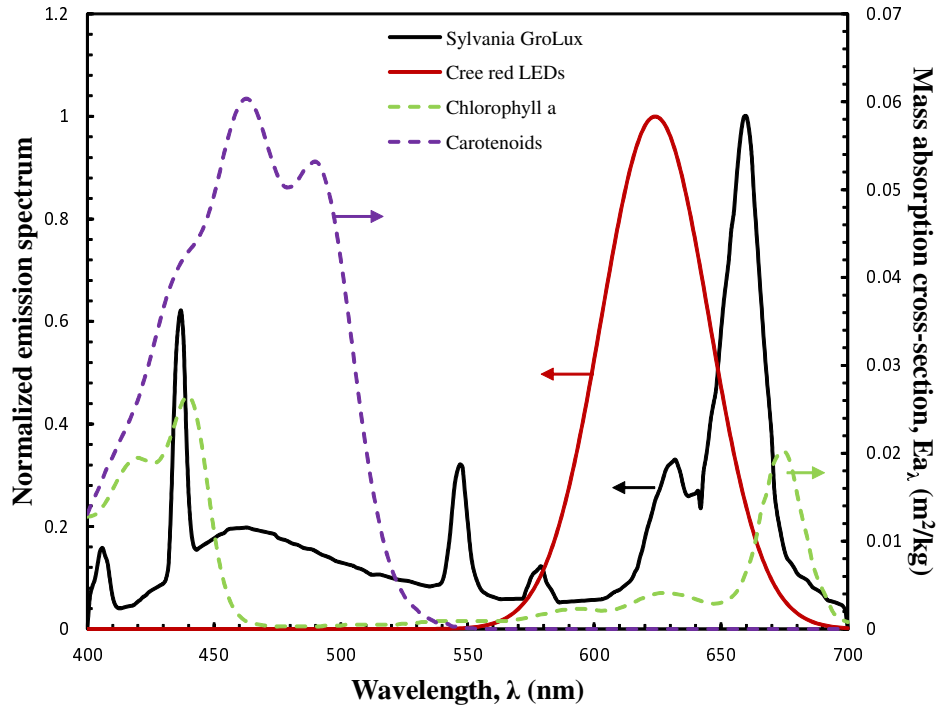
Figure 2.1: Normalized emission spectrum of Sylvania GroLux white fluorescent light source and Cree red LEDs used for *N. oculata* cultivation and *in vivo* absorption cross-sections (in m^2/mg) of chlorophyll *a*, carotenoids [42].

2.2.2   Experiments

2.2.2.1   Assumptions

The following assumptions were made when estimating the average absorption and scattering cross-sections as well as the effective optical properties of the microalgae: (1) The microorganisms were well mixed and randomly oriented. (2) The microalgae were assumed to be homogeneous with an effective complex index of refraction. (3) They were also assumed to be axisymmetric spheroids and treated as spheres. (4) Single scattering prevailed since we considered low concentration suspensions. (5) The total scattering phase function of the

18

suspension had azimuthal symmetry and was only a function of the polar angle Θ. (6) As a first order approximation, the scattering phase function was assumed to be constant over the PAR region.

2.2.2.2   Scattering phase function

The total scattering phase function was measured at 633 nm by a polar nephelometer. The experimental setup and data analysis have previously been reported by Berberoğlu *et al.* [8,45] and need not be repeated. Due to probe interference with the incident laser beam, it was only possible to collect measurements for scattering angles Θ up to 170°. Thus, in order to accurately determine b_λ, it was computed based on the following expression [37]

$$b_\lambda = 1 - \frac{1}{2} \int\limits_0^{\pi/2} \Phi_{T,\lambda}(\Theta) \sin\Theta d\Theta \qquad (2.2)$$

The apparatus and data analysis were validated by successfully comparing the measured scattering phase function of monodispersed latex spheres of 5 μm diameter and predictions from Lorenz-Mie theory using the complex index of refraction of latex at 633 nm as $m_{633} = 1.5823 + i4.5 \times 10^{-4}$ [46].

2.2.2.3   Absorption and scattering cross-sections

The extinction coefficient β_λ was estimated from normal-normal transmittance measurements between 350 and 750 nm using UV-VIS-NIR spectrophotometer (Shimadzu, USA, Model UV-3101PC). The microalgae suspensions were diluted to ensure single scattering. The absorption coefficient κ_λ was determined from normal-hemispherical measurements performed between 350 and 750 nm using an integrating sphere (Shimadzu ISR-3100) attached to the UV-VIS-NIR spectrophotometer [45]. The results for both measurements were corrected for scattering errors and the setup and data analysis was validated according to the analysis presented by Berberoğlu *et al.* [45]. Measurements were performed for three different concentrations to assess their repeatability and the validity of Equations (1.4) to (1.6) as well
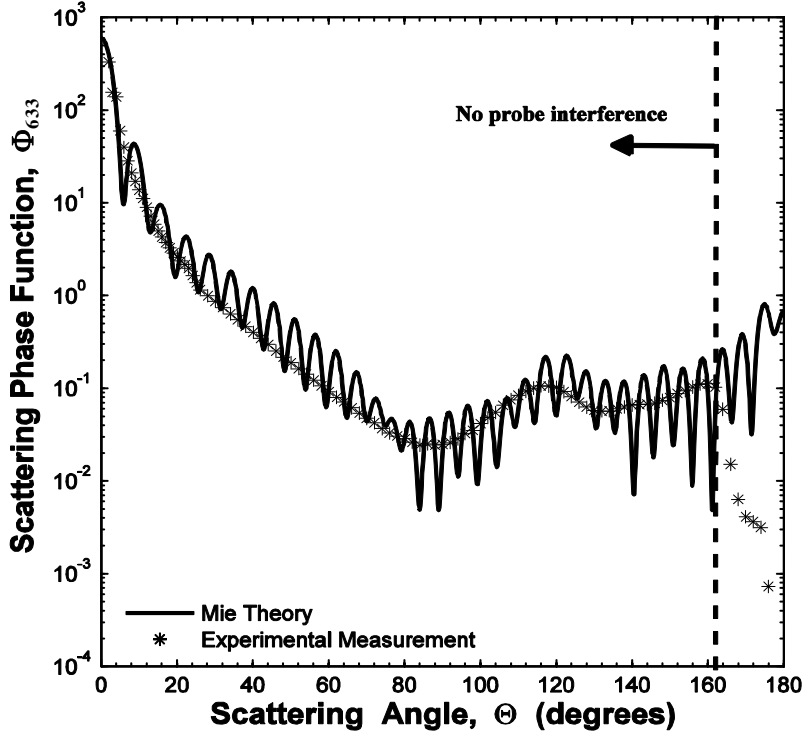
Figure 2.2:   Experimentally measured scattering phase function $\Phi_{633}(\Theta)$ of monodispersed latex spheres of 5 μm diameter and predictions from Lorenz-Mie theory using the complex index of refraction of latex at 633 nm.

as to estimate the average cross-sections $\bar{C}_{abs,\lambda}$ and $\bar{C}_{sca,\lambda}$ and the associated experimental uncertainty.

2.2.3   Retrieving the microalgae effective complex index of refraction

An inverse method combined with Lorenz-Mie theory [35] was used to retrieve the complex index of refraction from (i) the measured average absorption and scattering cross-sections $\bar{C}_{abs,\lambda}$ and $\bar{C}_{sca,\lambda}$, (ii) the cell equivalent diameter distribution $N(d_s)$, and (iii) the spectral refraction index of PBS reported in Ref. [47]. General purpose genetic algorithm code PIKIA [48] was used with a maximum of 30 generations each with a population of 120 individuals to retrieve the refraction and absorption indices for 41 wavelengths between 350 and 750 nm

in 10 nm increments. This method was recently developed and described in detail by Lee *et al.* [38].

2.2.4 Pigment concentration

Chlorophyll *a* and total carotenoid contents were determined spectrophotometrically using 24 hour extraction in methanol as it is most efficient at extracting pigments from microalgae [49]. Note that this method estimates the total carotenoid concentration in the cells and not that of a specific carotenoid. A 2 ml sample of microalgae culture was centrifuged for 2 minutes at 10,000 rpm (6,500 g) and the medium discarded. Then, 3 ml of pure methanol was added to the cell pellets and vortexed for 1 minute. The samples were left in a dark room for 24 hours at approximately 22^oC to ensure maximum pigment extraction. The samples were then centrifuged and the supernatant collected and transferred to 1 cm pathlength polystyrene cuvettes for OD measurements at 480, 666, and 750 nm. The pigment extractions were performed in duplicates and the measurements were repeated three times and averaged. The cell pellets were checked for complete extraction by performing double extractions.

The chlorophyll *a* concentration (in μg/m^3 of suspension) was calculated using the correlation [49]

$$c_{chla} = 15.65(OD_{666} - OD_{750})v/Vl \tag{2.3}$$

where V is the microalgae sample volume (in m^3), v is the volume of solvent (in m^3), and l is the cuvette pathlength (in cm). Similarly, the total carotenoid concentration (in μg/m^3) was calculated according to [50]

$$c_{x+c} = 4(OD_{480} - OD_{750})v/Vl \tag{2.4}$$

Pigment mass fraction (in kg of pigment/kg of dry cell) was estimated as the ratio of pigment concentration to dry mass concentration X, i.e., $w_{chla} = c_{chla}/X$ and $w_{x+c} = c_{x+c}/X$ [51].

2.3 Results and discussion

2.3.1 Mass concentration

All measurements were performed after 6 days of growth in batch mode with an initial mass concentration of 0.01 kg/m^3. The mass concentrations of microalgae at the time the optical measurements were performed are reported in Table 2.1. The microalgae in PBRs injected with 2 vol.% CO_2 showed the largest increase in mass concentration, after 6 days, reaching X=1.33 kg/m^3 for microalgae in PBRs exposed to 2,500 lux red LEDs from both sides. On the other hand, the microalgae grown in vented caps, i.e., without CO_2 injection, exposed to light from a single side showed an order of magnitude lower mass concentration. For example, X reached 0.158 kg/m^3 for microalgae grown under 2,000 lux of red LEDs or white fluorescent light, after 6 days. It fell to 0.084 and 0.090 kg/m^3 when grown under 5,000 and 10,000 lux, respectively.

2.3.2 Size distribution

Figure 2.3 shows a histogram of the equivalent diameter frequency distribution $f(d_s)$ of the microalgae calculated using Equation (1.7) with bins 0.1 μm in width. This distribution was estimated from at least 300 cells for each microalgae suspension grown with six different incident spectra or illuminances. The equivalent cell diameter and the cell aspect ratio did not vary appreciably for the different illumination conditions considered. In all cases, the average equivalent diameter was between 2.51 and 2.63 μm and the standard deviation was 0.35-0.45 μm.

2.3.3 Scattering phase function

Figure 2.4 shows the measured total scattering phase functions at 633 nm of *N. oculata* suspension grown under 2,000 lux white and red light sources. As expected, given the large equivalent cell diameter compared with the wavelength, scattering was mainly in the forward
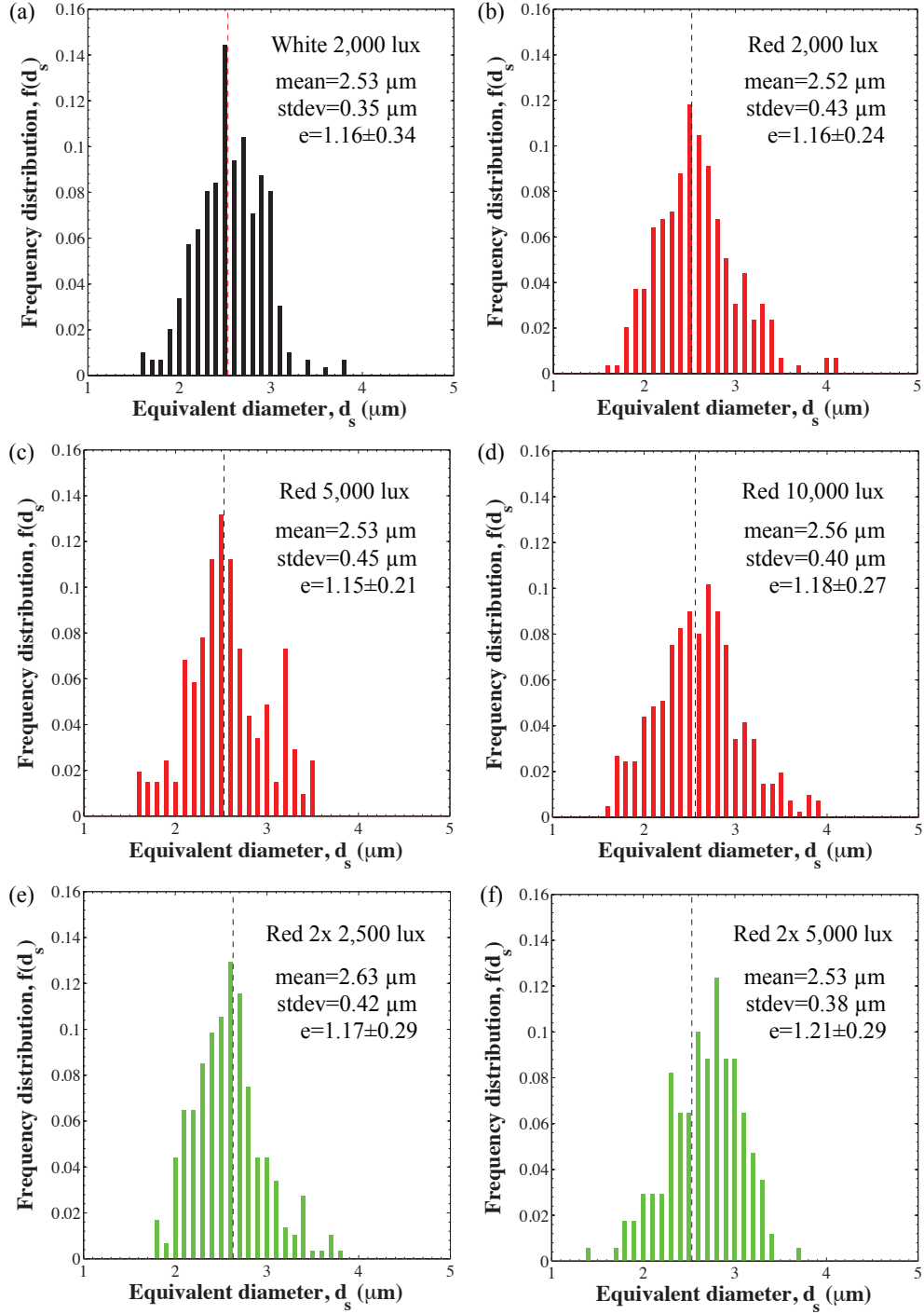
Figure 2.3: Histogram of frequency distribution $f(d_s)$ of the equivalent diameter d_s of *N. oculata* grown under (a) white light at 2,000 lux and red LEDs at (b) 2,000 lux, (c) 5,000 lux, (d) 10,000 lux, (e) 2,500 lux from two side, and (f) 5,000 lux from two sides. The equivalent diameter was calculated from the measured major and minor diameters using Equation (1.7). At least 300 cells were measured for each batch.
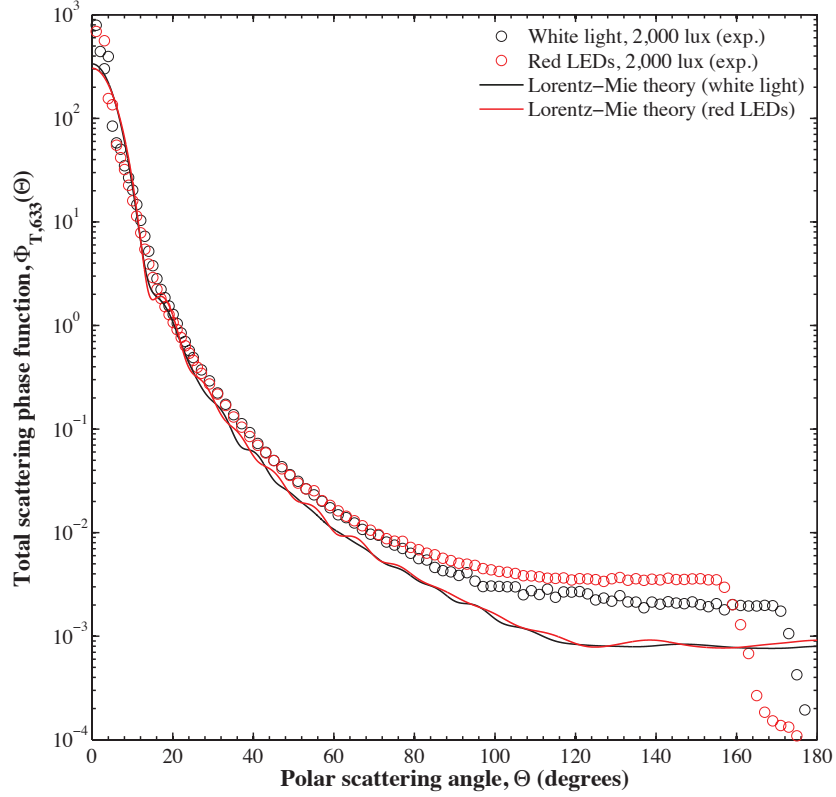
Figure 2.4:   Total scattering phase function $\Phi_{T,633}(\Theta)$ of *N. oculata* at 633 nm measured experimentally using a polar nephelometer for microalgae grown under 2,000 lux white light and red LEDs. The experimental phase functions were compared with predictions by Equation (1.6) using (i) Lorenz-Mie theory, (ii) the measured equivalent diameter distribution $p(d_s)$, and (iii) the retrieved complex index of refraction at 633 nm $m_{633} = 1.3675 + i9.997 \times 10^{-4}$.

direction with Henyey-Greenstein asymmetry factor found to be $g_{633} = 0.986$ at 633 nm for microalgae grown under either light sources. Furthermore, the backward scattering ratio was very small and equal to $b_{633} = 0.0013$ and $b_{633} = 0.0019$ for microalgae grown using white light and red LEDs, respectively.

2.3.4 Absorption and scattering cross-sections

Figures 2.5a and 2.5b show the measured absorption and scattering cross-sections, in the spectral region from 350 to 750 nm, for *N. oculata* grown under (i) white light with an illuminance of 2,000 lux, (ii) red LEDs with an illuminance of 2,000, 5,000, and 10,000 lux and (iii) red LEDs with 2,500 and 5,000 lux on both sides of the 1 cm thick PBR. The results for $\bar{C}_{abs,\lambda}$ and $\bar{C}_{sca,\lambda}$ shown in Figure 2.5 represent the arithmetic mean of the cross-sections measured three times for each of the three different concentrations considered. The error bars correspond to 95% confidence interval. The relatively small error bars established that the absorption and scattering cross-sections were independent of microorganism cell density as assumed in Equations (1.4) and (1.5). It also confirms that multiple scattering was negligible for the cell densities considered. Furthermore, it is evident that scattering dominated over absorption for all wavelengths in the PAR region, i.e., $\bar{C}_{sca,\lambda} > \bar{C}_{abs,\lambda}$. The absorption peaks for *in vivo* chl*a* were apparent at 436 nm, 630 nm, and 676 nm [10] while that of carotenoids was observed at 480 nm [10]. Note that the chl*a* peak at 630 nm is usually concealed by absorption peak of chl*b* in green microalgae [45, 52] which is lacking in *N. oculata*.

The absorption and scattering cross-sections for *N. oculata* grown under 2,000 lux of white and red light sources fell within their experimental uncertainty ranges for all wavelengths considered. This indicates that no chromatic adaptation occurred in the cells despite the different emission spectra of the fluorescent white light and the red LEDs (Figure 2.1). In addition, the absorption and scattering cross-sections of *N. oculata* grown under red LEDs providing illuminance of 2,000, 5,000, and 10,000 lux featured slight variations that fell within their experimental error bars for most wavelengths considered. The slight differences could be attributed to small variation in pigment concentrations, in particular around 480 nm corresponding to absorption peaks of photoprotective carotenoids [42].

By contrast, *N. oculata* grown in PBR exposed to red light from both sides and injected with 2 vol.% CO_2/air mixture featured smaller absorption cross-sections than those grown in the thicker bioreactors exposed to light from only one side. This may be explained
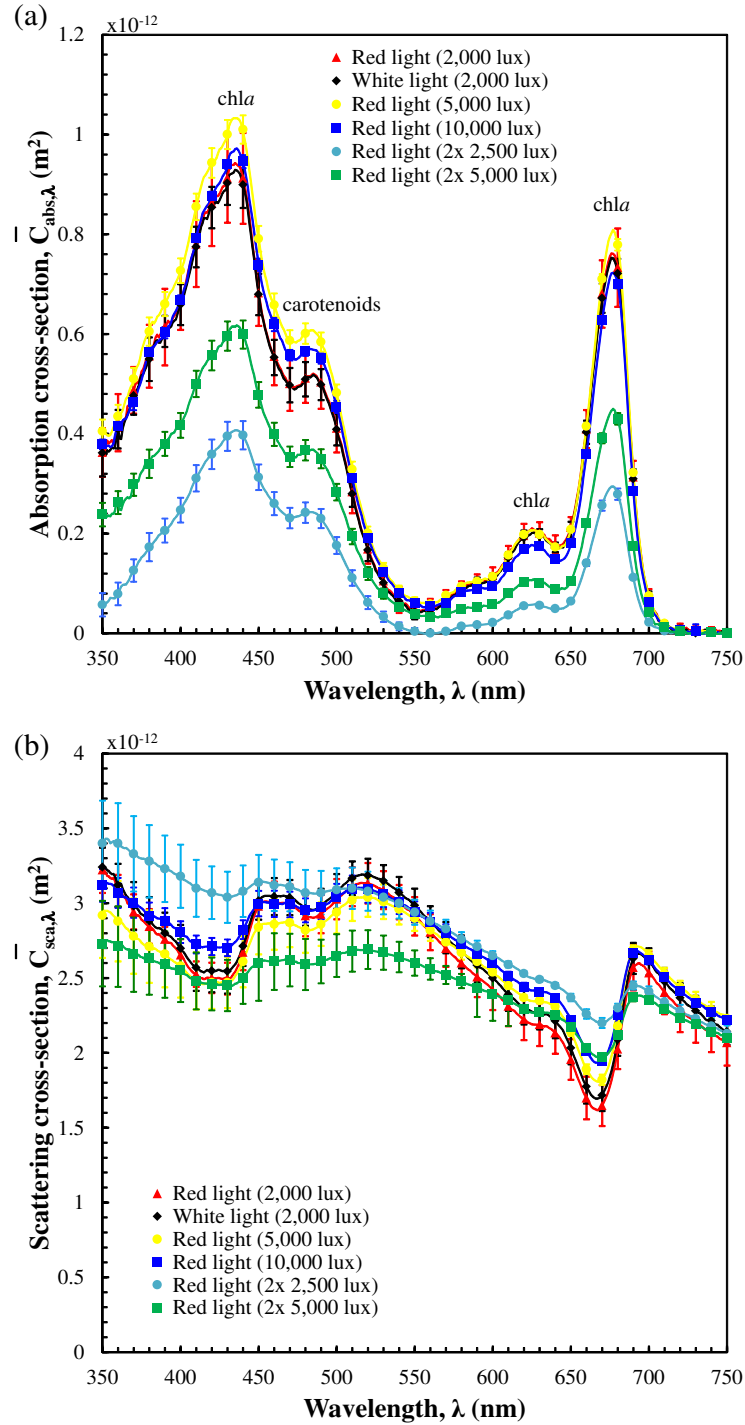
Figure 2.5: Average spectral (a) absorption $\bar{C}_{abs,\lambda}$ and (b) scattering $\bar{C}_{sca,\lambda}$ cross-sections of *N. oculata* grown with fluorescent white light having illuminance of 2,000 lux and red LEDs with illuminance ranging from 2,000 to 10,000 lux. Absorption peaks of chl*a* were observed at 436, 630, and 676 nm and that of carotenoids at 480 nm.

by the fact that the microalgae had reached significantly larger concentration and may have depleted a significant amount of nutrients initially available in the medium. In fact, nitrate limited conditions can stunt biomass production in *Nannochloropsis sp.* and cause a decrease in cell pigment concentrations leading to reduced absorption cross-section $\bar{C}_{abs,\lambda}$ [33]. Furthermore, the microalgae exposed to an illuminance of 5,000 lux from each side featured larger absorption cross-sections than those exposed to 2,500 lux from each side. This could be attributed to the fact that microalgae grown with the 2 x 2,500 lux were harvested at a later stage of their growth and their mass concentration X had reached $1.33\,\mathrm{kg/m^3}$ compared with $1.23\,\mathrm{kg/m^3}$ for *N. oculata* grown under 2 x 5,000 lux. In fact, nutrient availability in the medium can be estimated by stoichiometric calculation. The exact elemental composition of *Nannochloropsis oculata* was not available in the literature. However, microalgae elemental composition does not vary appreciably between different species and has been reported to be composed of 8-12% nitrogen (N) and 0.8-1.5% phosphorus (P) by weight [17, 39, 53]. Assuming a 10% N and 1% P composition by weight for *N. oculata* cells suggests that the culture experienced a phosphate limitation at a biomass concentration of 1.14 g/L and a nitrogen limitation around 1.52 g/L. In addition, the average scattering cross-section $\bar{C}_{sca,\lambda}$ of the microalgae grown with 2 x 2,500 lux was larger than that of microalgae grown with 2 x 5,000 lux. This may be due to their larger mean equivalent diameter of 2.63 μm instead of 2.53 μm [35]. Indeed, Lorenz-Mie theory estimates that the scattering cross-section $C_{sca,550}$ of cells (m_{550}=1.37+i2× 10^{-4}) with diameter 2.53 and 2.63 μm suspended in PBS were 3.17× 10^{-12} m² and 3.68 × 10^{-12} m², respectively. In other words, the scattering cross-section increased by 14% as the cell radius increased by 4%.

Finally, the average scattering cross-section $\bar{C}_{sca,\lambda}$ of *N. oculata* was two orders of magnitude smaller than those of significantly larger green microalgae such as *B. braunii* (d_s=9-15 μm) and *C. littorale* (d_s=6-12 μm) [52]. This is consistent with light scattering theory suggesting that the scattering cross-section increases with the size parameter $\chi = \pi d_s/\lambda$ [35].

2.3.5   Real and imaginary parts of the complex index of refraction

Figures 3.8a and 3.8b show the retrieved refraction and absorption indices of *N. oculata* grown under (i) white light with illuminance of 2,000 lux, (ii) red LEDs with illuminance of 2,000, 5,000, and 10,000 lux, and (iii) red LEDs with 2,500 and 5,000 lux on both sides of the 1 cm thick PBR. The effective refractive index was nearly identical for microalgae grown with white and red light under any illuminance delivered on one or both sides of the PBR. In fact, the relative difference in the effective refraction index n_λ was less than 0.1% for all growth conditions and wavelengths considered. These observations confirm that differences in scattering cross-section $\bar{C}_{sca,\lambda}$, previously discussed, were likely due to differences in size. In addition, the refraction index n_λ ranged from 1.365 to 1.376 and was comparable to the effective refraction indices reported for other microalgae [35, 38]. Here also, n_λ featured dips at wavelengths corresponding to peaks observed in the effective absorption index k_λ. These dips can be attributed to oscillator resonance around the peak absorption wavelengths as predicted by the Helmholtz-Kettler theory describing the relationship between n_λ and k_λ [35]. Note that the amplitude of the resonance in n_λ decreased as the absorption peaks in k_λ weakened.

Figure 3.8b indicates that the effective absorption index k_λ ranged from 0 to 4.32×10^{-3} with peaks at 436, 480, 630, and 676 nm. It was the same for *N. oculata* grown under white light and red LEDs with illuminance of 2,000 lux and under red LEDs with 5,000 and 10,000 lux. In addition, the absorption index of microalgae grown in the 1 cm thick PBRs with 2 x 2,500 lux red LEDs was on average 76% lower than that of microalgae grown with 5,000 lux red LEDs exposed from one side. Similarly, microalgae grown in the 1 cm thick PBR with 2 x 5,000 lux red light had absorption index 36% smaller than those grown under red light at 10,000 lux. As previously suggested, the lower absorption index could be attributed to the lower pigment content of the cells caused by nutrient deficient conditions.
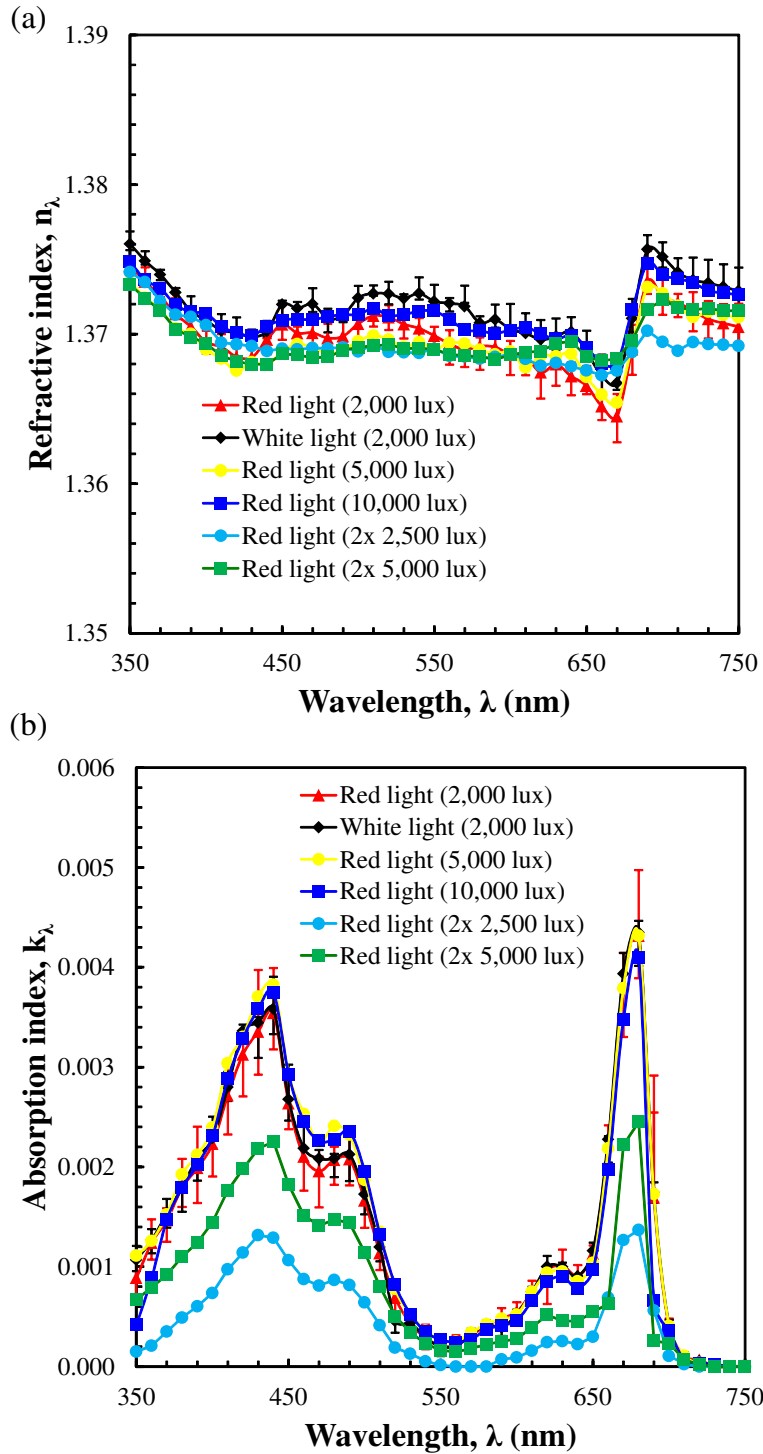
Figure 2.6: Spectral (a) refraction n_λ and (b) absorption k_λ indices of *N. oculata* retrieved using Lorenz-Mie theory for microalgae grown under fluorescent white light with illuminance of 2,000 lux and red LEDs with illuminance ranging from 2,000 to 10,000 lux.

2.3.6 Lorenz-Mie scattering phase function

Figure 2.4 displays the total scattering phase function $\Phi_{T,633}(\Theta)$ of *N. oculata* grown under 2,000 lux predicted by Equation (1.6) where $\Phi_\lambda(d_s, \Theta)$ was predicted by Lorenz-Mie theory using (i) the retrieved complex index of refraction at 633 nm $m_{633} = 1.3675 + i9.997 \times 10^{-4}$, (ii) the refraction index of PBS taken as $n_{PBS,633} = 1.334$ [47], and (iii) the measured equivalent diameter distribution $p(d_s)$. The backward scattering ratio b_{633} was estimated from Lorenz-Mie theory to be 0.0006 for microalgae grown using either light source. This value should be compared with experimental measurements of b_{633} of 0.0013 and 0.0019 for white and red incident light at 2,000 lux, respectively. More importantly, the Henyey-Greenstein asymmetry factor g_{633} estimated from Lorenz-Mie theory for microalgae grown under both light sources was 0.988 compared with 0.986 measured experimentally.

Furthermore, the asymmetry factor g_λ was estimated from Lorenz-Mie theory over the spectral range from 350 to 750 nm using the equivalent diameter distribution $p(d_s)$ and the retrieved spectral refraction and absorption indices retrieved from *N. oculata* grown under 2,000 lux (Figures 3.8a and 3.8b). It was found to be nearly independent of wavelength over the PAR region as it only varied between 0.9878 and 0.9884. This confirms Assumption 6 made when correcting normal-normal and normal-hemispherical transmittances for forward scattering.

2.3.7 Pigment concentrations

Table 2.2 summarizes the chlorophyll *a* and total carotenoid mass fractions in wt.% extracted from *N. oculata* grown under different light sources and illuminances.

The extracted chl*a* mass fraction was w_{chla}=2.25 ±0.04 wt.% and 2.21 ± 0.16 wt.% for *N. oculata* grown using 2,000 lux white light and red LEDs, respectively. Their respective total carotenoid mass fraction w_{x+c} was 0.73 ± 0.01 wt.% and 0.72 ± 0.07 wt.%. Overall, there was no statistically significant difference in pigment concentrations between the batches grown under 2,000 lux using white light or red LEDs indicating that no chromatic adaptation

Table 2.2: Chlorophyll *a* and total carotenoid mass fractions (%) and chlorophyll *a* to carotenoid ratio extracted from *N. oculata* grown under various light sources and illuminances summarized in Table 2.1.

Light source	Illuminance	Chlorophyll *a*	Total carotenoid	w_{x+c}/w_{chla}
	(lux)	(wt.%)	(wt.%)	
White	2,000	2.25 ±0.04	0.73 ±0.01	0.32
Red	2,000	2.21 ±0.16	0.72 ±0.07	0.32
Red	5,000	2.46 ±0.12	0.56 ±0.06	0.23
Red	10,000	2.08 ±0.01	0.43 ±0.01	0.21
Red	2x 2,500	0.28 ±0.002	0.45 ±0.01	1.61
Red	2x 5,000	0.549 ±0.03	0.23 ±0.06	0.43

occurred. These pigment concentrations and dry mass fractions were also consistent with those previously reported in the literature for *N. oculata* [43, 54].

The chlorophyll *a* and total carotenoid mass fractions of microalgae grown under red LEDs with different incident illuminances showed trends similar to those observed in their absorption cross-sections (Figure 2.5a). There were no statistically significant changes in the measured pigment concentrations. Larger carotenoid mass fraction has been reported in *Nannochloropsis sp.* grown under larger irradiances [33]. However, Lubián *et al.* [31] showed this effect to be significant in *N.salina* while the increase in zeaxanthin, astaxanthin, and antheraxantin in *N.oculata* were less pronounced and coincided by reduction in vioxanthin, thus maintaining an approximately constant total carotenoid mass fraction.

Moreover, Table 2.2 indicates that microalgae grown in the thinner 1 cm thick PBRs exposed to red LEDs on both sides had pigment mass fractions one order of magnitude lower than those grown in the thicker PBR exposed to light from only one side. Furthermore, *N. oculata* grown exposed to 2 x 2,500 lux contained lower chl*a* and carotenoids mass fractions than those exposed to 2 x 5,000 lux. This can be attributed to more severe nutrient deficient conditions in the PBRs exposed to 2 x 2,500 lux where microalgae concentration was the
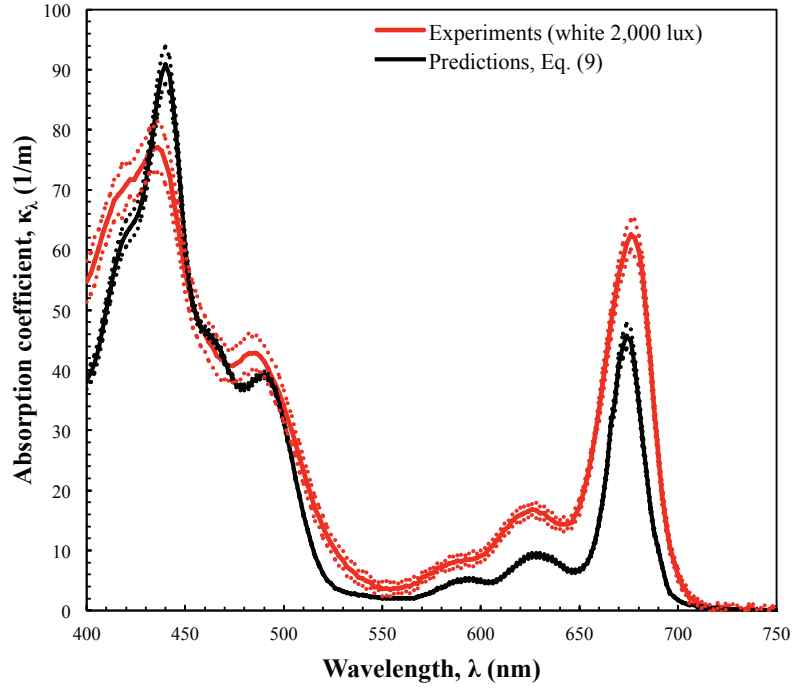
Figure 2.7: Comparison of the experimentally measured absorption coefficient of *N. oculata* grown with 2,000 lux white fluorescent light with mass concentration X=0.10 kg/m^3 and that predicted by Equation (2.1) using the measured pigment concentrations c_{chla}=2.25 $\times 10^{-3}$ kg/m^3, c_{x+c}= 1.30 $\times 10^{-3}$ kg/m^3. The dotted lines correspond to the 95% confidence intervals.

largest. The ratio of carotenoid to chlorophyll content is often cited as the measure of stress the culture is experiencing. Van Vooren *et al.* [39] showed that the ratio of carotenoid to chlorophyll *a* in *N. oculata* increased during nitrogen starvation and exceed unity. Similarly, in the PBRs injected with CO_2 this ratio was larger compared with microalgae grown in the thicker reactors. In fact, it reached 1.61 for the microalgae grown in PBR exposed to 2 x 2,500 lux further supporting the assertion of nutrient starvation in this culture.

2.3.8 Model validation

Figure 2.7 shows the absorption coefficient κ_λ of a microalgae culture with a mass concentration $X = 0.10$ kg/m^3 measured experimentally for *N. oculata* grown under 2,000 lux using white light and that predicted by Equation (2.1) using the experimentally measured pigment concentrations c_{chla} and c_{x+c}. The average relative error between experimental measurements and predictions of κ_λ by Equation (2.1) was 36% over the PAR region. The relative error was 10.8% and 28% at 436 nm and 676 nm corresponding to chl$a$ absorption peaks. At these wavelengths, the predicted mass absorption cross-section featured sharper absorption peaks than those experimentally measured. This was also observed for other microalgae species [38]. The flattening of the absorption peaks observed experimentally may be due to the so-called "package effect" [35]. In other words, pigments display a different absorption cross-section once they are packaged inside a cell. This is due to the non-linear dependence of absorption on (i) pigment concentrations, (ii) cell refractive index, (iii) cell size, and (iv) pigment location within the cell [35]. This suggests that simple superposition of the individual pigment's absorption cross-sections, as suggested by Equation (2.1), may not be adequate to accurately predict the mass absorption cross-section of microalgae.

2.4   Chapter summary

This chapter presented measurements of absorption and scattering cross-sections and optical properties of *N. oculata* using white light and red LEDs with illuminance ranging from 2,000 to 10,000 lux. The microalgae average equivalent diameter ranged from 2.52 to 2.63 μm. Their cross-sections and optical constants were statically identical over most of the PAR region. *N.oculata* grown in 2 vol.% CO_2 injected PBRs featured lower pigment concentration and significantly smaller absorption cross-section and absorption index due to nutrient limited growth conditions. By contrast, the refraction index was identical for all conditions considered, falling between 1.365 and 1.376.

CHAPTER 3

Equivalent Radiation Characteristics of Microalgae Colonies and Aggregates

Microalgae cells can form colonies or aggregates under stress due to the production of exopolysaccharides potentially affecting their radiation characteristics. Experimental characterization of colonies in terms of their number of cells and individual cell size can be very challenging. Thus, this chapter presents numerical predictions of radiation characteristics of microalgae colonies. The exact numerical solution for predicting these radiation characteristics is time consuming and requires large computational resources. This chapter presents a new simplified model for predicting the radiation characteristics of randomly oriented microalgae colonies.

3.1   Introduction

Particle aggregation and coagulation is a frequent occurrence in numerous applications such as combustion systems [55], atmospheric science [56, 57], astronomy and astrophysics [58], chemistry [59], and biotechnology [60–62]. Small particles aggregate to form fractal-like structures changing the light absorption and scattering properties of the suspension [56]. For example, Figures 3.1a to 3.1f show micrographs of soot [63], snow [64], cosmic dust [65], gold nanoparticles [66], bacteria [67], and microalgae aggregates, respectively. In all these systems, knowledge of the radiation characteristics of the fractal aggregates are of prime importance for radiation transfer analysis and remote sensing applications. The radiation characteristics of soot and aerosol aggregates have been studied extensively as reviewed by Sorensen [56]. However, to the best of our knowledge, those pertaining to aggregates

composed of larger monomers such as microalgae colonies have not been studied.
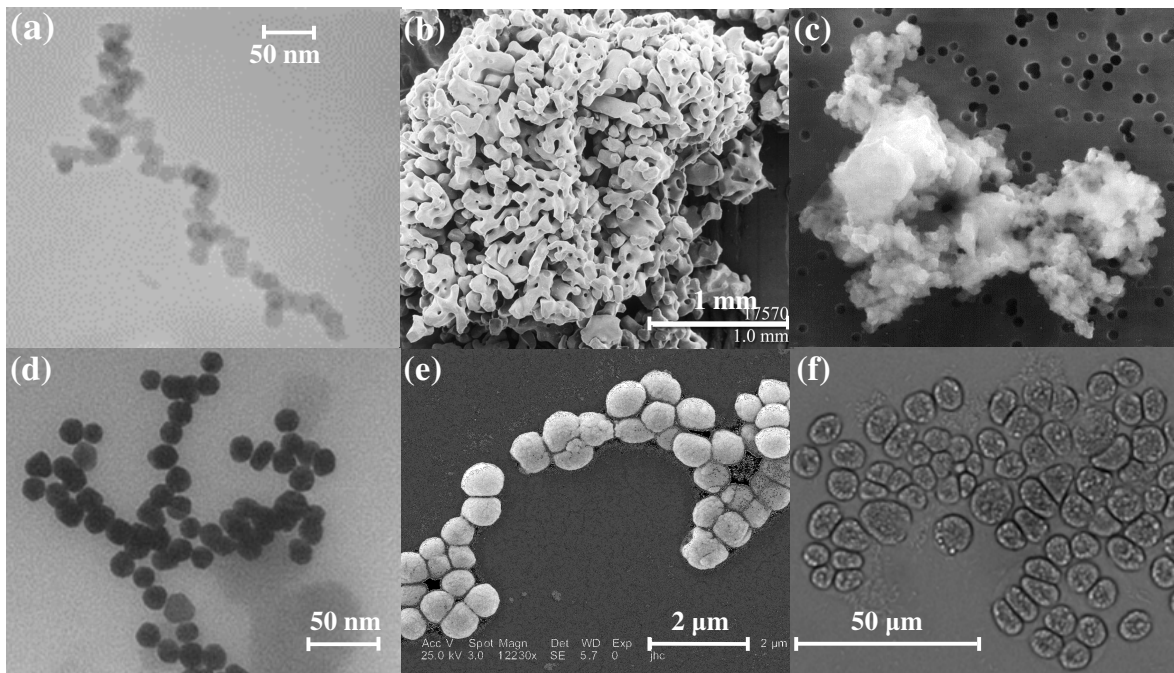
Figure 3.1: Micrographs of fractal aggregates of (a) soot [63], (b) snow [64], (c) cosmic dust [65], (d) gold nanoparticles [66], (e) the bacteria *M. luteus* [67], and (f) the microalgae *B. braunii*.

Microalgale are single cell photosynthetic microorganisms growing in freshwater or seawater. They can be grown in photobioreactors (PBRs) exposed to solar radiation to produce biofuels as well as various pharmaceuticals and biochemicals [68]. For example, *Botryococcus braunii* (Figure 3.1f) can be used for producing biofuels used for powering jet engines [68]. This species secretes exopolysaccharides (EPS), a viscous substance coating the cell surface and causing their aggregation into colonies. EPS production is part of a protection mechanism activated in response to environmental conditions such as limited illumination [69], non-optimal temperature [70], high salinity [70], and limited nutrient availability [71]. In addition, a recent study demonstrated reversible cell aggregation in concentrated *Chlorella vulgaris* cultures used for protein, starch, and lipid production [72]. The authors hypothesized that aggregation occurred at large cell concentration due to the proximity of the cells to

one another. Since larger microalgae cells possess a larger surface charge density compared to smaller cells, the electrostatic repulsion between larger cells is much stronger than that between a large and a small cell [72]. This leads to aggregation of the smaller cells in the space created by the electrostatic repulsion between the larger cells.

To achieve maximum biomass and biofuel productivities, light transfer in the PBRs must be optimized [8, 73, 74]. For example, a flat-plate PBR should be designed and operated such that the fluence rate at the backwall corresponds to the photosynthetic compensation point, i.e., the minimum amount of energy required to maintain cell metabolism [74]. The latter was reported to be 10 μmol$_{h\nu}$/m^{2}s for the microalgae *Chlamydomonas reinhardtii* [75] and 2 μmol$_{h\nu}$/m^{2}s for the cyanobacteria *Arthrospira platensis* [73]. Optimizing PBRs for maximum biomass productivity requires the solution to the radiative transfer equation and the knowledge of the absorption and scattering cross-sections as well as the scattering phase function of the microalgal suspension [8]. Moreover, the scattering matrix elements of the microalgal suspension may be measured for remote sensing of the PBR [35]. The radiation characteristics of suspensions composed of single cells can be predicted theoretically [41, 76–78] or measured experimentally [8, 79]. However, theoretical or experimental characterization of the radiation characteristics of suspensions consisting of microalgae colonies have received less attention.

Several numerical methods exist to estimate the radiation characteristics of aggregates consisting of spherical monomers. They include the superposition T-matrix method [80], the generalized multiparticle-Mie theory [81], and the volume integral method [82]. However, depending on the size of the aggregate, calculations can be time consuming and require large computational resources [58]. Thus, it would be computationally far more efficient to approximate the radiation characteristics of aggregates with complex morphology by those of particles with simple shapes such as spheres, coated spheres, or cylinders whose radiation characteristics can be computed relatively rapidly [83]. For example, Drolen and Tien [84] approximated the absorption and scattering cross-sections of soot particle aggregates as those of a volume equivalent solid sphere. More recently, Lee and Pilon [85] demonstrated

that the absorption and scattering cross-sections per unit length of randomly oriented linear chains of spheres can be approximated as those of randomly oriented infinitely long cylinders with equivalent volume per unit length. Alternatively, The Rayleigh-Debye-Gans (RDG) approximation provides an analytical expression for the absorption and scattering cross-sections and the scattering phase function of aggregates based on the assumption that the size of the monomers is much smaller than the incident radiation wavelength [86].

This study aims to identify approximations and equivalent particles for rapidly and accurately predicting the absorption and scattering cross-sections and the scattering matrix elements of fractal aggregates composed of relatively large monodisperse or polydisperse optically soft spherical monomers. The goal is to facilitate the predictions of radiation characteristics of fractal aggregates with large monomers compared with the wavelength of the incident radiation where numerical methods are too time consuming and resource intensive for practical purposes.

3.2 Background

3.2.1 Modeling fractal aggregates

An ensemble of N_s monodisperse spherical monomers of radius a aggregated in a fractal structure satisfies the statistical rule given by [56]

$$N_s = k_f \left(\frac{R_g}{a} \right)^{D_f} \tag{3.1}$$

where R_g is the aggregate radius of gyration defined as the mean of the distances between the aggregate center of mass and the geometric center of each particle. The constants D_f and k_f are the so-called fractal dimension and prefactor, respectively. For example, ordered linear chains of spheres (1D), square sheets (2D), and simple cubic (3D) aggregates have fractal dimensions D_f of 1.0, 2.0, and 3.0, respectively. On the other hand, fractal dimension D_f of random aggregates depends on the aggregation mechanism [56]. Aggregation by collisions due to Brownian motion can result in diffusion limited aggregation or in reaction limited

aggregation [56]. In diffusion limited aggregation, particles collide and immediately stick to the surface of the aggregate [61]. These aggregates typically have fractal dimension D_f of 1.75-1.8 [61]. In reaction limited aggregation, particles may penetrate the aggregate when they collide without immediately sticking to the surface. These aggregates feature fractal dimension D_f equal to 2.2 [61]. Jiang and Logan [61] experimentally determined the fractal dimension of aggregates formed through shear-induced coagulation to be larger than 2.4. In addition, Jackson *et al.* [62] experimentally found that the fractal dimension of phytoplanktonic suspensions ranged from 2.25 to 2.36. The prefactor k_f is typically treated as a fitting constant also known as the packing factor [61]. It has been reported to range between 1.2 and 3.0 for soot particles [86–89]. Sorensen [56] and Lapuerta [90] assumed a value of k_f for aggregates of soot particles to be 1.593 corresponding to the most compact packing of monodisperse monomers.

Fractal aggregate formation can be numerically simulated using particle cluster aggregation algorithm [56,91,92]. This method launches a spherical particle of radius a on a random walk. A collision between the marching particle and the aggregate leads to adherence of the two if the new aggregate structure satisfies the prescribed prefactor k_f and fractal dimension D_f [91]. This procedure is repeated until the aggregate contains the desired number of monomers N_s.

3.2.2 Scattering matrix

The Stokes vector is composed of the four Stokes parameters I, Q, U, and V describing the intensity and degree of polarization of an electromagnetic wave [93]. For a given aggregate whose center of mass is located at the origin of a spherical coordinate system, the far-field scattered intensity at location $\mathbf{r}$ in direction $\hat{s}$ is denoted by $\mathbf{I_{sca}}(\mathbf{r}, \hat{s}) = (I_{sca}, Q_{sca}, U_{sca}, V_{sca})^T$ can be related to the incident irradiance $\mathbf{I_{inc}}(\hat{s}_i) = (I_{inc}, Q_{inc}, U_{inc}, V_{inc})^T$ by the Mueller matrix $[Z(\Theta)]$ according to [80]

$$\mathbf{I_{sca}}(\mathbf{r}, \hat{s}) = \frac{1}{r^2}[Z(\Theta)]\mathbf{I_{inc}}(\hat{s}_i) \tag{3.2}$$

Here, r is the norm of the location vector $\mathbf{r}$ corresponding to the distance between the particle and the observation point. The scattering angle Θ is defined as the angle between the incident $\hat{s}_i$ and the scattered $\hat{s}$ directions. For randomly oriented aggregates, it is more convenient to use the normalized scattering, or Stokes, matrix $[F(\Theta)]$ given by [94]

$$[F(\Theta)] = \frac{4\pi}{\langle C_{sca}^a \rangle} [Z(\Theta)] \tag{3.3}$$

where $\langle C_{sca}^a \rangle$ is the orientation-averaged scattering cross-section of the aggregate. It is defined as the fraction of the unpolarized radiant energy incident on the surface of the randomly oriented aggregate that is scattered in any direction [95]. Similarly, the orientation-averaged absorption cross-section $\langle C_{abs}^a \rangle$ represents the fraction of the unpolarized radiant energy incident on the surface of the aggregate that is absorbed [95]. The orientation-averaged extinction cross-section $\langle C_{ext}^a \rangle$ is defined as the sum of the absorption and scattering cross-sections, i.e., $\langle C_{ext}^a \rangle = \langle C_{abs}^a \rangle + \langle C_{sca}^a \rangle$ [95]. For randomly oriented aggregates with a plane of symmetry, the scattering matrix $[F(\Theta)]$ can be expressed as [95]

$$[F(\Theta)] = \begin{bmatrix} F_{11}(\Theta) & F_{21}(\Theta) & 0 & 0 \\ F_{21}(\Theta) & F_{22}(\Theta) & 0 & 0 \\ 0 & 0 & F_{33}(\Theta) & F_{34}(\Theta) \\ 0 & 0 & -F_{43}(\Theta) & F_{44}(\Theta) \end{bmatrix} \tag{3.4}$$

The scattering matrix element $F_{11}(\Theta)$ is the scattering phase function and represents the angular distribution of unpolarized scattered radiation [95]. It is normalized according to [95]

$$\frac{1}{4\pi} \int_{4\pi} F_{11}(\Theta) d\Omega = 1 \tag{3.5}$$

where Ω is the solid angle around the scattering angle Θ. The asymmetry factor of an aggregate can be defined as [93]

$$g = \frac{1}{4\pi} \int_{4\pi} F_{11}(\Theta) \cos \Theta d\Omega \tag{3.6}$$

It describes the shape of the scattering phase function and is equal to 0, 1, and -1 for isotropic, purely forward, and purely backward scattering, respectively [95]. In addition,

the Henyey-Greenstein (HG) approximate phase function is often used in radiative transfer analysis for its simplicity as it predicts $F_{11}(\Theta)$ only as a function of the asymmetry factor g according to [37]

$$F_{11,HG}(\Theta) = \frac{1 - g^2}{[1 + g^2 - 2g\cos\Theta]^{3/2}} \qquad (3.7)$$

The scattering matrix element ratio $-F_{21}/F_{11}$ corresponds to the degree of linear polarization of the scattered radiation for an incident unpolarized light [96]. On the other hand, the scattering matrix element ratio F_{22}/F_{11} is representative of the sphericity of the scattering body and is equal to 1 for spherical particles. The ratio F_{34}/F_{11} relates to the amount of obliquely polarized incident radiation that is scattered into circularly polarized radiation [96]. The scattering matrix element ratios F_{33}/F_{11} and F_{44}/F_{11} behave similarly as a function of scattering angle Θ and are equal for spherical scatterers. Several analytical and numerical methods exist for predicting the absorption and scattering cross-sections of aggregates as well as their scattering matrix elements as discussed in the following sections.

3.2.3 The Rayleigh-Debye-Gans (RDG) approximation

Monomers of radius a in a given aggregate are characterized by (i) their size parameter defined as $\chi_s = 2\pi a\lambda^{-1}$ where λ is the wavelength of radiation in vacuum and (ii) their relative complex index of refraction $m = n + ik$ defined as the ratio of the complex indices of refraction of the monomers $m_s = n_s + ik_s$ and of the refractive index n_m of the non-absorbing surrounding medium [86]. The Rayleigh-Debye-Gans (RDG) approximation provides a closed-form analytical expression for absorption and scattering cross-sections as well as for the scattering phase function of randomly oriented fractal aggregates [56, 86, 97]. It is valid for aggregates composed of optically soft monomers such that $|m - 1| << 1$ with small size parameters, i.e., $\chi_s << 1$. Under these conditions, the aggregate absorption cross-section $\langle C_{abs,RDG}^a \rangle$ is the sum of the absorption cross-sections of all constituent monomers and is expressed as [56, 86]

$$\langle C_{abs,RDG}^a \rangle = N_s \langle C_{abs,R} \rangle \qquad (3.8)$$

Here, $\langle C_{abs,R} \rangle$ is the absorption cross-section of a single spherical monomer of size parameter χ_s given, in the Rayleigh scattering regime, by [86]

$$\langle C_{abs,R} \rangle = \frac{\lambda^2 \chi_s^3}{\pi} \text{Im} \left(\frac{m^2 - 1}{m^2 + 2} \right). \tag{3.9}$$

Similarly, the aggregate scattering cross-section $\langle C_{sca,RDG}^a \rangle$ can be estimated by [56, 86]

$$\langle C_{sca,RDG}^a \rangle = 2\pi N_s^2 \langle C_{sca,vv,R} \rangle \int_0^\pi \frac{1}{2} S(qR_g)(1 + \cos^2 \Theta) \sin \Theta d\Theta \tag{3.10}$$

where $\langle C_{sca,vv,R} \rangle$ represents the vertically polarized scattering cross-section for vertically polarized incident radiation [56, 86]. For a monomer of size parameter χ_s in the Rayleigh scattering regime, $\langle C_{sca,vv,R} \rangle$ can be written as

$$\langle C_{sca,vv,R} \rangle = \frac{\lambda^2 \chi_s^6}{4\pi^2} \left| \frac{m^2 - 1}{m^2 + 2} \right|^2 \tag{3.11}$$

Here, $S(qR_g)$ is the scattering structure factor of the aggregates describing the intensity of scattered radiation as a function of the scattering wavevector $q = 4\pi\lambda^{-1}\sin(\Theta/2)$ [56]. For an aggregate of fractal dimension D_f and radius of gyration R_g, $S(qR_g)$ can be expressed as [97]

$$S(qR_g) = \left[1 + \frac{8}{3} \frac{(qR_g)^2}{D_f} + (qR_g)^8 \right]^{-D_f/8} \tag{3.12}$$

Note that, for very small and very large aggregates compared with the radiation wavelength, i.e., for $qR_g \ll 1$ and $qR_g \gg 1$, the structure factor simplifies to $S(qR_g) = 1$ and $S(qR_g) = (qR_g)^{-D_f}$, respectively [56]. In these two limiting cases, the aggregate scattering cross-section $\langle C_{sca,RDG}^a \rangle$ is proportional to N_s^2 and N_s, respectively. In the first case, the scattered waves are in phase and their amplitudes add constructively [56]. In the second case, the phases are random and the waves add randomly [56].

Finally, the unpolarized scattering phase function $F_{11,RDG}(\Theta)$ of the aggregate predicted by the RDG approximation is expressed as [86]

$$F_{11,RDG}(\Theta) = \frac{1}{2} \frac{\langle C_{sca,vv,RDG}^a \rangle}{\langle C_{sca,RDG}^a \rangle} \left(1 + \cos^2 \Theta \right) \tag{3.13}$$

where the vertically polarized scattering cross-section of the aggregate for vertically polarized incident radiation, denoted by $\langle C^a_{sca,vv,RDG} \rangle$, is defined as [86]

$$\langle C^a_{sca,vv,RDG} \rangle = N_s \langle C_{sca,vv,R} \rangle S(qR_g). \tag{3.14}$$

The asymmetry factor g_{RDG} of the aggregate can also be estimated from the scattering phase function $F_{11,RDG}(\Theta)$ using Equation (3.6).

The validity of the RDG approximation has been investigated in numerous studies. Farias *et al.* [86] compared absorption and scattering cross-sections predicted by the RDG approximation with those estimated by volume integral formulation of Maxwell's equations [82]. The authors examined randomly oriented aggregates of fractal dimensions D_f between 1.0 and 3.0 with monomer size parameter χ_s ranging from 0.01 to 1.0, and $|m - 1|$ between 0.1 and 2.0. The RDG approximation predicted the scattering cross-section of aggregates consisting of 16 to 256 monodisperse monomers within 10% of those predicted by the volume integral method for size parameter $\chi_s < 0.3$. However, the accuracy of predictions of both absorption and scattering cross-sections by the RDG approximation deteriorated with increasing size parameter χ_s [86]. Wang and Sorensen [98] experimentally validated the RDG approximation by comparing the measured scattering cross-sections at 488 nm of aggregates with fractal dimension D_f of 1.75, composed of monodisperse monomers 20 nm in diameter made of SiO_2 (m=1.46) or TiO_2 (m=2.61). Note that at this wavelength, absorption by the aggregates could be ignored. On the other hand, Bushell [99] measured the scattering intensity of aggregates of latex particles 4.9 μm in diameter using a forward light scattering photometer. The author found poor agreement between experimental measurements and predictions by the RDG approximation. He attributed the discrepancy to multiple scattering and recommended using the superposition T-matrix theory [80] for such aggregates. Unfortunately, the author did not report the radiation wavelength and morphology (i.e., k_f and D_f) of the aggregates. However, we speculate that the monomer size parameter χ_s exceeded the range of validity of the RDG approximation.

3.2.4 Numerical predictions of aggregate radiation characteristics

The superposition T-matrix method [80], the generalized multiparticle-Mie theory [81], and the volume integral method [82] provide numerical solutions to Maxwell's equations for aggregates with arbitrary fractal dimension and number of monomers. For example, the superposition T-matrix method estimates the total scattered electromagnetic field at any given location by summing the contribution from each monomer [80].

Liu *et al.* [100] used the generalized multiparticle-Mie theory to predict the absorption and scattering cross-sections of soot aggregates featuring fractal dimension D_f of 1.4, 1.78, or 2.1 and a fractal prefactor k_f of 2.3. The aggregates were composed of up to 800 monodisperse monomers with size parameter χ_s=0.18 and relative complex index of refraction $m = 1.6 + i0.6$. They demonstrated that both aggregate absorption and scattering cross-sections normalized, respectively, by the product of the number of monomers in the aggregate and the absorption or scattering cross-sections of a single monomer, i.e., $\langle C_{abs}^a \rangle / N_s \langle C_{abs} \rangle$ or $\langle C_{sca}^a \rangle / N_s \langle C_{sca} \rangle$, increased as a function of N_s for aggregates of all fractal dimensions and number of monomers considered. The authors attributed both of these observations to multiple scattering. In a similar study, Liu *et al.* [101] demonstrated that the normalized absorption cross-section per monomer $\langle C_{abs}^a \rangle / N_s \langle C_{abs} \rangle$ decreased as a function of N_s for soot aggregates featuring a fractal dimension D_f of 1.78 and a fractal prefactor k_f of 1.3 or 2.3. The aggregates were composed of 20 or more monomers of size parameter χ_s of 0.354 and relative complex index of refraction $m = 1.6 + i0.6$. The decrease in $\langle C_{abs}^a \rangle / N_s \langle C_{abs} \rangle$ was attributed to the fact that outer particles of the aggregates shielded the inner ones from the incident radiation. Moreover, the normalized scattering cross-section per monomer $\langle C_{sca}^a \rangle / N_s \langle C_{sca} \rangle$ increased as a function of N_s due to multiple scattering [101].

Iskander *et al.* [82] developed a method for predicting the absorption and scattering cross-sections and the scattering matrix elements of aggregates by solving the volume integral formulation of Maxwell's equations [95]. This method is also known as the discrete dipole approximation and has been reviewed by Yukin and Hoekstra [102]. Manickavasagam and

Mengüç [96] used this method to predict the scattering matrix elements of randomly oriented soot aggregates with fractal dimension D_f and prefactor k_f equal to 1.7 and 5.8, respectively. The numerically generated aggregates contained up to 150 monodisperse monomers of radius 20, 40, or 60 nm and relative complex index of refraction equal to $1.8 + i0.5$. The authors concluded that the scattering phase function $F_{11}(\Theta)$ could not be used to identify either the number N_s of monomers in an aggregate or the monomer radius a. However, they demonstrated that spectral and angular variations in the scattering matrix element ratio $F_{21}(\Theta)/F_{11}(\Theta)$ could be used to determine both N_s and a. By contrast, the angular peaks in the scattering matrix element ratio $F_{34}(\Theta)/F_{11}(\Theta)$ depended on the monomer radius a but not on the number of monomers N_s [96]. The authors hypothesized that these peaks could be used to identify the monomer radius.

These different methods have been used to predict the radiation characteristics of soot aggregates [55, 57, 91, 96, 100, 103–105], snow [106], comets [58], and cosmic dust aggregates [58]. In these applications, the monomers are relatively small compared with the radiation wavelength such that $\chi_s \ll 1$. However, as the size and number of monomers in the aggregate increase, the computational time and resources necessary to predict the radiation characteristics of the aggregates, using any of these numerical methods, increases sharply [58, 85].

3.2.5 Equivalent particle approximations

Latimer [107] approximated fractal aggregates as coated spheres with equivalent volume and collision diameter. The coating had a relative complex index of refraction identical to that of the monomers constituting the aggregate while the core had the same index of refraction as the surrounding medium. The ratio of the total volume of monomers and the volume of the smallest sphere enclosing the aggregate was denoted by F and derived from fractal theory as [107]

$$F = N_s^{\left(1 - \frac{3}{D_f}\right)}. \tag{3.15}$$

This expression assumed that the aggregate formed a solid sphere when D_f was equal to 3.0. The resulting equivalent coated sphere had an outer diameter equal to the collision diameter of the aggregates. The inner $a_{i,L}$ and outer $a_{o,L}$ radii of the coated sphere were given by [107]

$$a_{i,L} = N_s^{1/3} a \left(1 - \frac{1}{F^{1/3}}\right) \quad \text{and} \quad a_{o,L} = \left(\frac{a^3 N_s}{F}\right)^{1/3} \tag{3.16}$$

Latimer [107] rationalized his approach by hypothesizing that the morphological features of aggregates composed of large monomers ($\chi_s >> 1$) did not have any effect on their radiation characteristics due to their random orientation. The author experimentally measured the scattered intensity of a 474 nm laser beam incident by aqueous suspensions of aggregates consisting of latex microspheres, with diameter ranging from 0.26 to 2.05 μm ($1.7 \le \chi_s \le 13.6$). Aggregates were formed by adding a concentrated NaCl solution to a suspension of monodisperse latex microspheres. For each suspension, 300-4000 aggregates were counted and were divided into five groups consisting of aggregates made of $N_s = 1, 4, 10, 32$, or 128 monomers. This monomer number distribution was used to generate the associated equivalent coated sphere size distribution for the inner and outer radii $a_{i,L}$ and $a_{o,L}$ [Equation (3.16)]. Then, the angular distribution of light scattered by the aggregate suspensions was predicted assuming that all aggregates had fractal dimension D_f of 2.25 [107]. Theoretical predictions of the scattered laser intensity fell within 15% of experimental measurements for scattering angles 0° to 10° for all aggregate suspensions. However, the relative error reached up to 80% for scattering angles greater than 90° [107]. Note that Latimer's choice to reduce the monomer number distribution of a large number of aggregates to only five discrete bins was arbitrary and may have introduced larger errors in the theoretical predictions of the scattering cross-section known to be very sensitive to the number of monomers N_s [56, 95]. Regardless, experimental characterization of the number of monomers in an aggregate is a challenging task even using 3D microscopy as monomers located at the surface of the aggregate obstruct the view of those inside. This results in underestimation of the monomer counts in large aggregates [92, 108]. Therefore, a more rigorous validation of Latimer's method of approximating radiation characteristics of aggregates as volume and collision diameter equivalent coated spheres must be performed. Recently, Heng *et al.* [109]

demonstrated that the absorption and scattering cross-sections and the asymmetry factor of bispheres, quadspheres, and rings of up to 20 spherical monomers can be approximated as those of coated spheres with equivalent volume and average projected area. The monomer size parameter ranged between 0.01 to 10 and the relative refraction n and absorption k indices were up to 1.5 and 0.1, respectively.

Finally, Morel and co-workers [110, 111] demonstrated that the radiation characteristics of spheroidal microorganisms with an aspect ratio smaller than 1.5 can be treated as those of spheres. In addition, Lee *et al.* [38] also established that randomly oriented spheroidal microalgae cells, with an average aspect ratio of 1.333, could be treated as spheres over the PAR region.

The present study aims to find a rapid and accurate method for predicting the radiation characteristics of fractal aggregates, in particular, those with a large number of monomers of large size parameter χ_s, beyond the range of validity of the RDG approximation. Absorption and scattering cross-sections as well as scattering matrix element ratios of fractal aggregates with fractal dimension ranging from 2.0 to 3.0 were computed using the superposition T-matrix method. These results were compared with predictions made by (1) the RDG approximation, (2) Latimer's coated sphere approximation, and (3) the volume and average projected area equivalent coated sphere approximation. Fractal aggregates composed of up to 1000 monodisperse or polydisperse spherical monomers featuring size parameter ranging from 0.01 to 20 were considered.

3.3   Methods

3.3.1   Fractal aggregate generation

First, fractal aggregates were generated using the particle cluster aggregation program validated and released by Mroczka and co-workers [91, 92, 112]. All monomers in the aggregate were in contact with each other but did not overlap. The fractal dimension was taken as $D_f = 2.25$ corresponding approximately to that of phytoplankton, as previously men-

tioned [62]. The fractal prefactor k_f was taken as 1.59 as prescribed by Sorensen [56] and Mroczka *et al.* [91]. The aggregates generated consisted of 2 to 1000 monomers featuring size parameter χ_s ranging from 0.01 to 20. In addition, ordered aggregates featuring integer fractal dimension D_f equal to 1.0, 2.0, and 3.0 were generated and corresponded to linear chain, square packing, and simple cubic packing of sphere, respectively.

The total volume V_T of an arbitrary aggregate with polydisperse spherical monomers of radius $(a_j)_{1 \leq j \leq N_s}$ can be written as

$$V_T = \sum_{j=1}^{N_s} \frac{4\pi}{3} a_j^3 \tag{3.17}$$

The radius $a_{eq,V}$ of the volume equivalent sphere can be expressed as

$$a_{eq,V} = \left(\frac{3}{4\pi} V_T \right)^{1/3}. \tag{3.18}$$

The radius $\langle a \rangle$ of the volume-averaged monomer is given by

$$\langle a \rangle = \left(\frac{3}{4\pi} \frac{V_T}{N_s} \right)^{1/3}. \tag{3.19}$$

The corresponding volume-averaged size parameter can be defined as $\langle \chi_s \rangle = 2\pi \langle a \rangle \lambda^{-1}$. Alternatively, the average monomer size parameter $\bar{\chi}_s$ for aggregates composed of polydisperse monomers can be estimated as

$$\bar{\chi}_s = \frac{1}{N_s} \sum_{j=1}^{N_s} \frac{2\pi a_j}{\lambda}. \tag{3.20}$$

For aggregates consisting of monodisperse monomers, the volume averaged monomer radius $\langle a \rangle$ is equal to the monomer radius a and $\langle \chi_s \rangle = \bar{\chi}_s = \chi_s$.

The average projected area $\bar{A}_p$ of the aggregates was estimated numerically using the method discussed in detail by Heng *et al.* [109]. In brief, the aggregate's center of mass was fixed with respect to the observer and the aggregate was rotated through a large number of discrete orientations. Then, the orientation-averaged area projected onto a plane normal to the line of sight was calculated. Then, the outer $a_{o,V+\bar{A}_p}$ and inner $a_{i,V+\bar{A}_p}$ radii of the volume and average projected area equivalent coated sphere, can be expressed as

$$a_{o,V+\bar{A}_p} = \left(\frac{\bar{A}_p}{\pi} \right)^{1/2} \quad \text{and} \quad a_{i,V+\bar{A}_p} = \left(a_{o,V+\bar{A}_p}^3 - \frac{3}{4\pi} V_T \right)^{1/3} \tag{3.21}$$

This ensures that the volume of the coating and the projected area of the equivalent coated sphere were the same as the total volume V_T and the average projected area $\bar{A}_p$ of the aggregate.

3.3.2 Radiation characteristic predictions

First, the orientation averaged absorption $\langle C_{abs}^a \rangle$ and scattering $\langle C_{sca}^a \rangle$ cross-sections and scattering matrix elements of aggregates consisting of monodisperse and polydisperse spherical monomers were predicted using the superposition T-matrix method using the program developed by Mackowski and Mishchenko [80]. The medium surrounding the aggregates was non-absorbing and had an index of refraction equal to that of water in the visible part of the spectrum, i.e., n_m=1.33. Unless stated otherwise, the monomers featured a complex index of refraction m_p=1.355+i0.003. This resulted in a relative complex index of refraction $m = m_p/n_m$ =1.0165+i0.003 representative of various microalgae species [35, 38]. The position of each monomer and their individual size parameter χ_s were prescribed while they were all assumed to have the same relative complex index of refraction m. Then, the orientation-averaged aggregate absorption $\langle Q_{abs}^a \rangle$ and scattering $\langle Q_{sca}^a \rangle$ efficiency factors were computed. Finally, the absorption $\langle C_{abs}^a \rangle$ and scattering $\langle C_{sca}^a \rangle$ cross-sections of the randomly oriented aggregates were estimated according to [80]

$$\langle C_{abs/sca}^a \rangle(N_s, \chi_s, m, D_f, k_f) = \langle Q_{abs/sca}^a \rangle(N_s, \chi_s, m, D_f, k_f)\pi a_{eq,V}^2 \tag{3.22}$$

where the volume equivalent sphere radius $a_{eq,V}$ is given by Equation (3.18).

Moreover, the orientation-averaged absorption $\langle C_{abs,RDG}^a \rangle$ and scattering $\langle C_{sca,RDG}^a \rangle$ cross-sections and the scattering phase function $F_{11,RDG}(\Theta)$ of the aggregates were predicted by the RDG approximation using Equations (3.8), (3.10), and (3.13), respectively. For aggregates composed of polydisperse monomers, the monomer size parameter χ_s in Equations (3.9) and (3.11) was replaced by the volume-averaged size parameter $\langle \chi_s \rangle$.

The absorption and scattering cross-sections and the scattering matrix elements of the volume and average projected area equivalent coated spheres were predicted based on Lorenz-

Mie theory using the program developed by Matzler [113]. First, their absorption and scattering efficiency factors were computed based on (i) the size parameters $\chi_{i,\bar{A}_p+V}$ and $\chi_{o,\bar{A}_p+V}$ associated with the inner $a_{i,V+\bar{A}_p}$ and outer $a_{o,V+\bar{A}_p}$ radii given by Equation (3.21) and (ii) the relative complex index of refraction m. Then, the absorption $\langle C_{abs,V+\bar{A}_p} \rangle$ and scattering $\langle C_{sca,V+\bar{A}_p} \rangle$ cross-sections were estimated according to

$$\langle C_{abs/sca,V+\bar{A}_p} \rangle (\chi_{i,\bar{A}_p+V}, \chi_{o,\bar{A}_p+V}, m) = \langle Q_{abs/sca,V+\bar{A}_p} \rangle (\chi_{i,\bar{A}_p+V}, \chi_{o,\bar{A}_p+V}, m) \pi a_{o,V+\bar{A}_p}^2 \quad (3.23)$$

Similarly, the absorption $\langle C_{abs,L} \rangle$ and scattering $\langle C_{sca,L} \rangle$ cross-sections corresponding to Latimer's equivalent coated sphere were estimated using Equation (3.23) by replacing the size parameters $\chi_{i,V+\bar{A}_p}$ and $\chi_{o,V+\bar{A}_p}$ with the size parameters $\chi_{i,L}$ and $\chi_{o,L}$ corresponding to the inner $a_{i,L}$ and outer $a_{o,L}$ radii given by Equation (3.16).

Finally, the relative errors in the absorption and scattering cross-sections of the aggregates between predictions by the superposition T-matrix method and the RDG and the equivalent coated sphere approximations were estimated in order to identify the best approximation method.

3.3.3   Retrieving the relative complex index of refraction

The suspensions used to illustrate the complex index of refraction retrieval method featured aggregates composed of monodisperse monomer with a monomer number distribution $p(N_s)$. Figures 3.2a and 3.2b show histograms of the monomer number distribution $p(N_s)$ for suspensions containing aggregates composed of monomers with size parameter of $\chi_s \leq 1$ and of $\chi > 1$, respectively. Each aggregate featured a fractal dimension D_f of 2.25 and k_f of 1.59 and was composed of N_s monodisperse monomers with a radius of 1 μm and a size parameter χ_s of 0.01, 0.1, 0.5, 1, 5, or 10. For aggregates composed of monomers of size parameter $\chi_s \leq 1$, the monomer number distribution $p(N_s)$ was taken as a Gaussian distribution with mean monomer number N_s of 36 monomers and a standard deviation of 20 monomers (Figure 3.2a). On the other hand, for aggregates composed of monomers of size parameters 5 and 10, $p(N_s)$ featured a mean N_s of 9 and a standard deviation of 5 monomers (Figure

[3.2](#)b).

Figures [3.3](#)a to [3.3](#)d show the histograms of inner and outer diameters distribution $p(a_{i,\bar{A}_p+V})$ and $p(a_{o,\bar{A}_p+V})$ of the volume and average projected area equivalent coated spheres, estimated using Equation ([3.21](#)), for suspensions consisting of aggregates composed of monomers with size parameter $\chi_s \leq 1$ and $\chi_s > 1$, respectively.

The suspension's total absorption $\langle C_{abs}^a \rangle_T$ and scattering $\langle C_{sca}^a \rangle_T$ cross-sections were predicted by the T-matrix method according to

$$\langle C_{abs/sca}^a \rangle_T = \frac{1}{N_T} \sum_{N_s=1}^{\infty} \langle C_{abs/sca}^a \rangle (N_s, \chi_s) p(N_s) \tag{3.24}$$

Here, N_T represented the total number of aggregates in the suspension defined as

$$N_T = \sum_{N_s=1}^{\infty} N_s p(N_s) \tag{3.25}$$

where $\sum_1^{\infty} p(N_s) = 1$.

Figure [3.4](#) shows the schematic diagram of the procedure used to retrieve the relative complex index of refraction $m = n + ik$ of the monomers. The Lorenz-Mie theory for coated spheres was used in the forward model to calculate the total absorption $\langle C_{abs,\bar{A}_p+V}^a \rangle_T$ and scattering $\langle C_{sca,\bar{A}_p+V}^a \rangle_T$ cross-sections of the aggregates. Then, the general purpose genetic algorithm PIKAIA [48] was used to efficiently and simultaneously find values of the relative refraction n and absorption k indices that minimized the difference between the absorption and scattering cross-sections obtained using the T-matrix method and the ones predicted using the equivalent coated sphere approximation in the inverse method. The use of a genetic algorithm such as PIKAIA provides a method to optimize and accelerate the search for the global minimum of an objective function [48]. Here, the objective function δ was defined as

$$\delta = \left(\frac{\langle C_{abs}^a \rangle_T - \langle C_{abs,\bar{A}_p+V}^a \rangle_T}{\langle C_{abs}^a \rangle_T} \right)^2 + \left(\frac{\langle C_{sca}^a \rangle_T - \langle C_{sca,\bar{A}_p+V}^a \rangle_T}{\langle C_{sca}^a \rangle_T} \right)^2 \tag{3.26}$$

The relative refraction index n was assumed to range between 1 and 1.15 while the absorption index k was allowed to range from 10^{-5} to 1. The genetic algorithm used a maximum of 500 generations and a population of 120 individuals. The convergence criterion was set as $\delta < 10^{-4}$.

(a)

$\chi_s \leq 1$

mean = 36
stdev = 20

(b)

$\chi_s > 1$

mean = 9
stdev = 5
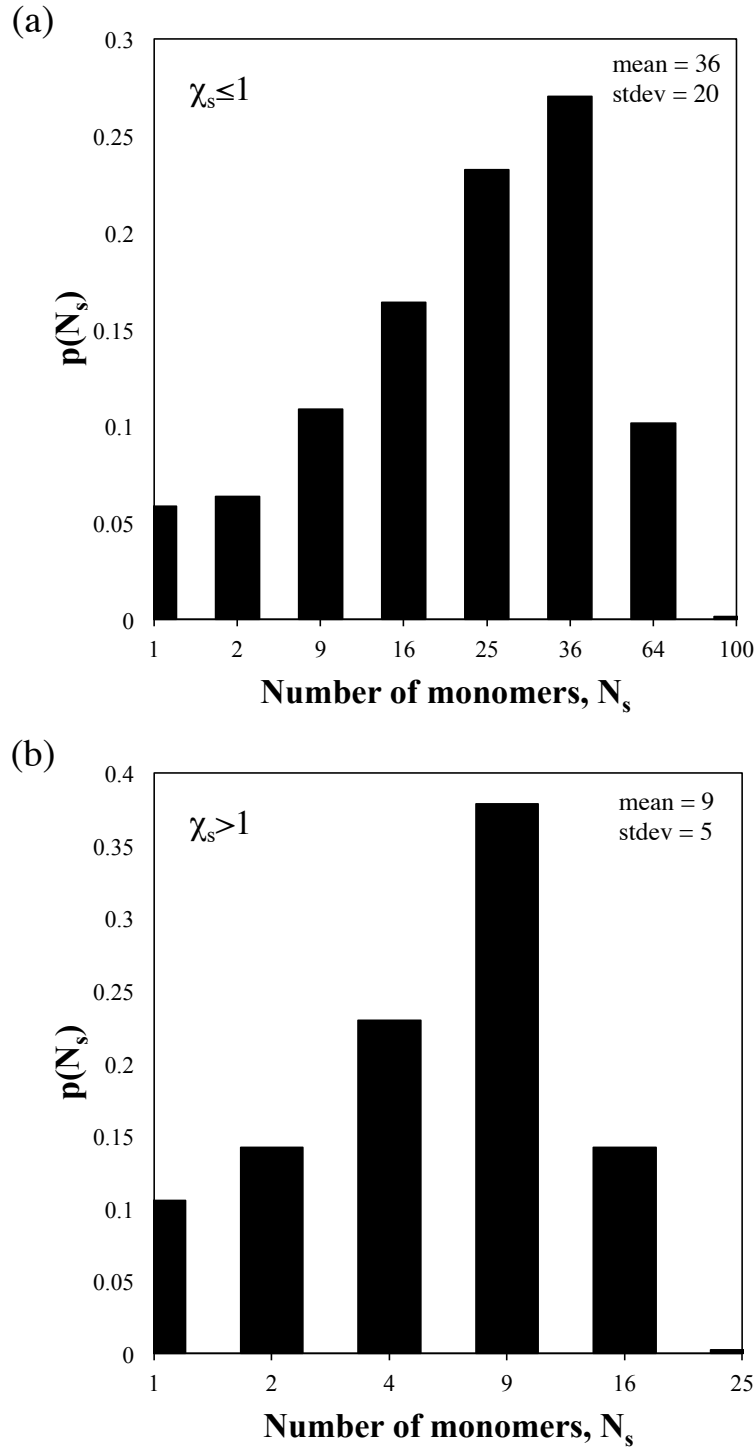
Figure 3.2: Histograms showing monomer number distribution $p(N_s)$ of aggregates composed of monodisperse monomers with (a) size parameter $\chi \leq 1$ and (b) size parameter $\chi_s > 1$.

(a)

(b)
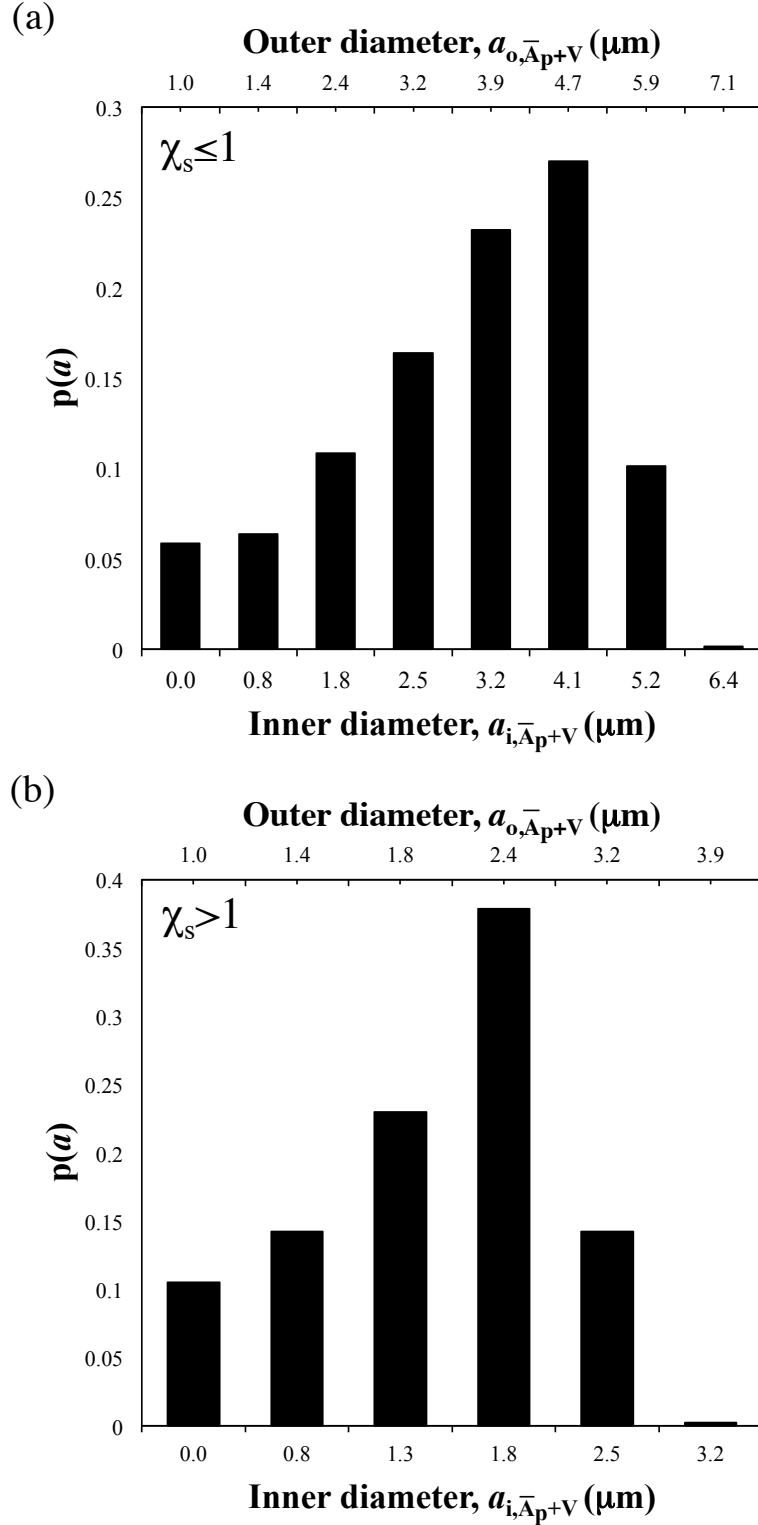
Figure 3.3: Histograms showing inner $a_{i,\bar{A}_p+V}$ and outer $a_{o,\bar{A}_p+V}$ equivalent coated sphere diameters $p(a)$ of aggregates composed of monodisperse monomers with (a) size parameter $\chi \leq 1$ and (b) size parameter $\chi_s > 1$.
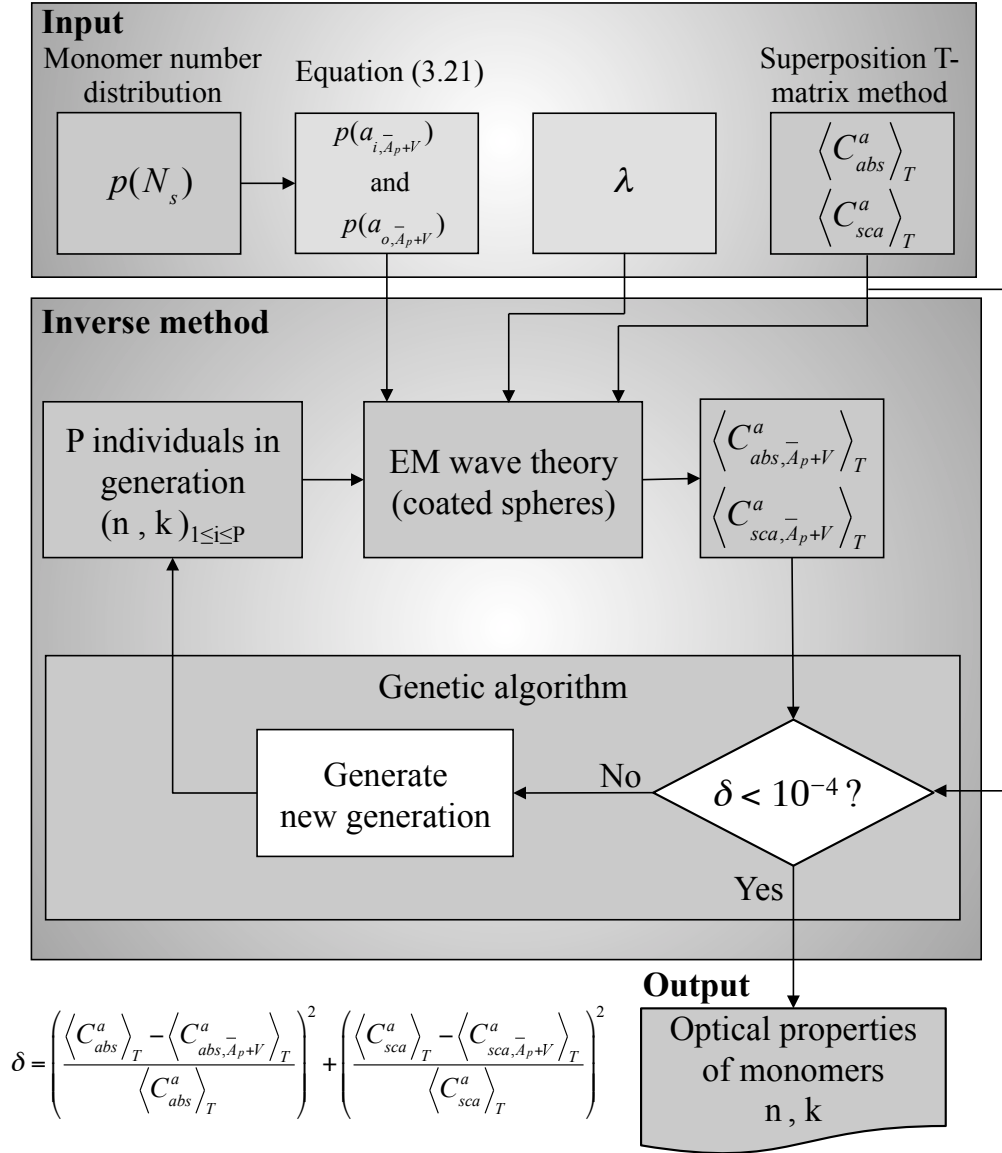
Figure 3.4: Block diagram of the procedure used to retrieve relative refraction n and absorption k indices from the absorption $\langle C^a_{abs}\rangle_T$ and scattering $\langle C^a_{sca}\rangle_T$ cross-sections for suspensions containing aggregates with monomer number distribution $p(N_s)$.

3.4 Results

3.4.1 Average projected area

First, the average projected area $\bar{A}_p$ of aggregates composed of monodisperse monomers was computed using the code developed by Heng *et al.* [109]. The monomers had radius a equal to 1, 5, or 10 μm. The number of monomers per aggregates N_s ranged from 2 to 1000 while the fractal dimension D_f was taken as 1.0, 1.75, 2.0, 2.25, 2.5, or 3.0. In all cases, for aggregates of a given fractal dimension D_f and monomers number N_s, the ratio $\bar{A}_p/a^2$ was found to be constant. Figure 3.5 plots the dimensionless ratio $\bar{A}_p/a^2$ as a function of the number of monomers N_s in the aggregate for different values of D_f. It indicates that $\bar{A}_p/a^2$ increased with the number of monomers N_s for all fractal dimensions considered. Moreover, for aggregates with identical monomer number N_s and radius a, the average projected area increased with decreasing fractal dimension D_f. This was consistent with fractal theory which dictates that aggregates with larger fractal dimension feature a more compact structure [56]. Finally, the ratio $\bar{A}_p/a^2$ was fitted by the least squares method to a power-law in terms of N_s to yield

$$\frac{\bar{A}_p}{a^2} = \pi N_s^\alpha \tag{3.27}$$

where the exponent α was a function of fractal dimension D_f. The constant π was used to ensure the validity of Equation (3.27) in the limiting case of a single sphere when $N_s = 1$ and $\bar{A}_p = \pi a^2$. The power α was found to decrease monotonously from α_{max} of 0.92 for linear chains of spheres with $D_f = 1.0$ to α_{min} of 0.73 for $D_f = 3.0$. The inset of Figure 3.5 shows the reduced variables $\alpha^* = (\alpha - \alpha_{min})/(\alpha_{max} - \alpha_{min})$ plotted versus $D_f^* = (D_f - 1)/2$ whose least-squares fitting yielded the following correlation

$$\alpha^* = \left(1 + D_f^{*1.8}\right)^{1/1.8} \tag{3.28}$$

For both power-law fits of Equations (3.27) and (3.28), the coefficient of determination R^2 was larger than 0.99. The average projected area estimated by Equations (3.27) and (3.28)
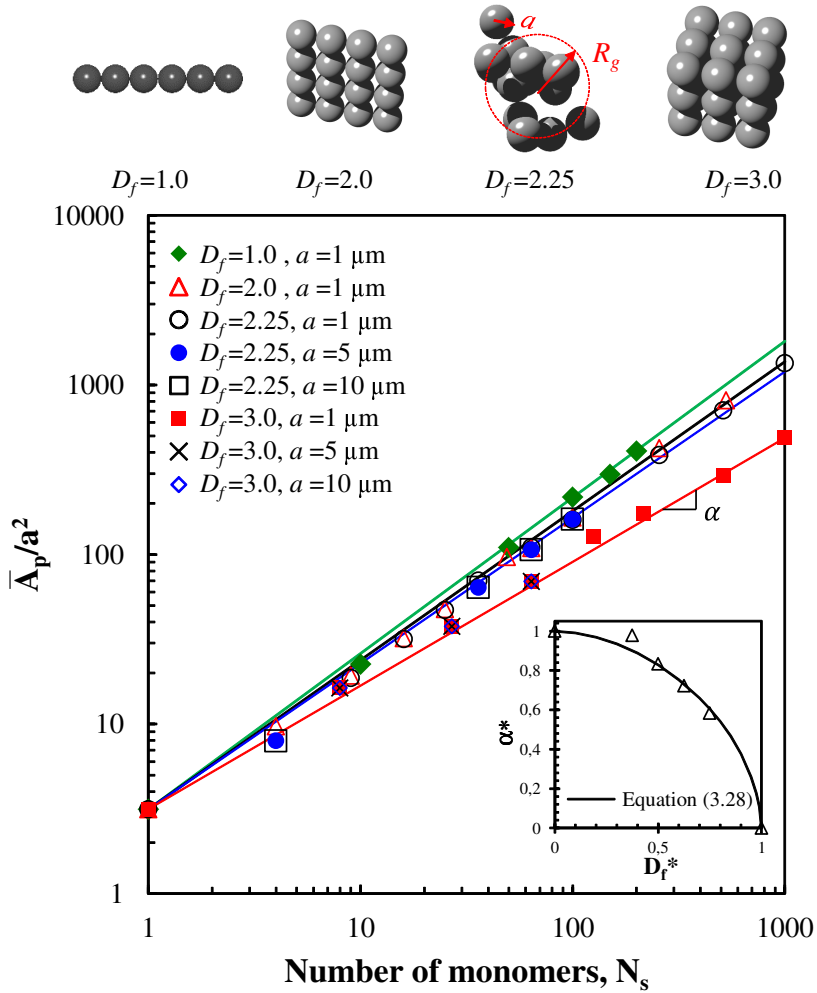
Figure 3.5: The ratio $\bar{A}_p/\mathrm{a}^2$ as a function of number N_s of monodisperse monomers in an aggregate for fractal dimension D_f equal to 1.0, 1.75, 2.0, 2.25, 2.5, and 3.0 and monomer radii a equal to 1, 5, and 10 μm.

was used to predict the outer radius $a_{o,V+\bar{A}_p}$ of the equivalent coated sphere according to Equation (3.21).

3.4.2 Absorption and scattering cross-sections

3.4.2.1 Effect of aggregate fractal dimension

Figures 3.6a to 3.6c show the absorption $\langle C^a_{abs} \rangle$ and scattering $\langle C^a_{sca} \rangle$ cross-sections of randomly oriented aggregates as functions of the number of monodisperse monomers N_s ranging from 2 to 1000 for fractal dimension D_f equal to 2.0, 2.25, and 3.0, respectively. Each monomer featured radius a equal to 1 μm and size parameter χ_s equal to 1, while its relative complex index of refraction m was equal to $1.0165 + i0.003$. Note that the monomer size parameter χ_s of 1 was chosen because it falls outside the Rayleigh scattering regime and it was the largest size parameter for which computation of aggregates containing as many as 1000 monomers was possible. Figures 3.6a to 3.6c also compare the absorption and scattering cross-sections predicted by the superposition T-matrix method with those estimated by (i) the RDG approximation, (ii) Latimer's coated sphere approximation, and (iii) the equivalent volume and average projected area coated sphere approximation. In all cases, the absorption cross-section $\langle C^a_{abs} \rangle$ was proportional to the number of monomers N_s. In fact, $\langle C^a_{abs} \rangle$ was independent of the fractal prefactor and dimension k_f and D_f. In addition, for all values of N_s and D_f investigated, the three different approximations considered predicted aggregate absorption cross-section $\langle C^a_{abs} \rangle$ within less than 1% of predictions by the superposition T-matrix method. This can be attributed to the fact that, for aggregates composed of monomers with relatively small absorption index k, (i.e., optically soft), absorption is a volumetric phenomenon and, for all approximations, the volume of material interacting with the incident electromagnetic wave was identical to the total volume V_T of the aggregates. Thus, for aggregates composed of monodisperse monomers, Equation (3.8) can also be expressed as $\langle C^a_{abs} \rangle = V_T/V_s \langle C_{abs} \rangle$, where V_s corresponds to the volume of a single monomer. In other words, the aggregate absorption cross-section $\langle C^a_{abs} \rangle$ was proportional to its total volume V_T. The same conclusion was reached for linear chains of spheres [85] and for bispheres, quadspheres, and rings of spheres [109] made of optically soft monomers.

Similarly, the scattering cross-section $\langle C^a_{sca} \rangle$ increased as a function of number of monomers
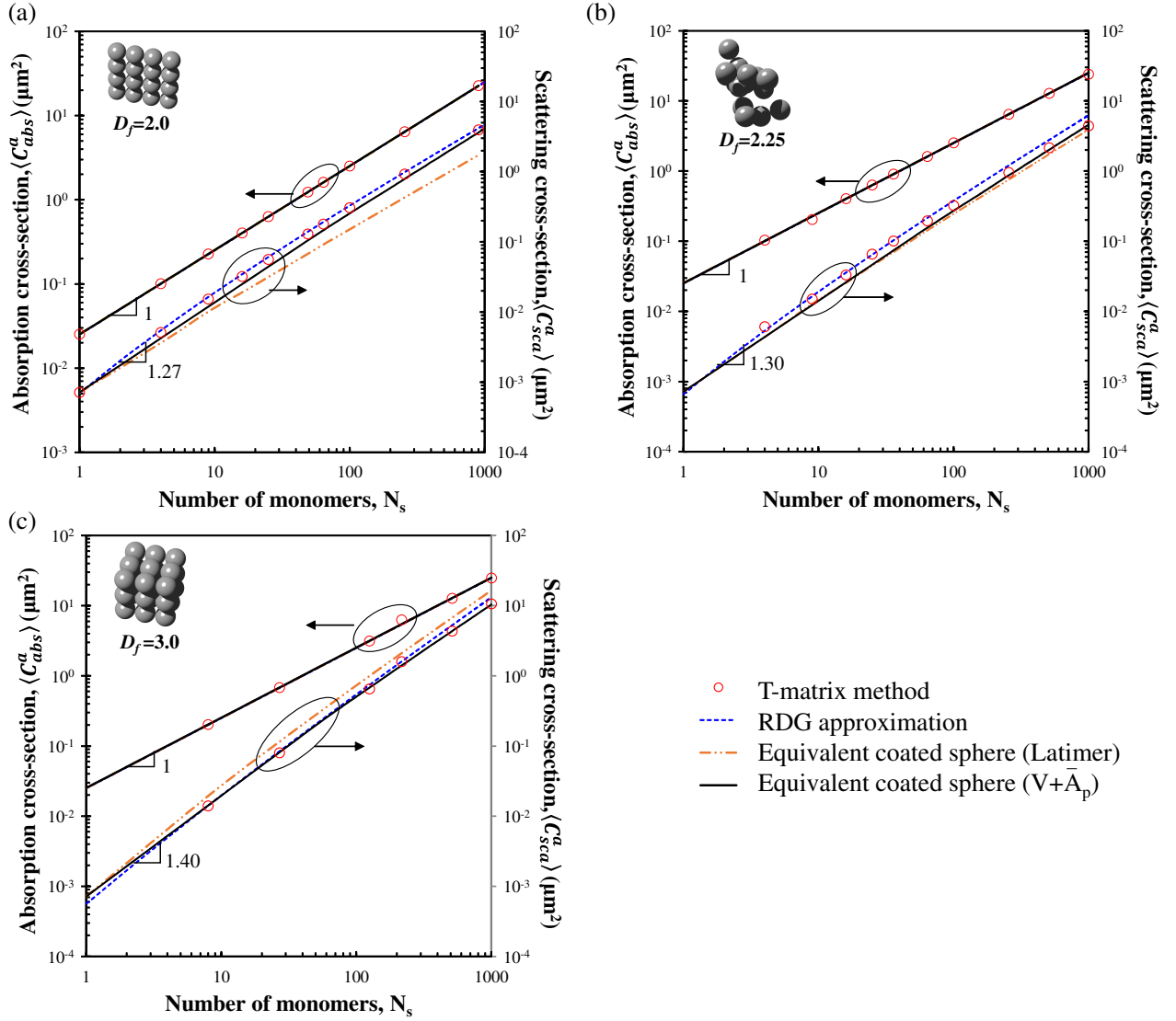
Figure 3.6: Absorption $\langle C_{abs}^a \rangle$ and scattering $\langle C_{sca}^a \rangle$ cross sections as functions of monomer number N_s in randomly oriented aggregates with fractal dimension D_f of (a) 2.0, (b) 2.25, and (c) 3.0 predicted using the superposition T-matrix method, the RDG approximation, Latimer's [107] coated sphere approximation, and the volume and average projected area equivalent coated sphere approximation. The aggregates were composed of monodisperse monomers featuring size parameter $\chi_s = 1$ and $m = 1.0165 + i0.003$.

N_s present in the aggregates. Here, $\langle C_{sca}^a \rangle$ was proportional to N_s^p where the power p was equal to 1.27, 1.30, and 1.40 for aggregates with fractal dimension D_f of 2.0, 2.25, and 3.0, respectively. Thus, unlike for $\langle C_{abs}^a \rangle$, the scattering cross-section of the aggregate was larger than the sum of the scattering cross-sections of each monomer (i.e., $p > 1$) due to multiple scattering. In fact, for a given number of monomers N_s and a given total volume V_T, the aggregates with larger fractal dimension D_f featured larger scattering cross-sections $\langle C_{sca}^a \rangle$. This was due to the fact that increasing the fractal dimension D_f resulted in a smaller average projected area (Figure 3.5) and a more compact structure more prone to multiple scattering [103]. The relative error between scattering cross-section $\langle C_{sca}^a \rangle$ predicted by the T-matrix method and that estimated by the RDG approximation was smaller than 15% for aggregates containing fewer than 100 monomers for any fractal dimension D_f considered. However, it reached up to 40% for aggregates containing 100 or more monomers. On the other hand, the relative error in the scattering cross-section predicted by Latimer's coated sphere approximation was smaller than 18% for fractal dimension D_f equal to 2.25 corresponding to the value of D_f validated by Latimer [107]. However, it reached up to 47% for fractal dimensions D_f of 2.0 and 3.0. Due to the relatively large discrepancies between predictions by the T-matrix method and by Latimer's approximation [107], the latter was omitted in the remainder of this study. By contrast, the scattering cross-section of the volume and average projected area equivalent coated sphere fell within 7.5% of that predicted by the T-matrix method for all values of N_s and D_f considered. Note that predictions of the integral radiation characteristics for the volume-equivalent or surface-area-equivalent homogeneous spheres were not as accurate as those for the volume and average projected area equivalent coated sphere.

3.4.2.2 Effect of size parameter

Figures 3.7a to 3.7d show the absorption $\langle C_{abs}^a \rangle$ and scattering $\langle C_{sca}^a \rangle$ cross-sections of randomly oriented aggregates of monodisperse monomers with fractal dimension $D_f = 2.25$ as a function of monomer number N_s for size parameter χ_s equal to 0.01, 0.1, 0.5, 5, 10, and 20.
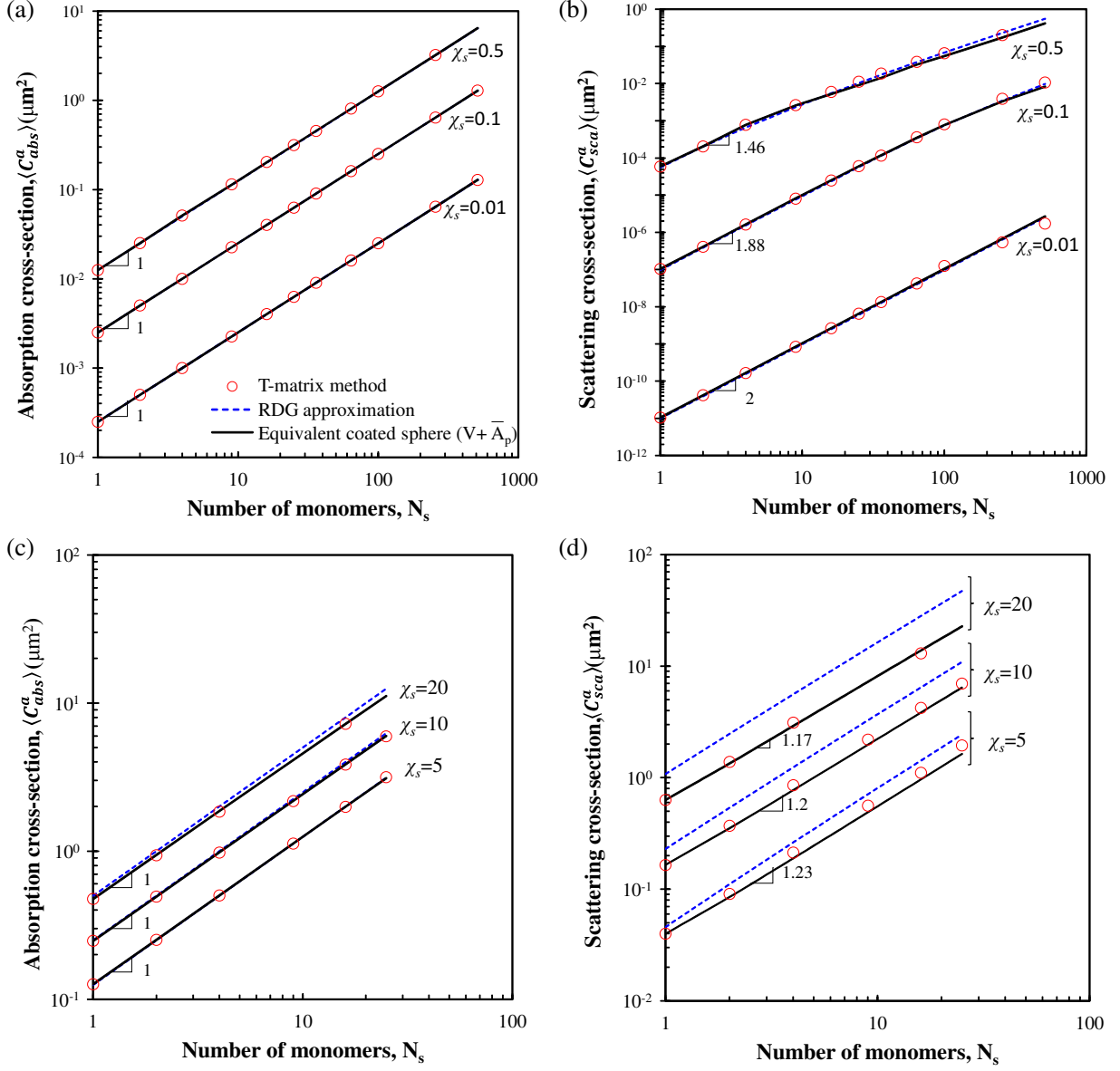
Figure 3.7: (a,c) Absorption $\langle C_{abs}^a \rangle$ and (b,d) scattering $\langle C_{sca}^a \rangle$ cross-sections as functions of monomer number N_s in randomly oriented aggregates with fractal dimension $D_f = 2.25$ and composed of monomers with $m = 1.0165 + i0.003$ and size parameter χ_s ranging from 0.01 to 20 predicted using (i) the superposition T-matrix method, (ii) the RDG approximation, and (iii) the volume and average projected area equivalent coated sphere approximation.

They compare the superposition T-matrix predictions with those of the RDG approximation and for the volume and average projected area equivalent coated sphere. They indicate that both absorption $\langle C_{abs}^a \rangle$ and scattering $\langle C_{sca}^a \rangle$ cross-sections increased with increasing number of monomers N_s and size parameter χ_s. More specifically, Figures 3.7a and 3.7c establish that the aggregate absorption cross-section $\langle C_{abs}^a \rangle$ was linearly proportional to the number of monomers N_s for all size parameters considered. On the other hand, Figure 3.7b reveals that the aggregate scattering cross-section $\langle C_{sca}^a \rangle$ was proportional to N_s^2 for aggregates composed of monomers of size parameter $\chi_s = 0.01$. It is interesting to note that, in the limiting case of for small size parameter χ_s and small aggregates such that $\chi_s << 1$ and $qR_g << 1$, the RDG approximation predicts that $\langle C_{sca}^a \rangle$ is proportional to N_s^2. Figures 3.7b and 3.7d indicate that $\langle C_{sca}^a \rangle$ was proportional to N_s^p with a power-law exponent p that monotonously decreased from 2 to 1.17 as the monomer size parameter χ_s increased from 0.01 to 20. In fact, in the limiting case of large size parameter χ_s and large aggregates, i.e., $\chi_s >> 1$ and $qR_g >> 1$, the RDG approximation predicts that $\langle C_{sca}^a \rangle$ is linearly proportional to N_s (i.e., $p = 1$), as previously mentioned.

The absorption cross-section predicted by the RDG approximation and the volume and average projected area equivalent coated sphere fell within 5% of the T-matrix predictions for all values of N_s and χ_s considered. In addition, the relative error in scattering cross-section predictions by the RDG approximation was smaller than 8% for size parameter χ_s smaller than 0.5. However, it reached 29%, 56%, and 117% for size parameters χ_s of 5, 10, and 20, respectively. This excessively large relative error in scattering cross-section renders the RDG approximation unsuitable for predicting the radiation characteristics of aggregates composed of monomers of size parameter larger than 1, as previously reported in the literature [86, 89, 98, 99]. By contrast, the scattering cross-section of the volume and average projected area equivalent coated sphere fell within 10% of the predictions by the T-matrix method for all values of N_s and χ_s considered. In other words, the volume and average projected area equivalent coated sphere was able to capture the multiple scattering effects. on the integral radiation characteristics.

Moreover, that the maximum number of monomers per aggregate that could be simulated decreased with increasing monomer size parameter χ_s. For example, a converged solution for aggregates of 25 monomers of size parameter $\chi_s = 20$ could not be obtained using the superposition T-matrix program despite the use of a relatively large computer cluster. What is more, for a fractal aggregate containing 25 monomers of size parameter $\chi_s = 10$, the superposition T-matrix code yielded a converged solution after 25 hours running in parallel on 135 CPUs. Alternatively, predictions of the radiation characteristics and scattering matrix elements of the corresponding volume and average projected area equivalent coated spheres were obtained in 3.6 ms using a computer with a single core CPU. Thus, this approximation could provide an invaluable tool for estimating the radiation characteristics of randomly oriented aggregates with reasonable accuracy, particularly for aggregates with a large number of large monomers. For example, it could be used in inverse problems aiming to infer the aggregate morphology and/or the monomer complex index of refraction from experimental measurements [38, 87, 114, 115]. It could also be used when the superposition T-matrix method fails to converge or if the necessary computing resources are not available. This is particularly interesting for microalgae colonies consisting of cells 4-12 μm in diameter (Figures 3.1e and 3.1f) and featuring size parameter χ_s ranging between 18 and 95 over the photosynthetically active radiation region (λ=400-700 nm). For such suspensions the volume and average projected area equivalent coated sphere approximation can predict the absorption and scattering cross-sections as well as the asymmetry factor g or the backward scattering fraction b needed to perform radiation transfer analysis in PBRs [78, 116].

3.4.2.3 Effect of polydispersity

To investigate the effects of monomer polydispersity on the aggregates' absorption and scattering cross-sections, aggregates composed of 256, 512, and 1000 polydisperse monomers were generated with a Gaussian radius distribution with the same mean radius of 1 μm and standard deviation of 10% or 25%. Table 3.1 reports the mean $\bar{\chi}_s$ and volume-averaged $\langle \chi_s \rangle$ size parameters and the average projected area of the aggregates generated. It also com-

pares predictions of the corresponding absorption $\langle C_{abs}^a \rangle$ and scattering $\langle C_{sca}^a \rangle$ cross-sections by the superposition T-matrix method with those made by the RDG and the volume and average projected area equivalent coated sphere approximations. In all cases, the monomer mean size parameter $\bar{\chi}_s$ was equal to 1 and the fractal dimension D_f was equal to 2.25. However, the total volume V_T and the volume-averaged size parameter $\langle \chi_s \rangle$ of the aggregates with polydisperse monomers were larger than those with monodisperse monomers for the same number of monomers N_s. On the other hand, the average projected area $\bar{A}_p$ of the aggregates increased only slightly with polydispersity of the monomers. Overall, the ratio $\bar{A}_p/V_T$ of the average projected area to the total volume was smaller for aggregates with polydisperse monomers than with monodisperse monomers having the same monomer number and mean radius. In other words, aggregates with polydisperse monomers were more compact that those with monodisperse monomers. Moreover, for all cases considered, aggregates composed of polydisperse monomers featured larger absorption and scattering cross-sections than those composed of the same number of monodisperse monomers N_s. The larger absorption cross-section was due to the fact that the total volume of the aggregates V_T increased with increasing monomer polydispersity, as reported in Table 3.1. On the other hand, the increase in aggregate scattering cross-section $\langle C_{sca}^a \rangle$ could be attributed to the fact that the aggregates were more compact and therefore more prone to multiple scattering. These results were consistent with the conclusion reached for aggregates with monodisperse monomers and different fractal dimensions (Figure 3.6).

Table 3.1: Absorption $\langle C_{abs}^a \rangle$ and scattering $\langle C_{sca}^a \rangle$ cross-sections of randomly oriented aggregates of fractal dimension D_f of 2.25 composed of monomers with a Gaussian radius distribution and standard deviations of 0%, 10%, and 25%. The aggregates were composed of 256, 512, and 1000 monomers with mean size parameter $\bar{\chi}_s=1$ and relative complex index of refraction $m = 1.0165 + i0.003$.

N_s	stdev χ_s (%)	$\langle \chi_s \rangle$	V_T (μm^3)	$\bar{A}_p$ (μm^2)	T-matrix		Rayleigh-Debye-Gans approximation				Equivalent coated sphere			
					$\langle C_{abs}^a \rangle$ (μm^2)	$\langle C_{sca}^a \rangle$ (μm^2)	$\langle C_{abs,RDG}^a \rangle$ (μm^2)	error (%)	$\langle C_{sca,RDG}^a \rangle$ (μm^2)	error (%)	$\langle C_{abs,V+\bar{A}_p}^a \rangle$ (μm^2)	error (%)	$\langle C_{sca,V+\bar{A}_p}^a \rangle$ (μm^2)	error (%)
256	0	1.00	1072	386	6.44	0.96	6.4	0.62	1.14	-19	6.4	0.01	0.83	14
256	10	1.01	1093	389	6.63	1.01	6.6	0.60	1.18	-17	6.6	0.3	0.91	10
256	25	1.08	1335	424	8.03	1.42	8.0	0.75	1.55	-9.2	8.0	0	1.2	14
512	0	1.00	2145	707	12.9	2.18	12.8	0.78	2.64	-21	12.9	0.2	2.0	10
512	10	1.00	2145	711	12.8	2.14	12.7	0.78	2.61	-22	12.8	0	2.0	8.4
512	25	1.06	2567	768	15.4	2.89	15.3	0.65	3.4	-18	15.4	0	2.7	8.0
1000	0	1.00	4189	1341	24.1	4.39	25.0	-3.4	5.9	-34	25.1	4.0	4.4	-0.5
1000	10	1.02	4376	1365	26.0	4.78	25.8	0.77	6.2	-29	26.0	0	4.5	5.7
1000	25	1.07	5059	1408	30.3	6.2	30.2	0.33	7.7	-24	30.3	0	5.9	5.7

Finally, the absorption cross-sections of the randomly oriented aggregates with polydisperse monomers predicted by both the RDG and the volume and average projected area equivalent coated sphere approximations fell within 4% of the predictions by the superposition T-matrix method. However, the associated scattering cross-section predicted by the RDG approximation suffered from a relative error of up to 29% for aggregates containing 1000 monomers. By contrast, the relative error in the scattering cross-section predicted for the volume and average projected area equivalent coated sphere was less than 14% for all aggregates considered. This confirms the validity of volume and average projected area equivalent coated sphere approximation in predicting the absorption and scattering cross-sections of randomly oriented fractal aggregates consisting of either monodisperse or polydisperse optically soft monomers.

3.4.2.4 Effect of the relative complex index of refraction

Figures 3.8a and 3.8b plot the absorption and scattering cross-sections of randomly oriented aggregates normalized by the product of the monomer number N_s and the absorption and scattering cross-sections of a single spherical monomer $\langle C_{abs}^a \rangle / N_s \langle C_{abs} \rangle$ and $\langle C_{sca}^a \rangle / N_s \langle C_{sca} \rangle$ as a function of N_s, respectively. All aggregates featured a fractal dimension D_f of 2.25, monodisperse monomers with size parameter $\chi_s = 1$, and relative refractive index $n = 1.0165$. The relative absorption index k was taken as 0.003, 0.03, 0.07, or 0.5. A ratio $\langle C_{abs}^a \rangle / N_s \langle C_{abs} \rangle$ or $\langle C_{sca}^a \rangle / N_s \langle C_{sca} \rangle$ independent of N_s and equal to unity would indicate that the absorption or scattering cross-section of the aggregate is the sum of absorption or scattering cross-sections of its constituent monomers. In fact, the normalized absorption cross-section per monomer $\langle C_{abs}^a \rangle / N_s \langle C_{abs} \rangle$ remained constant and equal to unity for aggregates with relative absorption index $k = 0.003$. This was consistent with the RDG approximation expression for $\langle C_{abs,RDG}^a \rangle$ given by Equation (3.8). However, for relative absorption index larger than 0.003, the normalized absorption cross-section was smaller than 1.0 and decreased with increasing values of N_s and k. Similar observations were made by Liu *et al.* [101] for soot aggregates composed of monomers with absorption index k of 0.6 and size parameter χ_s of 0.354, as
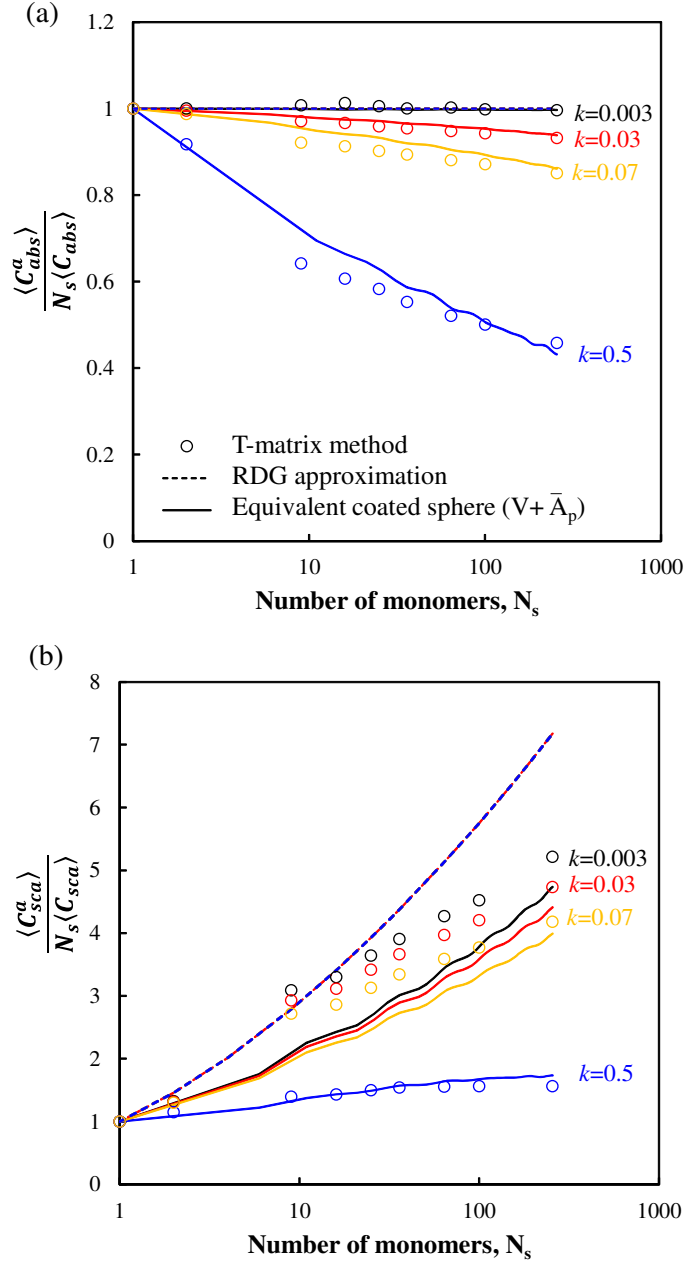
Figure 3.8: Normalized (a) absorption $\langle C_{abs}^a \rangle / N_s \langle C_{abs} \rangle$ and (b) scattering $\langle C_{sca}^a \rangle / N_s \langle C_{sca} \rangle$ cross-sections as a function of N_s predicted by the superposition T-matrix method, the RDG approximation, and the volume and average projected area equivalent coated sphere approximation for different values of relative absorption index k. All aggregates had fractal dimension $D_f = 2.25$, monomer size parameter $\chi_s = 1$, and relative refraction index $n = 1.0165$.

previously discussed. This can be attributed to the shading of the monomers located inside the aggregates by those located on the outside. This phenomenon was particularly important for aggregates composed of large, numerous, and/or strongly absorbing monomers. In addition, the scattering cross-section of aggregates composed of strongly absorbing monomers was much larger than for those composed of weakly absorbing monomers. These relatively large absorption and scattering cross-sections caused the incident electromagnetic wave to be fully attenuated before it can reach the inner monomers. For such aggregates, the absorption cross-section did not depend linearly on the material volume interacting with the incident radiation, unlike what has been observed for optically soft particles aggregates [100, 105]. Instead, when the penetration depth was smaller than the monomer size, absorption became a surface phenomenon.

Moreover, the normalized scattering cross-section per monomer represented by $\langle C_{sca}^a \rangle / N_s \langle C_{sca} \rangle$, increased with increasing N_s and was larger than 1.0 for all four complex indices of refraction considered. In other words, the scattering cross-section of an aggregate was larger than the sum of the scattering cross-sections of its constitutive monomers. This can be attributed to multiple scattering as previously discussed. However, the latter was less significant for aggregates composed of strongly absorbing monomers due to the attenuation of the electromagnetic wave which could not emerge from the aggregate. Note that Mishchenko [117] presented the equality $\langle C_{ext}^a \rangle = N_s \langle C_{ext} \rangle$ as a necessary condition for single scattering to prevail in multi-particle aggregates. Moreover, the RDG approximation predictions of $\langle C_{abs}^a \rangle / N_s \langle C_{abs} \rangle$ and $\langle C_{sca}^a \rangle / N_s \langle C_{sca} \rangle$ as a function of N_s were independent of the relative absorption index k. This resulted in very large discrepancies with predictions by the superposition T-matrix method. On the other hand, the volume and average projected area equivalent coated sphere predictions featured a relative error in the absorption and scattering cross-sections of less than 8% and 29%, respectively, compared with the T-matrix method for all values of N_s and k considered. Moreover, the relative error between predictions by the coated sphere approximation and by the T-matrix method decreased with increasing monomer absorption index. Indeed, the maximum relative error in the scattering cross-section was 29% and 11%

for aggregates composed of monomers with relative complex index of refraction m equal to $1.0165 + i0.003$ and $1.0165 + i0.5$, respectively. This was in contrast to the relative error between the RDG approximation and the superposition T-matrix method predictions which increased with monomer absorption index. In fact, the scattering cross-sections estimated by the RDG approximation differed by more than 50% from those by the T-matrix method for aggregates composed of more than $N_s = 100$ monomers with size parameter $\chi_s = 1$ and relative absorption index k larger than 0.03. These results establish that the volume and average projected area equivalent coated sphere approximation could not only capture the effects of multiple scattering but also of shading among monomers. Finally, these results indicate that the formation of colonies of microalgae in PBRs results in reduced absorption cross-section per cell and increased scattering cross-section per cell. Therefore, light transfer in microalgae suspensions will be strongly affected by colony formation.

3.4.3 Scattering phase function

Figures 3.9a to 3.9f show the scattering phase function $F_{11}(\Theta)$ of randomly oriented aggregates of fractal dimension D_f of 2.25 consisting of monomers of size parameter χ_s of 1 and 5 for a number of monomers N_s ranging from 9 to 100. They compare predictions by the superposition T-matrix method with those of (i) the RDG approximation, (ii) the volume and average projected area equivalent coated sphere approximation, and (iii) the Henyey-Greenstein phase function given by Equation (3.7) using the asymmetry factor g corresponding to the phase function of the equivalent coated sphere.

First, scattering by randomly oriented aggregates was increasingly in the forward direction as the size parameter χ_s and/or the number of monomers N_s in the aggregate increased. Figures 3.9a to 3.9c, corresponding to $\chi_s = 1$, confirm the conclusions reached by Manickavasagam and Mengüç [96] that measurements of aggregate scattering phase function alone could not be used to identify the monomer size parameter χ_s or their number N_s for size parameter χ_s between 0.5 and 1.5. Indeed, these three aggregates did not feature any distinguishing characteristics that could be used to determine either χ_s or N_s. On the other

hand, aggregates composed of monomers of size parameter $\chi_s = 5$ featured scattering phase functions $F_{11}(\Theta)$ with two distinct resonance peaks at scattering angles Θ of 55° and 100°. These angles depended only on the monomer size parameter χ_s. However, the magnitude of these resonance peaks correlated to the number of monomer in the aggregate N_s. Therefore, these two unique features of the scattering phase function could be used to determine the monomer's size parameter χ_s and number N_s in aggregates composed of relatively large monomers.

Moreover, the approximate methods predicted similar phase functions for the aggregates composed of monomers of size parameter χ_s of 1. However, the equivalent coated sphere scattering phase function featured several resonance peaks at various scattering angles Θ. These peaks did not correspond to those observed in the phase function predicted by the T-matrix method. The number and magnitude of these resonance peaks increased with increasing monomer number N_s and size parameter χ_s. These resonance peaks are characteristic of coated spheres [118] and were due to internal reflection within the coating which acted as a waveguide.

Another indicator of multiple scattering is the aggregate scattering phase function at $\Theta = 0^o$. Indeed single scattering by the aggregates requires that $F_{11}(0^o) = N_s F_{11,s}(0^o)$, where $F_{11,s}$ is the scattering phase function of a single sphere [117]. Here, the values of $F_{11}(0^o)$ for aggregates composed of 9 and 36 monomers of size parameter 1 and relative complex index of refraction $m = 1.0165 + i0.003$ was equal to 19.9 and 79.6, respectively. On the other hand, $F_{11,s}(0^o)$ for a single monomer of the same size parameter was equal to 2.21. Similarly, $F_{11}(0^o)$ was 244 and 309 for aggregates composed of 16 and 25 monomers of size parameter 5, respectively. The corresponding $F_{11,s}(0^o)$ was equal to 24.7. This further establishes the presence of multiple scattering in the aggregates considered in Figure 3.9.

The inset tables in Figures 3.9a to 3.9f report the asymmetry factor g corresponding to the scattering phase function predicted by the T-matrix method, the RDG approximation, and the volume and average projected area equivalent coated sphere approximation. They indicate that the asymmetry factor g increased from 0.62 for $\chi_s = 1$ and $N_s = 9$ to 0.96 for

$\chi_s = 5$ and $N_s = 25$. The relative error in the asymmetry factor g predicted by the RDG approximation reached 10% compared with the T-matrix method predictions for $\chi_s = 5$ and $N_s = 25$. However, it was smaller than 5% for the volume and average projected area equivalent coated sphere for all values of χ_s and N_s considered. The asymmetry factor can be used in various approximate expressions of the scattering phase function including the transport approximation [119] and the HG approximate phase function. In fact, the latter gave reasonable predictions of $F_{11}(\Theta)$ of the aggregates for $\chi_s = 1$ using the asymmetry factor corresponding to the equivalent coated sphere (Figures 3.9a to 3.9c). Note that large errors were observed for aggregates with larger monomers ($\chi_s >> 1$) which tend to scatter strongly in the forward direction (Figures 3.9d to 3.9f).w However, the use of the HG phase function has been shown to be sufficiently accurate for radiation transfer analysis through strongly forward scattering media such as microalgae suspensions containing gas bubbles [78], glass containing bubbles [120], red blood cells [121, 122], and also in the field of ocean optics [123, 124].

Note that microalgae cells are strongly forward scattering due to their large size compared with the wavelength of the photosynthetically active radiation (PAR). In addition, the solution of the radiative transfer equation derived by Pottier *et al.* [41] based on the two-flux approximation, has been shown to offer a relatively accurate method for predicting the fluence rate in open pond and flat-plate PBRs [41, 116]. Their analytical expression requires only the absorption and scattering cross-sections, the microorganism concentration, as well as the backward scattering ratio b of the microalgae suspension. The insets to Figures 3.9a to 3.9e show the values of b for each aggregates estimated using the scattering phase function predicted using (i) the T-matrix method, (ii) the coated sphere approximation, (iii) the RDG approximation, and (iv) the HG phase function. They indicate that the backward scattering ratio predicted using the coated sphere approximation was within 30% of that predicted by the T-matrix method for aggregates composed of monomers of size parameter $\chi_s = 1$. In addition, b was negligibly small for aggregates composed of monomers with $\chi_s = 5$.

Moreover, Berberoğlu *et al.* [78] used the discrete ordinates method with a combination

of two Gauss quadrature having 24 discrete directions per hemisphere to predict the fluence rate in PBRs containing microorganisms. Results obtained using the HG approximate phase function were in good agreement with those obtained using the phase function predicted by the Lorenz-Mie theory of the microorganism suspension. This demonstrates that for the purposes of unpolarized radiation transfer analysis through microalgae cultures, or any other strongly forward scattering media, knowledge of the integral radiation characteristics $\langle C_{abs}^a \rangle$, $\langle C_{sca}^a \rangle$, g, and b are sufficient.

Finally, the inset to Figures 3.9a to 3.9e show the scattering phase function $F_{11}(\Theta = 0^o)$ values obtained by (i) the T-matrix method, (ii) for the equivalent coated sphere, (iii) the RDG approximation, and (iv) the HG phase function. This is of particular interest since most of the scattered radiation energy is concentrated around the forward direction $\Theta = 0^o$ for large aggregates and/or large monomers. Relatively good agreement was found between the values of $F_{11}(0^o)$ predicted by the T-matrix approximation and those predicted for the equivalent coated spheres. In fact, the relative error between the predictions of the two methods was less than 13% for all size parameters χ_s and monomer numbers N_s considered. In addition, the value of $F_{11}(\Theta = 0^o)$ predicted by the HG approximation was accurate within 15% for aggregates composed of 36 or 100 monomers with size parameter $\chi_s = 1$. However, it overestimated $F_{11}(0^o)$ for aggregates composed of monomers with larger size parameter.
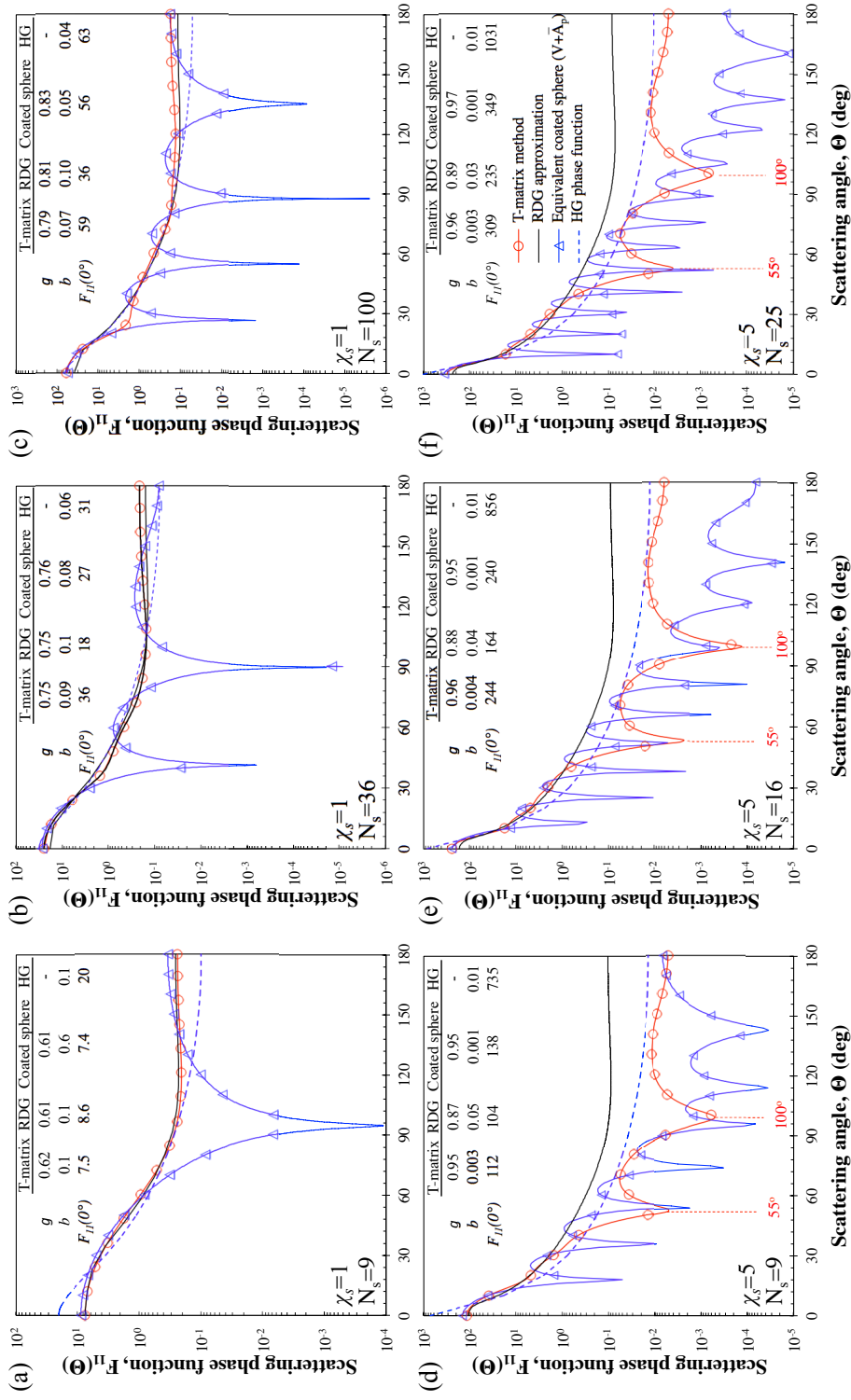
Figure 3.9: Scattering phase function $F_{11}(\Theta)$ of randomly oriented aggregates of fractal dimension D_f of 2.25 with monodisperse monomers of size parameters χ_s equal to (a-c) 1.0 or (d-f) 5, $m = 1.0165 + i0.003$ and N_s ranging from 9 to 100 estimated using the superposition T-matrix method, the RDG approximation, and for the volume and average projected area equivalent coated sphere, and the HG phase function. The inset table reports the corresponding asymmetry factor g computed using Equation (3.6).

71

3.4.4 Scattering matrix element ratios

Polarized incident radiation and the scattering matrix elements can be used in remote sensing applications to characterize the morphology of the aggregates defined by a, N_s, k_f, D_f, V_T, and/or $\bar{A}_p$. Figures 3.10 plots the normalized scattering matrix element ratios (a) $F_{21}(\Theta)/F_{11}(\Theta)$, (b) $F_{22}(\Theta)/F_{11}(\Theta)$, (c) $F_{33}(\Theta)/F_{11}(\Theta)$, (d) $F_{34}(\Theta)/F_{11}(\Theta)$, and (e) $F_{44}(\Theta)/F_{11}(\Theta)$ predicted by the superposition T-matrix method as functions of scattering angle Θ for randomly oriented aggregates of fractal dimension D_f=2.25 and consisting of 9, 36, and 100 monomers with size parameter χ_s=1 and $m = 1.0165 + i0.003$. They also show the same scattering matrix element ratios predicted for the volume and average projected area equivalent coated sphere. The degree of linear polarization of the aggregates $F_{21}(\Theta)/F_{11}(\Theta)$ was identical for all values of N_s considered. It reached 100% at scattering angle $\Theta = 90^o$ and was equal to 0% at scattering angles Θ of 0° and 180°. The scattering matrix element ratio $F_{22}(\Theta)/F_{11}(\Theta)$ was equal to 100% for all scattering angles Θ. The scattering matrix element ratios $F_{33}(\Theta)/F_{11}(\Theta)$ and $F_{44}(\Theta)/F_{11}(\Theta)$ were equal for all aggregates and decreased from 100% at $\Theta = 0^o$ to -100% at $\Theta = 180^o$. Finally, the scattering matrix element ratio $F_{34}(\Theta)/F_{11}(\Theta)$ was equal to zero for all angles Θ. Results for the different scattering matrix element ratios presented in Figure 3.10 for $\chi_s = 1$ were identical to those for a single sphere. This indicates the dominant role of single scattering by the constituent monomers [103, 125]. These results confirm the findings by Liu and Mishchenko [103] who demonstrated that increasing the aggregate number of monomers N_s up to 400, with size parameter $\chi_s = 0.2$, did not modify the scattering matrix element ratios.

The equivalent coated sphere featured scattering element ratios with overall trends similar to those predicted by the T-matrix method. However, they also featured resonance peaks at scattering angles Θ corresponding to those observed in the scattering phase function shown in Figures 3.9a to 3.9c and attributed to internal reflectance in the coating. These results indicate that the volume and average projected area equivalent coated sphere approximation cannot be used for predicting the scattering matrix elements of the actual aggregates. Thus, it will not be considered further in this section.
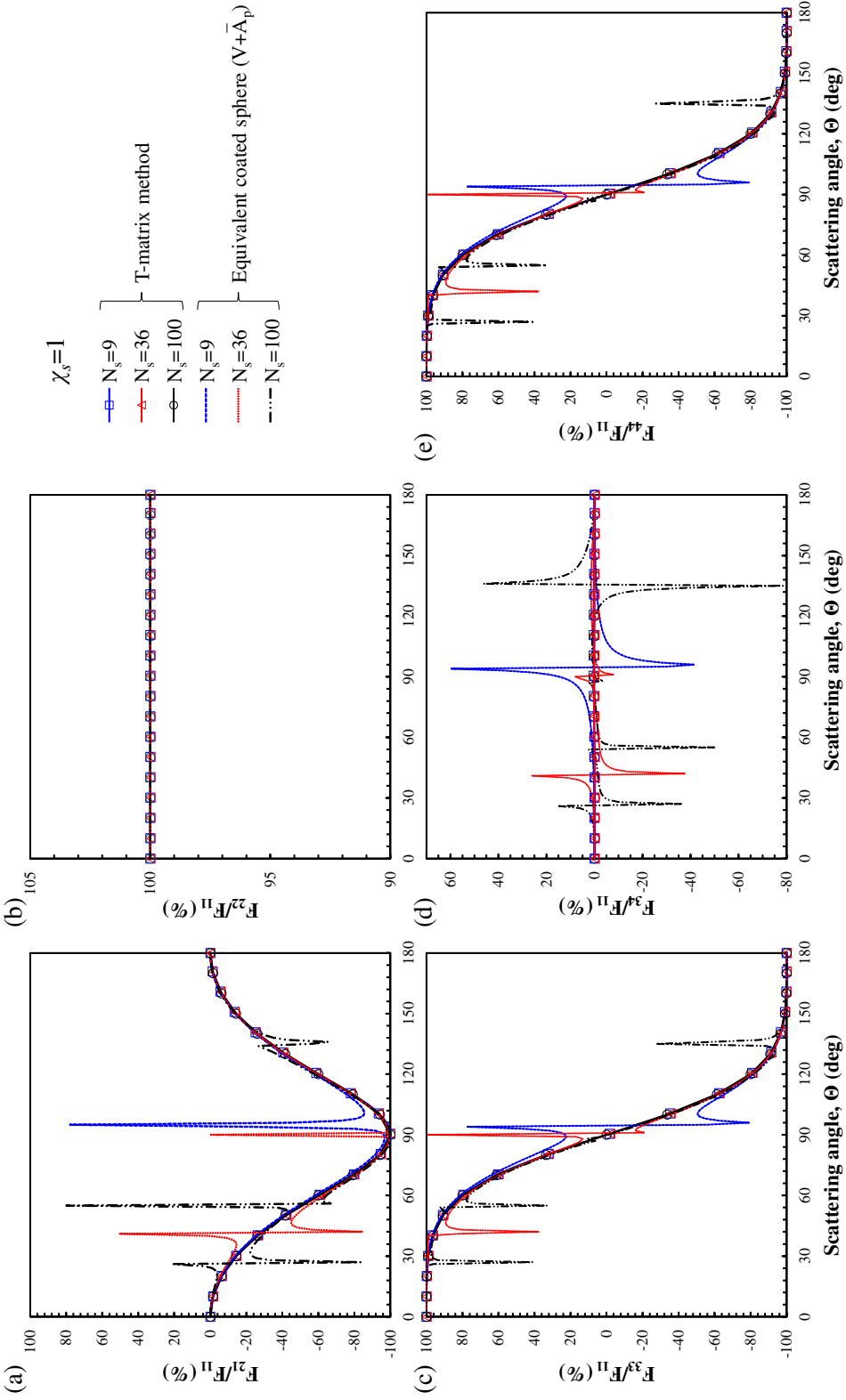
Figure 3.10: Scattering matrix element ratios (a) $F_{21}(\Theta)/F_{11}(\Theta)$, (b) $F_{22}(\Theta)/F_{11}(\Theta)$, (c) $F_{33}(\Theta)/F_{11}(\Theta)$, (d) $F_{34}(\Theta)/F_{11}(\Theta)$, and (e) $F_{44}(\Theta)/F_{11}(\Theta)$ of randomly oriented aggregates with fractal dimension $D_f = 2.25$ containing 9, 36, and 100 monodisperse monomers with size parameter $\chi_s = 1$ and relative complex index of refraction $m = 1.0165 + i0.003$ predicted using the superposition T-matrix method and the volume and average projected area equivalent coated sphere approximation.

Figures 3.11 shows the scattering matrix element ratios (a) $F_{21}(\Theta)/F_{11}(\Theta)$, (b) $F_{22}(\Theta)/F_{11}(\Theta)$, (c) $F_{33}(\Theta)/F_{11}(\Theta)$, (d) $F_{34}(\Theta)/F_{11}(\Theta)$, and (e) $F_{44}(\Theta)/F_{11}(\Theta)$ predicted by the superposition T-matrix method as a function of scattering angle Θ for randomly oriented aggregates of fractal dimension D_f of 2.25 and consisting of 9, 36, and 100 monomers of size parameter χ_s=5 and $m = 1.0165 + i0.003$. All scattering matrix element ratios featured resonance peaks at scattering angles Θ of 55° and 100° also observed in the aggregate scattering phase function $F_{11}(\Theta)$ (Figures 3.9d-3.9f). These resonance peaks appeared in the scattering matrix elements for large enough monomer size parameter. Similar resonance peaks were observed in the scattering matrix element ratios of aggregates composed of linear chain of spheres with size parameter of 10 [85] and for fractal soot aggregates with $D_f = 1.82$ and $k_f = 1.19$ composed of 200 monomers with size parameter $\chi_s = 0.6$ [103]. Here, the number and angles of the resonance peaks depended on the monomer size parameter χ_s while their magnitude depended on the number of monomers N_s in the aggregates. Indeed, the scattering matrix element ratios had 1, 2, or 6 resonance peaks for aggregates composed of $N_s = 9$ monomers with size parameter 2.5, 5, or 10, respectively (see Appendix A). These confirm and expand on previous results reported by Mackowski and Mishchenko [126] illustrating that the resonance angles of aggregates of up to 5 spherical monomers of size parameter $\chi_s = 5$ were equal to those for a single sphere of the same size parameter. The authors also reported that increasing monomer number in an aggregate causes "damping of the oscillation in the matrix elements" [126]. However, here no such effect could be observed (see Appendix A).

Furthermore, the ratio $F_{21}(\Theta)/F_{11}(\Theta)$ deviated from unity while the scattering element ratios $F_{33}(\Theta)/F_{11}(\Theta)$ and $F_{44}(\Theta)/F_{11}(\Theta)$ featured similar trends but were not identical. Divergence of the ratio F_{22}/F_{11} from unity as well as the inequality between the ratios F_{33}/F_{11} and F_{44}/F_{11} were also observed by Mishchenko *et al.* [127] and used as indicators for nonsphericity of randomly oriented bispheres of size parameter $\chi_s = 5$ and relative index of refraction $m = 1.5 + 0.005$. Such features of the scattering matrix elements can be used for remote sensing applications.
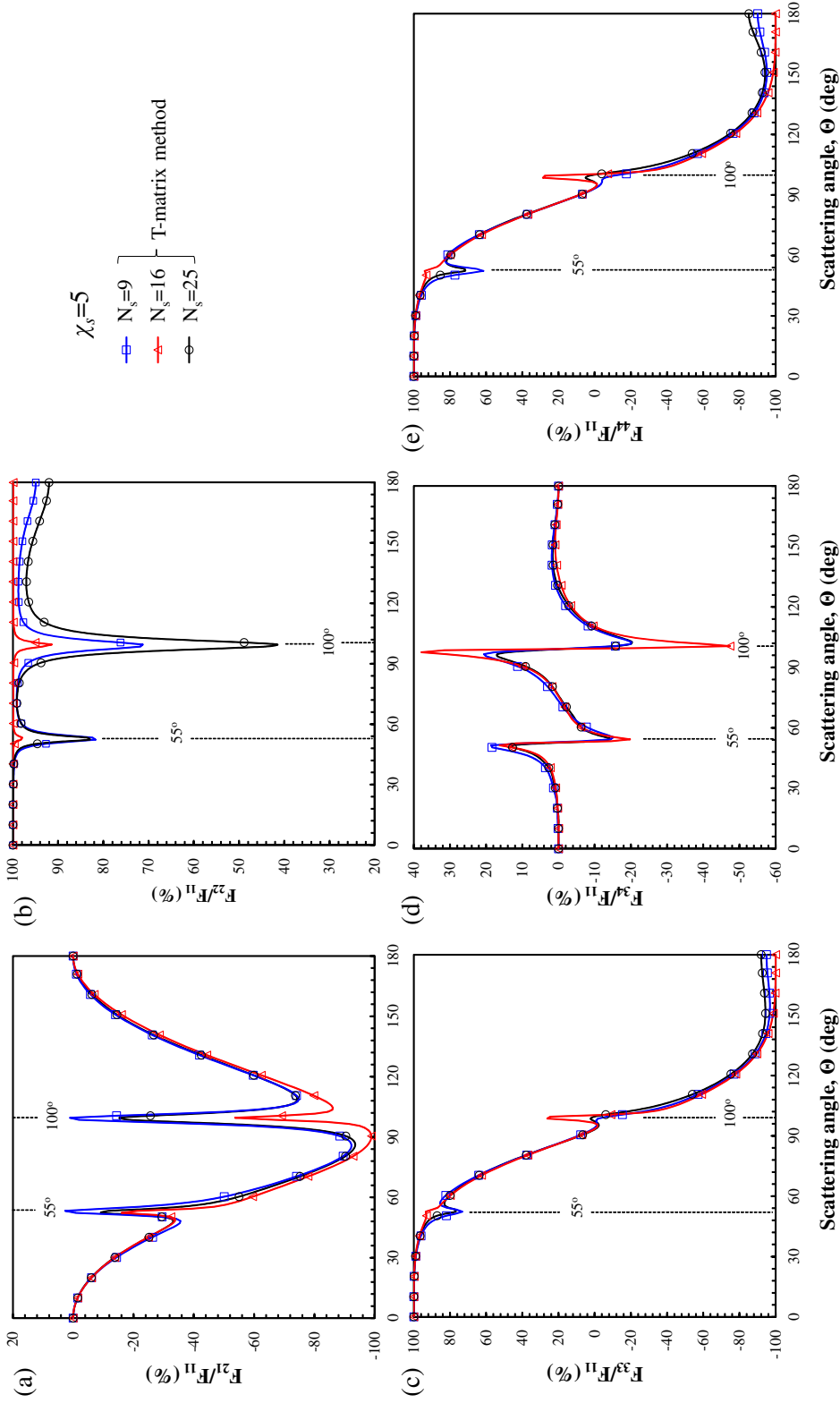
Figure 3.11: Scattering matrix element ratios (a) $F_{21}(\Theta)/F_{11}(\Theta)$, (b) $F_{22}(\Theta)/F_{11}(\Theta)$, (c) $F_{33}(\Theta)/F_{11}(\Theta)$, (d) $F_{34}(\Theta)/F_{11}(\Theta)$, and (d) $F_{44}(\Theta)/F_{11}(\Theta)$ of randomly oriented aggregates with fractal dimension $D_f = 2.25$ containing 9, 16, and 25 monodisperse monomers with size parameter $\chi_s = 5$ and $m = 1.0165 + i0.003$ predicted using the superposition T-matrix method.

3.4.5 Retrieved relative complex index of refraction

Table 3.2 shows the relative complex index of refraction used in predicting the absorption and scattering cross-sections of randomly oriented aggregates using the T-matrix method as well as those retrieved by the inverse method. Each suspension featured aggregates with monomer number distribution $p(N_s)$ (FIgures 3.2a and 3.2b). The aggregates featured a fractal dimension of 2.25 and were composed of monodisperse monomers of size parameter χ_s of 0.01, 0.1, 0.5, 1, 5, or 10. The monomer relative refraction index n was equal to 1.0165 and the relative absorption index k was taken as 0.003, 0.03, 0.07, or 0.5.

Table 3.2: The input and retrieved relative complex index of refraction of aggregates of fractal dimension D_f of 2.25, and size parameter 0.01, 0.1, 0.5, 1, 5, or 10.

	T-matrix				Retrieved			
χ_s	n	k	$\langle C^a_{abs} \rangle_T$ $(\mu\mathrm{m}^2)$	$\langle C^a_{sca} \rangle_T$ $(\mu\mathrm{m}^2)$	n	error (%)	k	error (%)
0.01	1.0165	0.003	6.4×10^{-3}	1.2×10^{-8}	1.0173	0.1	0.003	0
0.1	1.0165	0.003	6.5×10^{-2}	8.82×10^{-5}	1.0165	0	0.0029	4.3
0.5	1.0165	0.003	0.33	1.2×10^{-2}	1.0178	0.1	0.003	0.7
1	1.0165	0.003	0.66	7.1×10^{-2}	1.0176	0.1	0.003	1.3
1	1.0165	0.03	6.17	0.27	1.0234	0.7	0.029	4.3
1	1.0165	0.07	13.2	1.07	1.0383	2.2	0.065	6.9
1	1.0165	0.5	48.0	19.8	1.0005	1.6	0.474	5.2
5	1.0165	0.003	0.88	0.43	1.0166	0.01	0.0032	6.7
10	1.0165	0.003	1.7	1.71	1.0162	0.03	0.003	0.7

The relative difference between the input and the retrieved refraction and absorption indices was less than 7% for all cases considered. The error was significantly smaller for aggregates composed of monomers with small absorption index. On the other hand, the relative error in the retrieved complex index of refraction did not show any obvious trend with monomer size parameter. This demonstrates the capability of this inverse method to

retrieve the relative complex index of refraction of fractal aggregates based on the volume and average projected surface area coated sphere approximation and their total absorption $\langle C_{abs}^a \rangle_T$ and scattering $\langle C_{sca}^a \rangle_T$ cross-sections predicted by the T-matrix method. It also demonstrates that the method can be applied to aggregates composed of monomers with a wide variety of absorption indices and size parameters. Thus, it could be applied to accurately estimate the optical properties of microalgae aggregates and colonies in the oceans, ponds, and photobioreactors.

3.5 Conclusion

This study demonstrated that the absorption $\langle C_{abs}^a \rangle$ and scattering $\langle C_{sca}^a \rangle$ cross-sections and the asymmetry factor g of randomly oriented fractal aggregates consisting of spherical monomers can be rapidly estimated as those of coated spheres with equivalent volume and average projected area. Predictions for $\langle C_{abs}^a \rangle$ and $\langle C_{sca}^a \rangle$, and g fell within 8%, 29%, and 15%, respectively, for aggregates composed of monomers with (i) size parameter χ_s between 0.01 and 20, (ii) number N_s ranging from 1 to 1000, (iii) relative refractive index of 1.0165 and absorption index varying from 0.003 to 0.5, and (iv) for aggregates of fractal dimension ranging from 2.0 to 3.0. First, a convenient correlation was derived for the average projected area of fractal aggregates with various fractal dimensions. The proposed equivalent coated sphere approximation was able to capture multiple scattering in the aggregates and shading among constituent monomers on the integral radiation characteristics of the aggregate. It was superior to that proposed by Latimer [107] and to the Rayleigh-Debye-Gans approximation, particularly for large values of χ_s and N_s. In addition, the use of Henyey-Greenstein approximate phase function estimated using the asymmetry factor for the equivalent coated sphere yielded acceptable predictions of the actual aggregate scattering phase function for all values of χ_s and N_s considered. However, the equivalent coated spheres featured scattering matrix element ratios significantly different from those of the aggregates due to internal reflection in the coating. The scattering phase function and the scattering matrix elements were found to have unique features for large monomer size parameter χ_s. These could be

used in remote sensing applications to measure the morphology of such aggregates. Finally, the proposed inverse method could be applied to accurately estimate the optical properties of microalgae aggregates and colonies in the oceans, ponds, and photobioreactors.

CHAPTER 4

Control of Incident Irradiance on a Batch Operated Flat-Plate Photobioreactor

This chapter presents an experimental demonstration of a novel feed-forward inversion control scheme for maintaining an optimum incident irradiance on photobioreactors (PBRs) during batch cultivation. It uses the radiation characteristics of *N. oculata* measured in Chapter 2 for the radiation transfer analysis and incident irradiance control. The goal of this chapter is to develop an experimental approach able to (i) identify rapidly the optimum average fluence rate for any species, (ii) reduce the lag time, and (iii) increase the growth rate and biomass productivity of microalgae.

4.1   Introduction

Microalgae can be produced in large quantities in photobioreactors (PBRs) operated in batch or continuous mode. Batch cultivation is more widely used due to its simplicity and low cost [128]. Optimization of the light available to microorganisms in PBRs is a crucial aspect of biomass production and process productivity [4, 8, 9, 39, 74]. Light is the energy source that enables these photosynthetic microorganisms to metabolize. Inadequate amount of light causes a decrease in growth and photosynthesis rates due to lack of energy necessary to fixate carbon. Similarly, exposing microalgae to excessively large irradiances causes photo-oxidative damage in photosystem II units. The cells continuously perform a damage repair cycle to repair the damaged photosystem II units [27, 28]. However, when the damage rate exceeds the repair rate, photoinhibition becomes apparent and the overall cell photosynthetic efficiency decreases [10, 27]. Identifying the optimum level of irradiance

required for maximum microalgae growth rate and maintaining an optimum fluence rate in the PBR throughout the growth phase are necessary to increase biomass productivity.

This study aims to develop a versatile and robust scheme to control the incident irradiance on PBRs for maximizing microalgae growth rate and biomass productivity. The method should be able to rapidly identify the optimum light conditions. It should also be applicable to any species and/or PBR without prior knowledge of the culture growth kinetics.

4.2 Background

4.2.1 Radiative transfer model

Several methods of solution for the RTE exist [8, 116, 129, 130]. Pottier *et al.* [41] derived an analytical solution to the one-dimensional RTE using the Schuster-Schwarzschild two-flux approximation in order to model light transfer through a well-mixed algal cultures in vertical flat-plate PBRs. The local spectral fluence rate $G_\lambda(z)$ in such PBRs with (i) normally incident light at $z = 0$ and (ii) perfectly transmitting back wall at $z = L$ was given by Pottier *et al.* [41] as

$$\frac{G_\lambda(z)}{G_{in,\lambda}} = 2\frac{(1+\alpha_\lambda)e^{\delta_\lambda X(L-z)} - (1-\alpha_\lambda)e^{-\delta_\lambda X(L-z)}}{(1+\alpha_\lambda)^2 e^{\delta_\lambda XL} - (1-\alpha_\lambda)^2 e^{-\delta_\lambda XL}} \tag{4.1}$$

where $G_{in,\lambda}$ is the spectral irradiance incident on the surface of the PBR. Here, X is the dry mass concentration of microalgae (in kg/m^3) and L is the PBR thickness (in m). The coefficients α_λ and δ_λ are expressed as [41]

$$\alpha_\lambda = \sqrt{\frac{\bar{A}_{abs,\lambda}}{\bar{A}_{abs,\lambda} + 2b_\lambda \bar{S}_{sca,\lambda}}} \quad \text{and} \quad \delta_\lambda = \sqrt{\bar{A}_{abs,\lambda}\left(\bar{A}_{abs,\lambda} + 2b_\lambda \bar{S}_{sca,\lambda}\right)} \tag{4.2}$$

where $\bar{A}_{abs,\lambda}$ and $\bar{S}_{sca,\lambda}$ (in m^2/kg) are the average mass absorption and scattering cross-sections of the microalgae suspension, respectively. They are related to the absorption and scattering coefficients by [8]

$$\kappa_\lambda = \bar{A}_{abs,\lambda}X \quad \text{and} \quad \sigma_{s,\lambda} = \bar{S}_{sca,\lambda}X \tag{4.3}$$

In addition, b_λ is the backward scattering fraction defined, for axisymmetric scattering, as [41, 131]

$$b_\lambda = \frac{1}{2} \int_{\pi/2}^{\pi} \Phi_\lambda(\theta) \sin\theta \mathrm{d}\theta \tag{4.4}$$

where θ is the scattering angle between directions $\hat{s}_i$ and $\hat{s}$.

Similarly, the volume-averaged fluence rate G_{ave} in a one-dimensional PBR of thickness L over the PAR region can be estimated from the local spectral fluence rate as [19, 132]

$$G_{ave} = \frac{1}{L} \int_0^L G_{PAR}(z) \mathrm{d}z \tag{4.5}$$

4.2.2 Growth model

The time rate of change of the microorganism mass concentration $X(t)$ can be predicted by the exponential growth equation

$$\frac{dX}{dt} = \mu X \tag{4.6}$$

where μ is the specific growth rate expressed in hr^{-1}. Despite the presence of fluence rate gradient in the PBR, growth kinetics models often use the average fluence rate G_{ave} [19, 128, 132, 133]. This approach is valid for optically thin PBRs where the fluence rate does not significantly vary within the PBR [116, 130, 134]. A more general approach is to relate the growth rate $\mu(z)$ to the local fluence rate $G_{PAR}(z)$ and average it over the volume of the PBR [73, 75, 116, 135].

Finally, the daily volumetric productivity P_v (in kg/m^3·day) and the daily areal productivity P_A (in kg/m^2·day) of a PBR, defined as the average biomass produced daily per unit volume and per unit surface area of PBR exposed to the light source, can be defined as

$$P_v = \frac{X_f - X_0}{\tau} \quad \text{and} \quad P_A = P_v \frac{L}{2} \tag{4.7}$$

where τ (in days) is the duration needed to reach the saturation mass concentration X_f from an initial mass concentration X_0.

4.2.3 Optimum *Nannochloropsis oculata* cultivation conditions

Various studies have aimed at finding the optimum operating conditions for growing *N. oculata* In closed PBRs in batch mode. For example, Chiu *et al.* [136] grew *N. oculata* in modified f/2 medium in batch mode in a vertical tubular PBR 7 cm in diameter exposed to 300 $\mu mol_{h\nu}/m^2 \cdot s$ fluorescent light. The PBR was sparged with air or with 2 vol.% CO_2 in air mixture and the biomass concentration reached a maximum of 0.26 kg/m^3 and 1.28 kg/m^3, respectively. In addition, *N. oculata* cultures aerated with CO_2 concentrations larger than 5 vol.% did not show any significant growth [136]. Spolaore *et al.* [137] estimated the optimum conditions based on response surface optimization method for *N. oculata* grown in batch mode in a 2.5 L bubble column PBR with f/2 medium. These conditions were 21°C, pH of 8.4, and incident irradiance of 52 $\mu mol_{h\nu}/m^2 \cdot s$ resulting in a maximum value of specific growth rate μ of 0.036 h^{-1}. Converti *et al.* [138] reported a maximum specific growth rate μ of 0.005 h^{-1} for *N. oculata* cultivated in f/2 medium in 2 L flasks injected with 0.03 vol.% CO_2/air mixture exposed to incident irradiance of 70 $\mu mol_{h\nu}/m^2 \cdot s$ at 20°C. These studies demonstrate that for a given microalgae species and strain, PBR geometry, temperature, nutrient availability, and spectral light quality determine the optimum average fluence rate. The latter must be experimentally identified in order to maintain optimum conditions in the PBR and maximize its productivity.

4.2.4 Microalgae cultivation techniques

Light is one of the main limiting factors of microalgae cultivation and growth kinetics models are often used to predict the optimal operating conditions for maximum biomass or lipid productivity [73, 75, 139]. In fact, optimum cultivation conditions depend on microalgae species, strain, growth media, and PBR geometry [17, 132, 133, 140]. These conditions are unique for each cultivation system and can only be reliably obtained experimentally. Accurate estimation of the optimum average fluence rate is essential for optimizing PBR productivity.

Furthermore, the average fluence rate in the PBR decreases as the microalgae mass con-

centration increases. Therefore, to maintain a constant average fluence rate in the PBR throughout the duration of the cultivation, one must keep the cell concentration constant by diluting the culture (continuous mode) or by increasing the incident irradiance over time (batch mode). Several cultivation techniques such as the acceleration-stat and the lumostat have been developed to address this problem. For example, the aim of the acceleration-stat cultivation is to maintain a pseudo steady-state in the PBR by controlling the biomass concentration. Barbosa *et al.* [140] cultivated *Dunaliella tertiolecta* in a 65 L bubble column PBR in continuous mode with a variable dilution rate. This method was successful at maintaining a relatively constant microalgae growth rate and PBR productivity for 500 h. Similarly, Cuaresma *et al.* [141] designed a system that changed the concentration of *C. sorokiniana* in real time in a flat-plate PBR to maintain a predetermined optimal optical transmittance. The authors simulated diurnal light conditions using a LED panel to demonstrate the feasibility of such strategy.

On the other hand, the lumostat cultivation technique relies on direct adjustment of the incident irradiance to maintain a constant growth rate and productivity in a batch cultivation [128, 141, 142]. Chen *et al.* [128] measured microalgae concentration every six hours and adjusted the incident irradiance according to an empirical correlation relating the cell number density and the optimum incident irradiance. The latter was determined by first performing a series of batch cultivation experiments using *Chlorella* sp. in draft-tube PBR. The authors hypothesized that batch culture's optimum average fluence rate corresponded to its maximum chl$a$ concentration. After 300 hours, the PBR operated with a controlled irradiance achieved a biomass concentration 25 and 74 % larger than those using constant irradiances of 82 and 590 μmol$_{h\nu}$/m^2·s, respectively.

Similarly, Melnicki *et al.* [142] grew the cyanobacteria *Cyanothece* sp. and *Synthecoccus* sp. in a 7.5 L cylindrical PBR with an inner diameter of 13.4 cm illuminated by variable intensity LEDs at wavelengths 630 and 680 nm. The PBR was equipped with light transmission sensors and could be utilized as both an acceleration-stat or a lumostat. The authors demonstrated the system's ability to maintain a pre-determined optical transmit-

tance through the culture by feedback-control of the LED light source. The feedback control scheme was very similar to the system developed by Cuaresma *et al.* [141]. Note that such system is very cost prohibitive due to the necessity to custom construct a PBR to accommodate the various sensors and actuators of the control system. It is not widely available in practice.

The main shortcoming of previous studies lies in the fact that they required extensive and time consuming experiments in order to identify the optimum average fluence rate. For example, Chen *et al.* [128] performed 4 batch cultivation experiments collecting in excess of 300 data points. In addition, previous studies relied on indirect method of identifying the optimum average fluence rate [128]. For example, a batch culture's optimum average fluence rate generally does not correspond to its maximum chl*a* concentration [39, 114, 115]. Moreover, the system presented by Melnicki *et al.* [142] did not feature a method for estimating the optimum average fluence rate and was very cost prohibitive.

The present study aims to develop a novel, low-cost, robust, and model-free method to estimate the optimum average fluence rate in the PBR and use feed-forward inversion control to continuously adjust the incident irradiance on the PBR operated in batch mode. Marine microalgae *N. oculata* were used to experimentally demonstrate the approach. The biomass concentration, growth rate, and productivity of the microalgae grown under controlled irradiance were compared with those grown using constant incident irradiance.

4.3 Experiments

4.3.1 Materials and methods

The microalgae species *N. oculata* UTEX 2164 were purchased from UTEX, Austin, TX. They were cultivated in artificial seawater medium. The latter had the following composition: NaCl 0.31M, $MgSO_4 \cdot 7H_2O$ 10.5 mM, KCl 8 mM, $NaNO_3$ 11.8 mM, $CaCl_2 \cdot 2H_2O$ 2 mM, KH_2PO_4 0.37 mM, NH_4Cl 0.5 mM, $Na_2EDTA \cdot 2H_2O$ 0.27 mM, H3BO3 1.84 mM, $FeCl_3 \cdot 6H_2O$ 0.018 mM, $MnSO_4 \cdot H_2O$ 0.097 mM, $ZnSO_4 \cdot 7H_2O$ 0.007 mM, $CoCl_2 \cdot 6H_2O$ 0.002 mM, Vitamin

B12 0.1 μM.

(a)

(b)

(c)

(d)
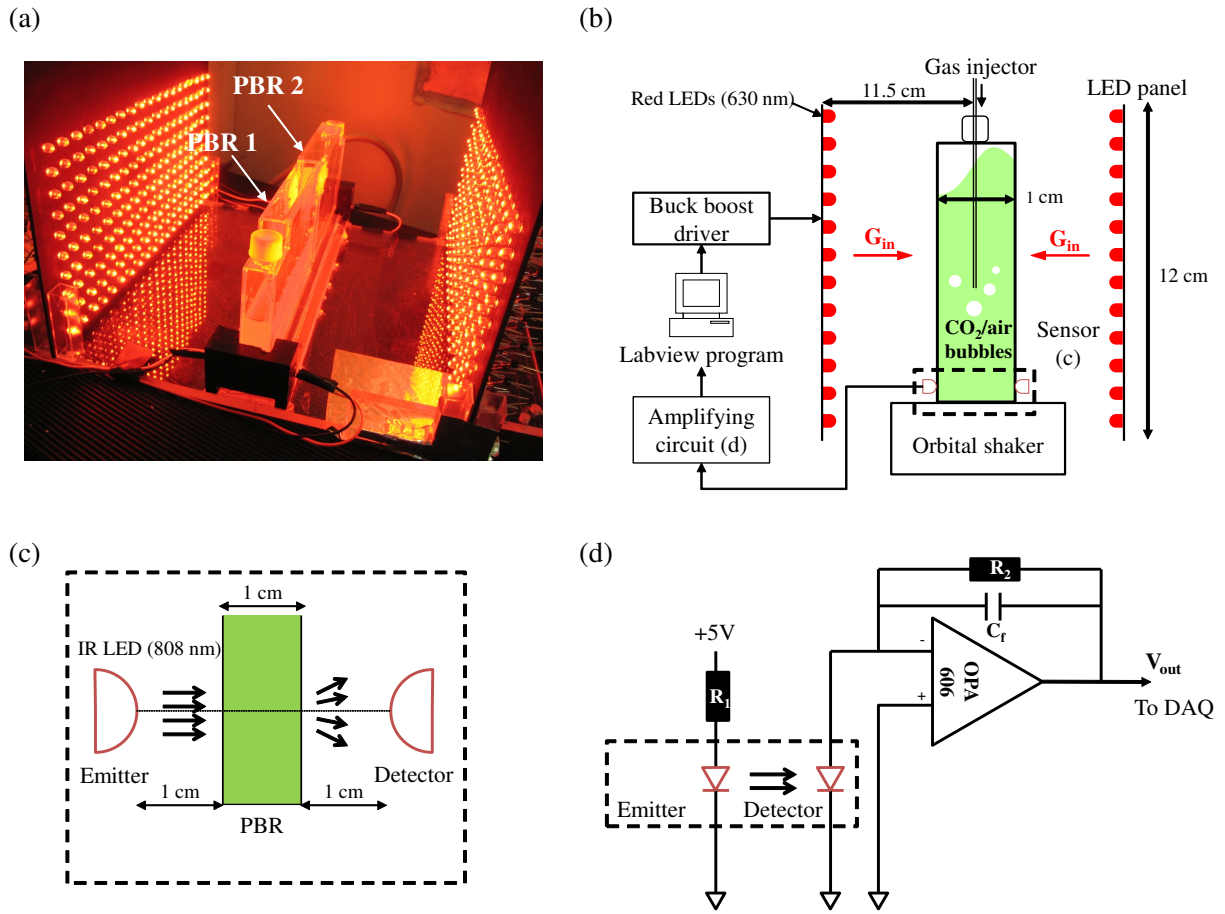
Figure 4.1: (a) Photograph and (b) schematic of the experimental setup used in the study. (c) Mass concentration sensor with IR LED emitter and detector at 808 nm, and (d) electronic circuit used to amplify the photocurrent from the IR diode.

Figures 4.1a and 4.1b show a photograph and the schematic of the experimental apparatus, respectively. It consisted of (i) a flat-plate PBR operated in batch mode, (ii) two custom made LED panels, (iii) a custom concentration sensor, and (iv) a controller. Measurements were performed in duplicates in identical PBR 1 and PBR 2 placed immediately adjacent to each other and operated simultaneously. Each PBR was a 1 cm thick flat-plate container made of acrylic filled with 70 ml of artificial seawater medium. It was continuously aerated with a mixture of air and CO_2 injected at a rate of 7.5 ml/min via a needle through a septum

85

cap. The microalgae were kept in suspension using an orbital shaker rotating at 100 rpm. The pH was measured daily with a ±0.01 accuracy electrode (PHB-213 Omega Engineering, CT) and maintained between 7.7 and 8.0 by adjusting the CO_2 flow rate once a day as necessary. The temperature was approximately 22°C for all experiments. Finally, all experiments started with an initial mass concentration X_0 of 0.02 kg/m^3. The LED panel consisted of 390 discrete low-power red LEDs (C503B-RAN Cree, NC) with peak emission at 630 nm and 30 nm spectral bandwidth. These LEDs were as effective in growing $N.$ $oculata$ as white fluorescent light [114]. They were spaced 2.25 cm apart resulting in a spatial variation of less than 10% in the irradiance incident on the PBR located 11.5 cm from the LED panels. A buck-boost LED controller (LUXdrive by LEDdynamics, VT) was used to vary the intensity of the LED panels. The incident irradiance of the LED panels was adjusted by an analog voltage input to the LED controller. Figure 4.1c shows a schematic of the concentration sensor assembly consisting of an infrared (IR) LED (OSRAM SFH4550, Osram-Sylvania, MA) emitting at 808 nm with a beam divergence angle of 6°. A second identical diode was place on the other side of the PBR to sense the IR beam attenuation through the PBR. Figure 4.1d shows the electrical circuit and the operational amplifier (Op-Amp) (OPA606KP Texas Instruments, TX) used to amplify the photocurrent from the detector diode. The output voltage V_{out} was sent to the data acquisition system (USB-1208FS Measurement Computing Co., MA) to measure the dry mass microalgae concentration based on a calibration curve relating V_{out} to X.

The controller input voltage V_{ctrl} to the LED panel and the incident irradiance were calibrated using a LICOR LI-190 quantum sensor. Figure 4.2a shows the calibration of the incident irradiance G_{in} (expressed in $\mu mol_{h\nu}/m^2 \cdot s$) as a function of V_{ctrl}. The incident irradiance from each panel varied between 0 and 440 $\mu mol_{h\nu}/m^2 \cdot s$. The microalgae dry mass concentration X was determined using a calibration curve relating X to the optical density (OD$_\lambda$) of the microalgae suspension at 750 nm. Note that at 750 nm, $N.$ $oculata$ do not absorb and only scatter [114]. The calibration curve was obtained by relating the normal-normal transmittance T_λ and the corresponding optical density OD$_\lambda = -lnT_\lambda$ at 750 nm
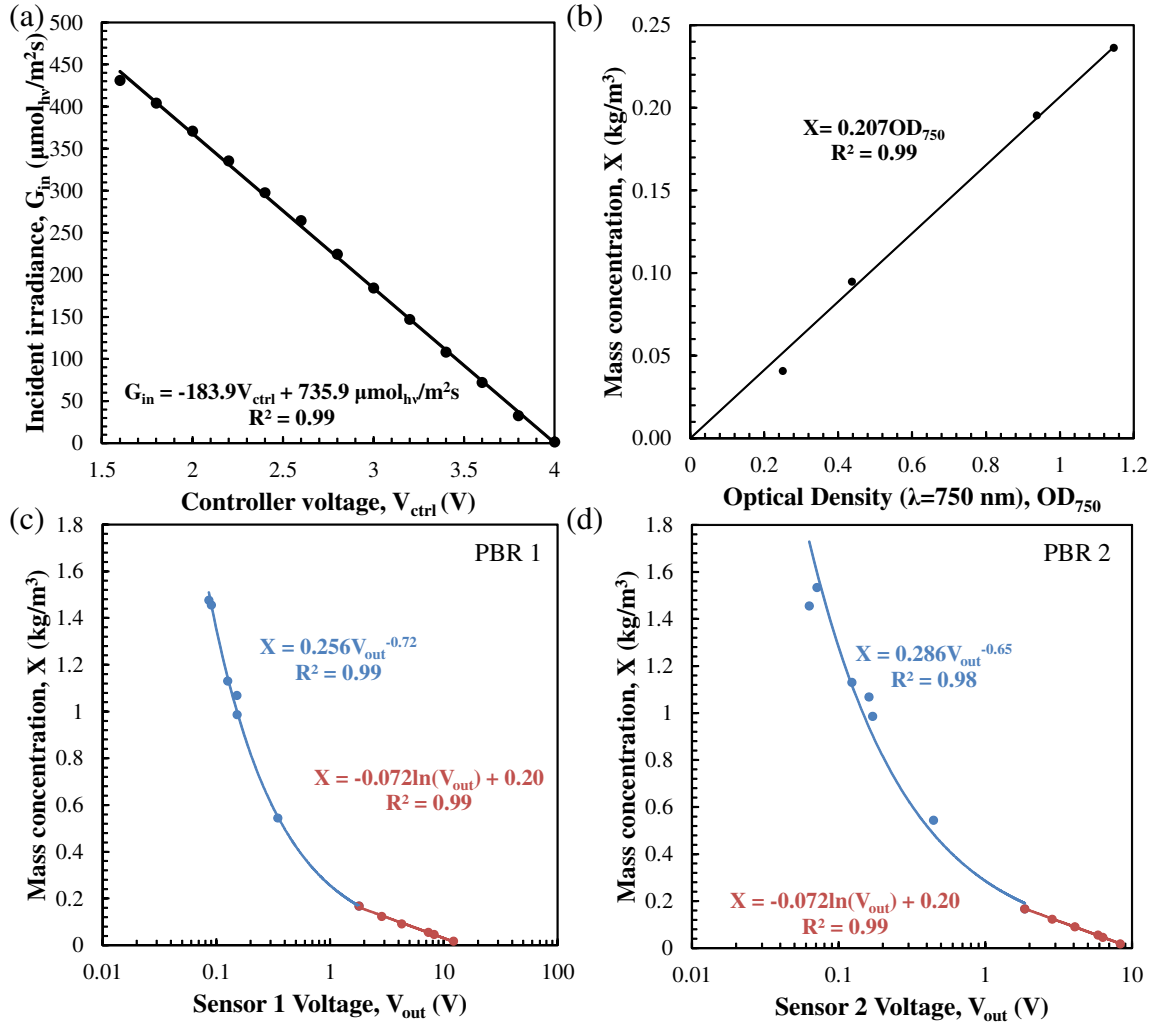
Figure 4.2: Calibration curves for (a) the incident irradiance G_{in} of the LED panel as a function of LED driver control voltage V_{ctrl}, and for *N. oculata* mass concentration $X(t)$ versus (b) the optical density at 750 nm OD_{750}, and sensor voltage V_{out} for (c) PBR 1 and (d) PBR 2.

for several mass concentrations of microalgae in disposable polystyrene cuvettes with 1 cm pathlength using a Fourier Transform Infrared spectrophotometer (FTIR) (ThermoNicolet Magna IR-560). The corresponding dry mass concentration X was measured by filtering the cells through a previously washed and dried 0.45 nm pore size cellulose membrane filters (HAWP-04700 by Millipore, MA) followed by drying at $60^{o}C$ in a vacuum oven overnight.

The dried filters with the dry cells were weighed immediately after being removed from the oven using a precision balance (model AT261 by Delta Range Factory, OH) with a 0.01 mg precision. Figure 4.2b shows the calibration curve relating optical density at 750 nm OD_{750} and mass concentration X. The resulting calibration curve was $X=0.207OD_{750}$.

Figures 4.2c and 4.2d show the calibration curves relating the output from the Op-Amp V_{out} and the microalgae concentration X for PBR 1 and PBR 2 sensors, respectively. The output voltage V_{out} was fitted to a natural logarithm function at low mass concentrations and to a power law for large concentrations. Good fits were obtained with a coefficient of determination R^2 larger than 0.99 for dry mass concentration X in the range 0.01 to 1.5 kg/m^3. Each sensor for PBR 1 and PBR 2 was calibrated individually to ensure better accuracy and reliability of the results. The two calibration curves for PBR 1 sensor formed a continuous function while those for PBR 2 featured slight offset at X=0.3 kg/m^3. Finally, for dry mass concentration exceeding 1.5 kg/m^3, 0.250 ml of microalgae culture was physically sampled from each PBR and diluted by adding 2.750 ml of medium to a 1 cm pathlength polystyrene cuvette before measuring the optical density OD_{750}.

4.3.2   Analysis

4.3.2.1   Light transfer model

The two-flux approximation of the RTE, given by Equation (4.1), can be further simplified in the case of strongly forward scattering microalgae when b_λ approaches 0 resulting in α_λ reaching unity. Then, the local fluence rate, for the PBR shown in Figure 4.1 with irradiation incident on both sides can be expressed as

$$G_\lambda(z) = G_{in,\lambda} \left[e^{-\delta_\lambda X z} + e^{-\delta_\lambda X (L-z)} \right] \tag{4.8}$$

This expression is similar to Beer-Lambert's law [37]. However, the arguments in the exponential functions are significantly different. In fact, Beer-Lambert's law is not appropriate for predicting the local fluence rate in a PBR due to strong forward and multiple scattering by microalgae [78].

The total irradiance G_{in} incident on one side of the PBR over the PAR (in W/m^2) can be written as

$$G_{in} = \int_{400}^{700} G_{in,\lambda} d\lambda = G_{in,\lambda_m} \int_{400}^{700} N_\lambda d\lambda \qquad (4.9)$$

where G_{in,λ_m} is the maximum spectral incident irradiance at wavelength λ_m between 400 and 750 nm and N_λ is the normalized spectral distribution of the incident irradiance. Here, λ_m was 630 nm for the LED light source used. Combining Equations (4.5) and (4.8), the total irradiance G_{in} on each side of the PBR to achieve a desired average fluence rate G_{ave} in the PBR with microorganism concentration X can be written as

$$G_{in} = G_{ave} \frac{\displaystyle\int_{400}^{700} N_\lambda d\lambda}{\displaystyle 2\int_{400}^{700} \frac{N_\lambda}{\delta_\lambda X L} \left(1 - e^{-\delta_\lambda X L}\right) d\lambda} = \frac{G_{ave}}{f(X)} \qquad (4.10)$$

where $f(X)$ is, for all practical purposes, a function of $X(t)$, for a given PBR description and a light source. Note that the factor 2 present in the denominator of Equation (4.10) was due to the fact that irradiance was incident on both sides of the PBR. Furthermore, in the asymptotic limits of $\delta_\lambda X L << 1$ and $\delta_\lambda X L >> 1$, $1/f(X)$ can be simplified as

$$\frac{1}{f(X)} = \begin{cases} \dfrac{1}{2} & \text{for} \quad \delta_\lambda X L << 1 \\[2ex] \dfrac{qXL}{2} & \text{for} \quad \delta_\lambda X L >> 1 \end{cases} \qquad (4.11)$$

where q is a constant defined as $q = \int_{400}^{700} N_\lambda d\lambda \Big/ \int_{400}^{700} (N_\lambda/\delta_\lambda) d\lambda$. Finally, the average absorption and scattering cross-sections $\bar{A}_{abs,\lambda}$ and $\bar{S}_{sca,\lambda}$ of *N. oculata*, needed to compute δ_λ, were reported by Kandilian *et al.* [114] between 400 and 700 nm with 1 nm spectral resolution. In addition, the scattering phase function was measured at $\lambda = 632.8$ nm and was shown to be nearly constant over the PAR region. The backward scattering coefficient b_λ was 0.002 according to Equation (4.4). Note that for $\delta_\lambda X L << 1$, Equation (4.10) can be approximated as $G_{in} \approx \frac{1}{2} G_{ave}$. On the other hand, for $\delta_\lambda X L >> 1$, the feed-forward gain $1/f(X)$ is bounded since XL is bounded.

4.3.2.2 Control scheme

Figures 4.3a and 4.3b show the proposed feed-forward inversion and optimal search diagrams, respectively. The controller consisted of the radiation transfer model [Equation (4.10)] and a zero-order-hold which operated at time interval Δt_1 equals to 5 minutes. The controller was fed the optimum average fluence rate G_{peak} and the measured mass concentration of the microalgae $X(t)$. Then, it generated the optimum incident irradiance $G_{in}(k\Delta t_1)$ necessary to achieve G_{peak} where $k\Delta t_1$ corresponded to k^{th} mass concentration sampling time. Similarly, the plant model, corresponding to the PBR, consisted of the radiation transfer model [Equation (4.10)], the microalgae growth kinetics model relating the average fluence rate G_{ave} to the growth rate μ and the microalgae growth equation [Equation (4.6)]. Note that experimentally, the mass concentration $X(t)$ was the only plant output parameter measured for the control system. The feed-forward controller is bounded-input-bounded-output stable since the feed-forward gain $1/f(X)$ is bounded, as previously discussed. One of the benefits of using such feed-forward control in microalgae cultivation lies in the fact that it does not suffer from instabilities. However, it requires accurate modeling of the system being controlled [143]. Moreover, the optimum average fluence rate in the PBR G_{peak} must be estimated before the beginning of the feed-forward control. It corresponded to G_{ave} that yielded the largest microalgae growth rate μ. To estimate G_{peak}, an optimal search procedure was devised to empirically correlate the average fluence rate in the PBR G_{ave} to the microorganism growth rate μ. Brent's method is an inverse parabolic interpolation method that estimates the abscissa corresponding to the maximum of a function [144]. In the optimal search diagram (Figure 4.3b), the radiation transfer model [Equation (4.10)] in the feed-forward controller (Figure 4.3a) inverted the radiation transfer model in the plant [Equation (4.10)] allowing the omission of both and facilitating the simple search method. The optimal search scheme required the input of several test values of average fluence rate G_{ave}^{*} to determine the optimum average fluence rate G_{peak} using Brent's method. The latter enabled the estimation of G_{peak} without requiring a model relating incident irradiance to growth rate. The only assumption made was that the growth rate μ was a convex function
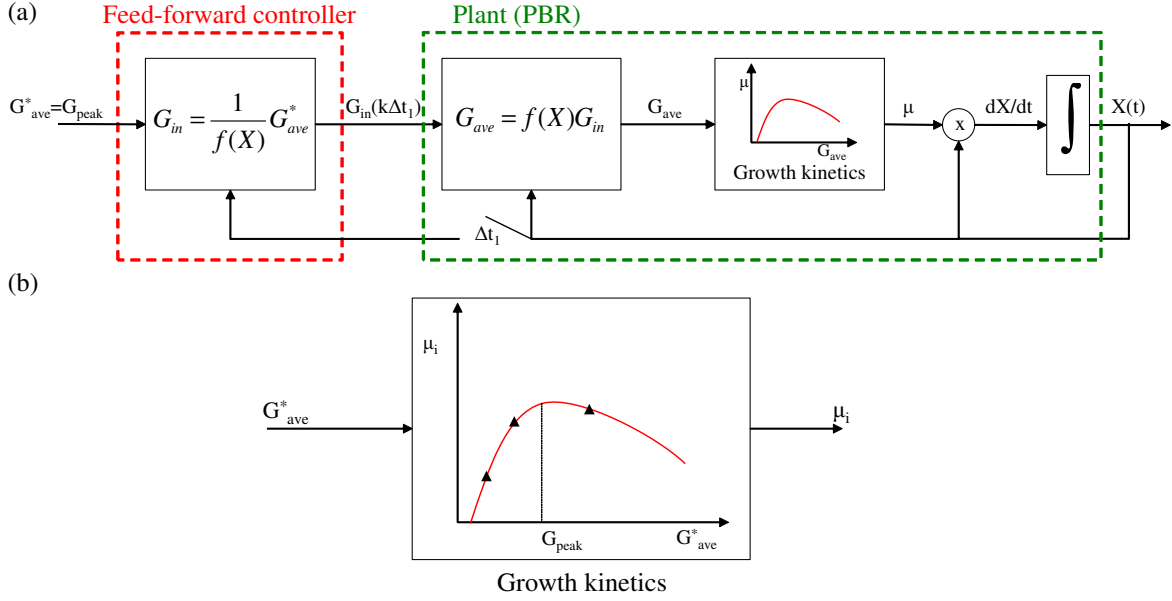
Figure 4.3: (a) Diagram of the proposed feed-forward control scheme illustrating the controller and the plant and (b) the optimal search control diagram used to estimate G_{peak} using Brent's method.

of the average fluence rate G_{ave}. The use of such a model-free optimal search algorithm increased the versatility and the applicability of the control strategy developed to any microorganism species or to other photochemical processes.

In practice, the optimal search, illustrated in Figure 4.3b, preceded the feed-forward control of incident irradiance on the PBR (Figure 4.3a). First, the PBR was exposed to three different irradiances G_{in} on each side namely, 30, 63, and 132 $\mu\mathrm{mol}_{h\nu}/\mathrm{m}^2\cdot$s. The corresponding average fluence rate test values G^*_{ave} were estimated using Equation (4.10), for a duration $\Delta t_2 = 3$ hours, as 59, 125, and 265 $\mu\mathrm{mol}_{h\nu}/\mathrm{m}^2\cdot$s. Note that Equation (4.10) simplifies to $G_{ave} \approx 2G_{in}$ at the beginning of the growth stage, since $\delta_\lambda XL << 1$. This suggests that the model $f(X)$ is not necessary to determine the optimal average fluence rate G_{peak}. This is a great feature of the present optimal search method. However, as the mass concentration $X(t)$ increases, the condition $\delta_\lambda XL << 1$ is no longer valid and the feed-forward controller has to rely on $f(X)$ to set the incident irradiance G_{in}. Then, the control

91

performance relies on the closeness of the model $f(X)$ to the actual system. The sensitivity analysis for the present experimental system is discussed later in Section 4.2. However, the control system is robustly stable with respect to uncertainties/modeling error of $f(X)$, since the feed-forward gain $1/f(X)$ is bounded by the linear dependency of the function $f(X)$ with respect to X as the latter increases. The test values for the average fluence rate G_{ave}^* were chosen to fall in the photolimited and the photoinhibited regions based on growth kinetics data reported by Huertas and Lubian [145]. Note that this was performed for convenience and it was not essential to the implementation of the optimal search. The average growth rate during each period of constant irradiance was estimated in two different ways. It was first estimated by fitting the mass concentration to Equation (4.6), assuming μ to be constant and equal to $\bar{\mu}$ such that

$$X = X_0 e^{\bar{\mu}t} \tag{4.12}$$

Alternatively, the growth rate was estimated at regular time intervals Δt_3 according to

$$\mu_i = \frac{1}{\Delta t_3} ln \left[\frac{X(t_i + \Delta t_3)}{X(t_i)} \right] \tag{4.13}$$

Here, Δt_3 was set to 30 minutes to maximize signal to noise ratio. Smaller values of Δt_3 resulted in large fluctuations in μ_i. Then, the average growth rate μ_{ave} for each period was estimated according to

$$\mu_{ave} = \frac{1}{n} \sum_{i=1}^{n} \mu_i \tag{4.14}$$

where n is the number of growth rate estimates. It was equal to 24 calculated from 36 mass concentration samples $X(t_i)$ at sampling interval Δt_1 of 5 minutes per fitting period Δt_2 of 3 hours. If the growth rate is constant during this period, $\bar{\mu}$ and μ_{ave} should be identical. The estimated average growth rates μ_{ave} or $\bar{\mu}$ for each of the three periods as functions of the corresponding average fluence rate G_{ave} were then fitted to a second order polynomial. Based on Brent's method, the abscissa corresponding to the maximum of this polynomial was identified as the estimated optimum average fluence rate G_{peak}. Note that Δt_2 needed to be large enough so that the signal to noise ratio of the mass concentration measurements did not introduce an error in the estimated growth rate. It also had to be small enough so

that changes in the operating conditions could be ignored during the optimal search period.

Once the optimum average fluence rate G_{peak} was obtained, the feed-forward control scheme (Figure 4.3a) adjusted the incident irradiance G_{in} estimated using Equation (4.10) every 5 minutes based on (i) the optimum average fluence rate G_{peak}, (ii) the mass concentration $X(t)$ measured by the sensor, and (iii) δ_λ calculated from the measured radiation characteristics of *N. oculata* [114]. Note that in this experiment, the optimal search took place in the initial stage where $\delta_\lambda X L$ was significantly smaller than unity thus simplifying Equation (4.10) to $G_{ave} = 2G_{in}$. Therefore, mass concentration measurements were not necessary for the radiation transfer model. If the optimal search is set active during the process, the mass concentration dependent nonlinear gain must be applied so that a varying incident irradiance G_{in} will render a constant average fluence rate G_{ave}.

4.4   Results and Discussion

4.4.1   Optimum average fluence rate

Figure 4.4a shows the temporal evolution of microalgae dry mass concentration $X(t)$ for each incident irradiance G_{in} on each side of the PBR for the 9 hours of the optimal search. It indicates that the microalgae concentration increased under all three different values of G_{in} imposed. The average growth rate $\bar{\mu}$ was retrieved by fitting the mass concentration $X(t)$ to Equation (4.12). Figure 4.4b shows the growth rate $\bar{\mu}$ estimated by fitting the experimental data to Equation (4.12) as a function of the duration of the fitting period ranging from 15 to 180 minutes for each value of G_{in} imposed. The results indicate that the growth rate $\bar{\mu}$ corresponding to $G_{in} = 63$ and 132 $\mu\text{mol}_{h\nu}/\text{m}^2 \cdot \text{s}$ converged to a constant value for fitting periods longer than 120 minutes. On the other hand, 150 minutes were required for the value of the growth rate $\bar{\mu}$ to converge when G_{in} was 30 $\mu\text{mol}_{h\nu}/\text{m}^2 \cdot \text{s}$. This can be attributed to an initial lag period observed after transferring the culture to the PBR. Overall, the average growth rate $\bar{\mu}$ was found to be 0.008, 0.038, and 0.060 h^{-1} for G_{in} equal to 30, 63, and 132 $\mu\text{mol}_{h\nu}/\text{m}^2 \cdot \text{s}$, respectively. The corresponding average fluence rate G_{ave}^* was estimated,
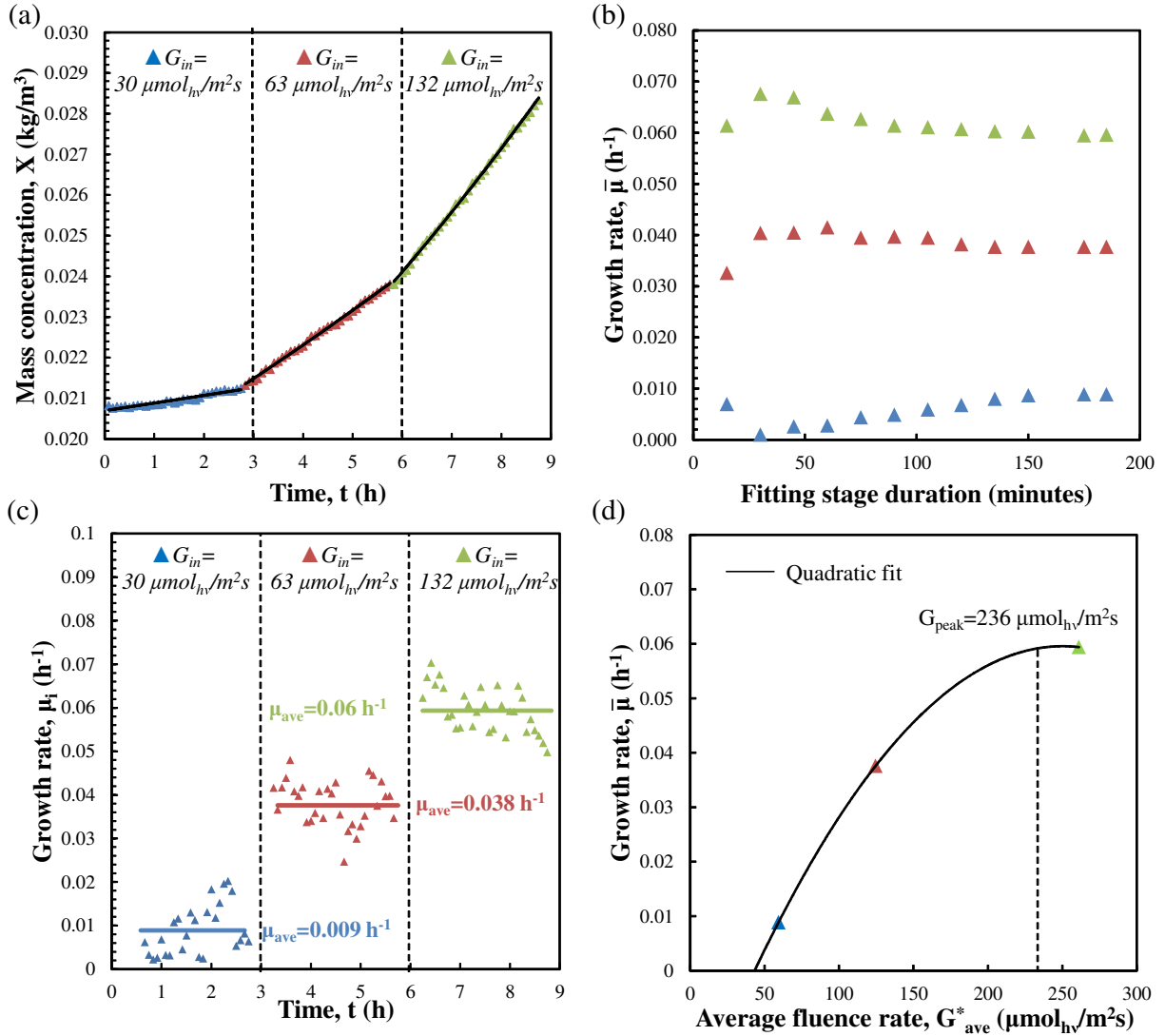
Figure 4.4: Temporal evolution, during the optimal search of (a) the mass concentration $X(t)$, (b) the average growth rate $\bar{\mu}$ (h^{-1}) as a function of fitting period duration, (c) the growth rate $\mu_i(t)$ of *N. oculata*, and (d) fitted growth rate $\bar{\mu}$ versus average fluence rate G^*_{ave}. The optimum average fluence rate was $G_{peak} = 236$ μmol$_{h\nu}$/m^2·s.

based on Equation (4.10), as 59, 125, and 261 μmol$_{h\nu}$/m^2·s, respectively.

Furthermore, Figure 4.4c shows the growth rate μ_i calculated using Equation (4.13) for $\Delta t_3 = 0.5$ hour. The growth rates estimated by this method were noisy and scattered. However, the average growth rate μ_{ave} [Equation (4.14)] for each period fell within 5% of

94

the fitted average growth rate $\bar{\mu}$ plotted in Figure 4.4b. These results provided confidence in the estimated value of the average growth rates $\bar{\mu}$ and μ_{ave}.

Finally, Figure 4.4d shows the function $\bar{\mu}(G^*_{ave})$ fitted to a second order polynomial. The fitting polynomial intercepted the x-axis (i.e., $\bar{\mu}(G^*_{ave}) = 0$) for $G^*_{ave} = 45$ μmol$_{h\nu}$/m^2·s corresponding to $G_{in} = 23$ μmol$_{h\nu}$/m^2·s for a mass concentration $X(t)$ equal to 0.02 kg/m^3. This offset compensated for the energy required for respiration or biomass maintenance. The ability of the model-free optimal search to identify respiration and the respiration compensation point of the species further demonstrates its versatility and value. Note that the respiration compensation point was similar in magnitude to 10 μmol$_{h\nu}$/m^2·s reported by Takache et $al.$ [75] for $Chlamydomonas$ $reinhardtii$ grown in a 1.5 L torus PBR with a 3 cm thickness illuminated from one side by 250 μmol$_{h\nu}$/m^2·s white LEDs. The difference in the respiration compensation point obtained from the two experiments can be attributed to the different light sources and microalgae species.

Moreover, the optimum average fluence rate G_{peak} was identified as 236 μmol$_{h\nu}$/m^2·s by Brent's method from the three points relating the average growth rate $\bar{\mu}$ and the average fluence rate G^*_{ave}. This significantly differed from the values of 52 μmol$_{h\nu}$/m^2·s reported by Spolaore et $al.$ [137] and 72 μmol$_{h\nu}$/m^2·s used by Converti et $al.$ [138] for $N.$ $oculata$. The optimum incident irradiance depends on PBR geometry, operating conditions, and the spectral quality of the light source. Differing experimental conditions may explain the differences in the reported optimum average fluence rate G_{peak}. Here, the latter could be achieved by imposing $G_{in} = 120$ μmol$_{h\nu}$/m^2·s on both sides of the PBR for initial mass concentration $X_0 = 0.02$ kg/m^3, according to Equation (4.10).

The optimal search method implemented here can be applied to other microorganism species, PBR geometries, and operating conditions. It has the advantage of rapidly identifying the optimum incident irradiance for maximum growth rate. Furthermore, the optimal search procedure can be repeated during subsequent growth under feed-forward control to adjust for changes in the optimum average fluence rate due to pigment concentration [75] or due to metabolic activity [17].

4.4.2 Biomass concentration

Figure 4.5a compares the temporal evolution of biomass concentration for *N. oculata* obtained under controlled incident irradiance with that obtained by exposing the PBR to a constant incident irradiance of 90 and 165 $\mu mol_{h\nu}/m^2{\cdot}s$. The associated error bars were estimated from duplicate experiments and corresponded to 95% confidence interval. The microalgae culture exposed to constant irradiance of 90 $\mu mol_{h\nu}/m^2{\cdot}s$ featured a short lag phase and reached a saturation mass concentration of $X_f = 1.48$ kg/m^{3}after 168 hours. The culture grown under constant incident irradiance of 165 $\mu mol_{h\nu}/m^2{\cdot}s$ had the longest lag time due to photoinhibition. However, it reached a saturation concentration of $X_f = 2.08$ kg/m^3. In fact, microalgae cultures that are photolimited or exposed to lower irradiance are typically characterized by shorter lag times but reach lower saturation mass concentrations than those under higher irradiance [114, 139]. The cultures grown in the PBR exposed to controlled incident irradiance not only had a short lag time but also reached the largest saturation mass concentration at $X_f = 2.25$ kg/m^{3}after 185 hours. In fact, the mass concentration $X(t)$ of microalgae exposed to controlled irradiance was similar to those in PBR exposed to 90 $\mu mol_{h\nu}/m^2{\cdot}s$ for approximately the first 50 hours. Note that the optimal search period was relatively short and did not significantly delay the biomass growth.

Furthermore, the average volumetric batch productivity P_v, [Equation (4.7)] over 180 hours of operation was 0.326 kg/m$^3{\cdot}$day when exposed to controlled incident irradiance compared with 0.216 and 0.264 kg/m$^3{\cdot}$day when exposed to a constant incident irradiance of 90 and 165 $\mu mol_{h\nu}/m^2{\cdot}s$, respectively. These corresponded to areal productivities P_A of 1.63, 1.08, and 1.32 g/m$^2{\cdot}$day, respectively. This corresponded to a relative increase of 51 % and 26 % in daily volumetric or areal productivity, respectively. These results demonstrates the advantages of controlling the incident irradiance during microalgae growth in batch mode.

Figure 4.5b shows the incident irradiance G_{in} imposed on each face of the PBR as a function of time during the different experiments. It ranged from 120 to 270 $\mu mol_{h\nu}/m^2{\cdot}s$ during the control stage compared with the constant incident irradiance of 90 $\mu mol_{h\nu}/m^2{\cdot}s$
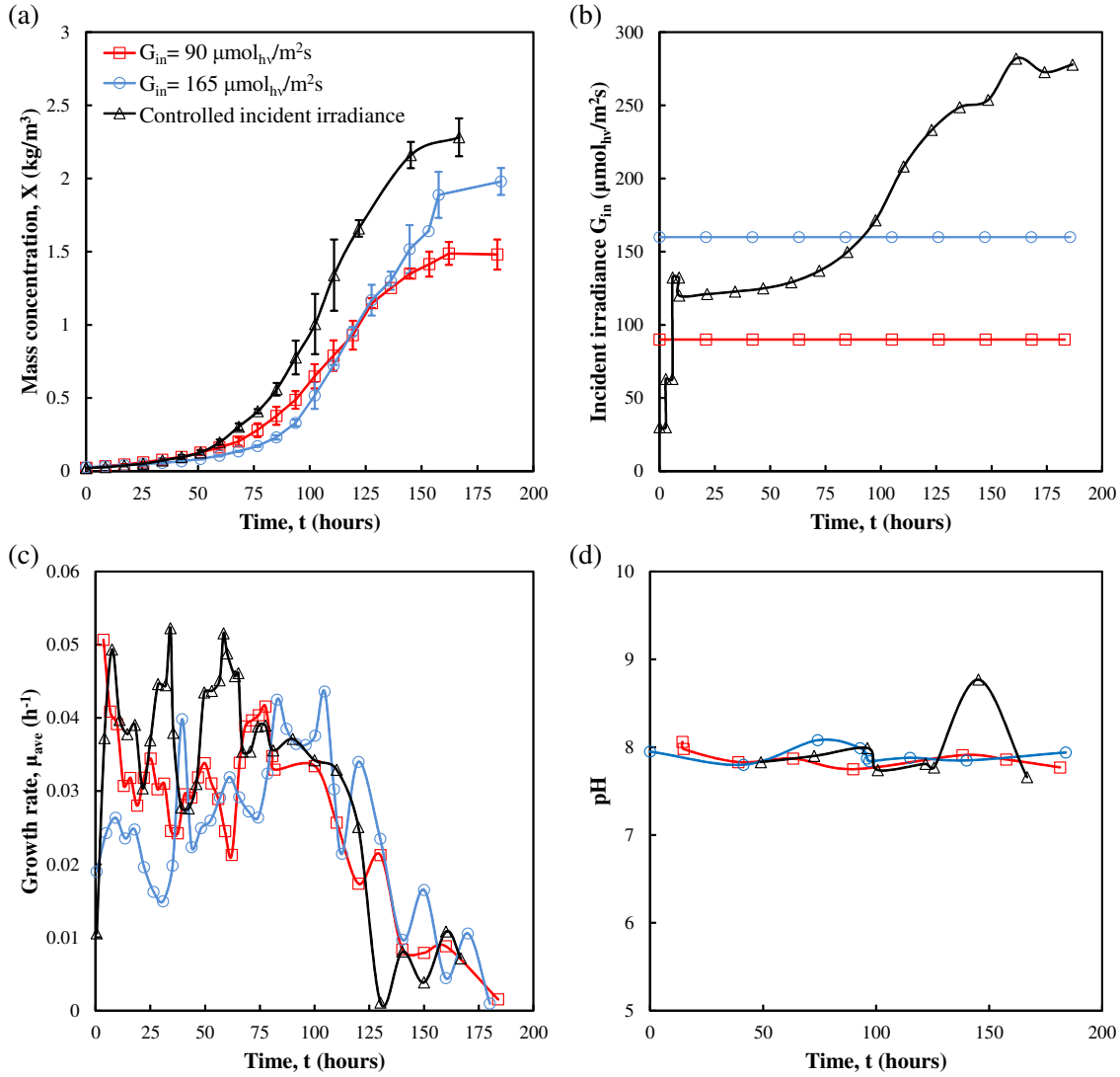
Figure 4.5: Comparison of the temporal evolution of (a) the mass concentration $X(t)$, (b) the PAR-averaged incident irradiance G_{in} on each face of the PBR, (c) the growth rate $\mu_{ave}(t)$, and (d) the pH of the medium for *N. oculata* grown in flat-plate PBR exposed to controlled or constant incident irradiance of 90 and 165 μmol$_{h\nu}$/m^2·s.

and 165 μmol$_{h\nu}$/m^2·s. Note that for $X \geq 1.5$ kg/m^3, the concentration signal from the sensor was noisy, as previously discussed. However, it was still used in the feed-forward control as the microalgae were reaching their saturation mass concentration. This resulted in noisy

incident irradiance G_{in} estimated using Equation (4.10). This issue could be overcome by using an array of sensors operating over complementary concentration ranges [146]. The PAR averaged fluence rate $G_{PAR}(z)$ in the PBR varied by less than 15 % with depth for biomass concentration up of 2.5 kg/m^3. This observation confirmed the use of the average fluence rate G_{ave} to couple growth rate μ to the incident irradiance G_{in}. Finally, to apply this method of cultivation to PBRs other than flat-plate PBRs, it is necessary to substitute Equation (4.1) with the appropriate expression of the fluence rate relevant to the specific PBR geometry. Note however that the validity of the two-flux approximation and Equation (4.1) has been established for open ponds and vertical flat-plate PBRs [116]. In addition, Cornet [147] derived an analytical expression for the local fluence rate in tubular PBRs, such as those described by Olivieri *et al.* [148], based on the two-flux approximation. Alternatively, the RTE can be solved numerically thus removing any restrictions on PBR geometry but with added complexity [116].

To determine the sensitivity of the feed-forward control scheme, the effects of uncertainty in the measured mass concentration were assessed with respect to the optimum incident irradiance set by the controller and the growth rate of the microorganisms. Underestimating the measured mass concentration of $X = 2$ kg/m^3 by 10%, for example, would result in (i) an incident irradiance 6% smaller than its optimum value according to Equation (4.10) and (ii) an average fluence rate G_{ave} 6% smaller than the optimum average fluence rate G_{peak}. Then using the parabolic relationship obtained between growth rate μ and G_{ave} (Figure 4.4d), the 10% uncertainty in X would result in up to 1.5% decrease in the growth rate μ relative to its maximum value. This relatively small decrease in growth rate illustrates the robustness of the feed-forward control method proposed in this study.

Figure 4.5c shows the growth rate μ_{ave} as a function of time for the three different experiments. Under constant irradiance $G_{in}= 90$ μmol$_{h\nu}$/m^2·s, the growth rate reached its peak of 0.032 h^{-1} after 1 hour and steadily decreased thereafter. On the other hand, under $G_{in} = 165$ μmol$_{h\nu}$/m^2·s the growth rate reached a maximum at 0.042 h^{-1} after approximately 80 hours of operation. This was a significantly longer lag time compared with other illumina-

tion conditions and was evident in the corresponding mass concentration (Figure 4.5a). By contrast, under controlled irradiance, the growth rate fluctuated between 0.05 and 0.03 h^{-1} for up to 120 hours of operation. These oscillations could be due to fluctuating pH and dissolved CO_2 concentration. In addition, the signal to noise ratio from the mass concentration sensors was too low to accurately estimate the growth rate for concentrations larger than 1.5 kg/m^3. Finally, at the end of the growth phase, the nutrients in the medium may have been depleted resulting in nutrient-limited growth conditions leading to a decrease in growth rate that could not be compensated by adjusting the incident light. In fact, nutrient availability in the medium can be estimated by stoichiometric calculation similar to that reported by Kandilian *et al.* [114]. It was assumed that *N. oculata* cells were elementally composed of 8% nitrogen and 1% phosphate by dry mass [17]. This suggests that the culture experienced phosphate limitation at a biomass concentration of 1.2 kg/m^3 and a nitrogen limitation at around 2.1 kg/m^3.

Figure 4.5d shows the temporal evolution of the pH of the growth medium averaged between duplicates PBR 1 and PBR 2 and sampled once a day for all experiments. The relative difference in pH between PBR 1 and PBR 2 was negligible at all times. The pH varied between 7.7 and 8.0 and was maintained in the desired range by increasing the CO_2 flow rate as the microalgae mass concentration increased. Here, the microalgae *N. oculata* showed the largest growth rate in the 7.7 to 8.0 range, despite conflicting literature reports [136–138,145]. Note that no effort was made to continuously maintain a specific pH in the PBR other than daily adjustment of the CO_2 flow rate. Nevertheless, further increase in microalgae growth rate could be achieved by applying the same optimal search methodology based on Brent's method to the CO_2 concentration and continuously adjusting the CO_2 injection rate. Further improvements may also require controlling the dissolved concentrations of individual nutrients in the growth medium to avoid inhibition or limitation by one or several nutrient ingredients.

4.5 Chapter summary

This study developed a versatile and general control methodology consisting of (i) a model-free optimal search based on Brent's method and (ii) a feed-forward inversion control of incident irradiance based on continuous mass concentration measurements. For demonstration purposes, marine microalgae *N. oculata* was grown in batch mode in 1 cm thick flat-plate PBRs exposed to red light from both sides. The optimal search successfully estimated the optimum average fluence rate as 236 μmol$_{h\nu}$/m^2·s corresponding to a specific growth rate of 0.06 h^{-1}. The microalgae exposed to controlled incident irradiance had a very short lag time and reached saturation mass concentration of 2.25 kg/m^3. This should be compared with 1.48 and 2.08 kg/m^3 for microalgae grown under 90 and 165 μmol$_{h\nu}$/m^2·s, respectively. This corresponded to an average productivity of 0.326 kg/m^3·day compared with 0.216 and 0.264 kg/m^3·day, respectively. The method demonstrated in this study can be used for any microorganism species and PBR design, as well as for operating parameters other than incident irradiance such as the pH and the medium composition.

CHAPTER 5

Influence of Light Absorption Rate by *Nannochloropsis oculata* on Triglyceride Production During Nitrogen Starvation

Large amount of triglyceride fatty-acid (TG-FA) can be produced by nitrogen starvation of *N. oculata*. However, the effect of light transfer in the PBR on TG-FA production is not well understood. This chapter elucidates the role of light absorption on TG-FA cell content and productivity. These results presented in this chapter will be instrumental in defining protocols for TG-FA production in scaled-up photobioreactors.

5.1   Introduction

Several strategies can be used to enhance lipid productivity [17]. For example, nitrogen starvation triggers large amounts of lipid accumulation [39, 149]. The stressful conditions of nitrogen starvation lead cells to synthesize neutral lipids mainly in the form of triglyceride fatty acids (TG-FA) [39]. They are believed to serve as carbon and energy storage compound for the cells [149]. TG-FA are the main feedstock for lipid to biodiesel conversion through transesterification reaction with methanol to produce methyl esters of fatty acids that are essentially biodiesel [5]. The accumulation of TG-FA during nitrogen starvation has been observed in numerous microalgal species including *Nannochloropsis oculata* [39], *Nannochloropsis* sp. [150], *Neochloris oleoabundans* [151], *Scenedesmus obliquus* [152], *Chlorella sp.*, and many others [153]. Typically, 40-50 dry wt.% is the maximum concentration of TG-FA reported in microalgae cells [149]. In addition, subjecting the cells to intense light

during nitrogen starvation has been shown to be essential in TG-FA synthesis [39,149]. This is in contrast to the synthesis and accumulation of polar lipids under light limited growth conditions [149]. On the other hand, Breuer *et al.* [152] demonstrated that TG-FA accumulation in *Scenedesmus obliquus* was independent of photon flux density (PFD) in batch grown cultures.

One of the consequences of nitrogen starvation is the reduction in the total pigment concentration in the cells as well as the increase in carotenoid to chlorophyll *a* (chl*a*) concentration ratio [154]. Pruvost *et al.* [151] observed a ten fold decrease in total pigment concentration in *Neochloris oleoabundans* cells during nitrogen starvation. In addition, changes in chl*a* to carotenoid ratio greatly modifies the color and light absorption of microorganisms thus affecting their ability to perform photosynthesis and accumulate TG-FA [39].

5.2   Background

5.2.1   Nitrogen starvation

The radiation characteristics and optical properties of *N. oculata* in batch grown cultures over the photosynthetically active radiation (PAR) region were reported in Chapter 2. A significant decrease in the absorption cross-section of the cells at wavelengths between 400 and 750 nm was observed during nitrogen limitation compared with cells grown in nitrogen replete media [114]. Furthermore, Flynn *et al.* [155] demonstrated that nitrogen deprived *N. oculata* cells can undergo two cell divisions after the onset of NH_4^+ deprivation. To do so, each cell divides its nitrogen content between the daughter cells [155]. In fact, the authors reported that nitrogen replete *N. oculata* cells had a carbon to nitrogen ratio (C/N) of 6 while NH_4^+ deprived cells featured C/N ratio of nearly 26 [155].

Nitrogen starvation of *N. oculata* cultures can be achieved by two methods. *Sudden starvation* consists of two steps: first, microalgae are grown in nitrogen replete conditions. Then, they are transferred into a nitrogen-free medium. *Progressive starvation* consists of initially adding a small amount of nitrogen to the culture medium in the form of nitrate, for

example. After inoculating the PBR, the microalgae grow and multiply until they consume all the nitrates in the medium and the culture medium becomes deprived of nitrogen. Cells subjected to progressive nitrogen starvation have a slightly different behavior than those in sudden starvation [39]. Indeed, the culture goes through a nitrogen replete phase followed by nitrogen limitation phase and finally a nitrogen starvation phase. By contrast, in sudden starvation, the cells go from a nitrogen replete phase directly to a nitrogen starvation phase. Nitrogen limitation results in a decrease in pigment concentrations. Therefore, cells undergoing progressive starvation enter the nitrogen starvation phase with significantly lower pigment concentrations than those subjected to sudden starvation. This modifies the light availability in the PBR in a non-obvious way. Finally, both methods can lead to appreciable amount of TG-FA accumulation [39]. However, in practice, progressive starvation is preferable for mass production as it requires only one production stage and does not require the costly biomass filteration/separation from growth medium and re-suspension in a nitrogen-free medium [39, 156].

5.2.2   Effect of light on *N. oculata* TG-FA productivity

Van Vooren *et al.* [39] demonstrated that greater light availability in flat-plate PBRs used to cultivate *N. oculata* in nitrogen starvation resulted in larger lipid productivity. Indeed, peak areal TG-FA productivity was 3.6 g/m^2·day for sudden starvation of batch culture with initial biomass concentration of 0.41 kg/m^3 exposed to 250 μmol$_{h\nu}$/m^2·s compared with 1.4 g/m^2·day for the same illumination conditions when the initial biomass concentration was 0.76 kg/m^3. The larger initial biomass concentration resulted in stronger light attenuation and lower light availability in the PBR. Similarly, *N. oculata* cultivated in a 5 cm flat-plate PBR had 50% lower TG-FA productivity than those cultivated in 3 cm flat-plate PBR under the same conditions. Pal *et al.* [150] also showed that nitrogen starved *Nannochloropsis sp.* grown in cylindrical PBR 6 cm in diameter and exposed to 750 μmol$_{h\nu}$/m^2·s of white light contained 35% total lipids by dry weight compared with 22% for cells grown exposed to 170 μmol$_{h\nu}$/m^2·s.

These studies established the existence of a relationship between the light attenuation conditions in the PBR and lipid or TG-FA accumulation in the cells. In order to examine this link further, it is necessary to perform light transfer analysis in the PBR and relate it to the kinetics of lipid accumulation in the cells. To do so, the radiation characteristics of the microalgae as a function of time are necessary during nitrogen starvation [8]. Because the cells undergo large changes in pigment concentrations and composition, theoretical predictions could be difficult to obtain and may be inaccurate [78]. Therefore, experimental measurements were preferred in this study.

5.2.3 Light transfer model

In photochemical reactions, the reaction kinetics are proportional to the absorbed useful energy or the specific local volumetric rate of energy absorption, $\mathscr{A}$ expressed in $\mu mol_{h\nu}/g\cdot s$ [157]. In the context of photobioreactors, it represents the amount of photons absorbed per unit time and per unit weight of biomass. In the case of photosynthetic microalgae, the useful energy is contained in the PAR region defined by the spectral region between 400 and 700 nm. Therefore, the specific local volumetric rate of energy absorption depends on the absorption cross-section of the species and on the radiation field inside the PBR in the PAR region as recently shown by Pruvost and Cornet [74]. The authors developed a model predicting the maximum biomass productivity of both microalgae [158] and cyanobacteria [73] in various PBRs as a function of PFD. The authors used the specific mean volumetric rate of energy absorption (MVREA) denoted by $\langle \mathscr{A} \rangle$ and the photosynthesis half saturation constant of the microorganism to obtain an analytic expression for the biomass productivity [74]. The MVREA $\langle \mathscr{A} \rangle$ can be expressed as [74]

$$\langle \mathscr{A} \rangle = \frac{1}{L} \int_{400}^{700} \int_0^L \bar{A}_{abs,\lambda} G_\lambda(z) dz d\lambda \tag{5.1}$$

where $\bar{A}_{abs,\lambda}$ is the average spectral mass absorption cross-section of the microalgae (in m^2/kg), $G_\lambda(z)$ is the local fluence rate in $\mu mol_{h\nu}/m^2\cdot s$, and L is the thickness of the PBR (in m). The MVREA $\langle \mathscr{A} \rangle$ accounts for the cumulative effects of (i) biomass concentration,

(ii) absorption cross-section of the microalgae, and (iii) the fluence rate inside the PBR. Note that all these parameters vary during the course of nitrogen starvation experiments. Therefore, $\langle \mathscr{A} \rangle$ is more indicative of the amount of light absorbed by the microalgae than the fluence rate in the PBR or the absorption cross-section of the cells considered separately.

In the case of absorbing and scattering media such as microalgal culture, the local spectral fluence rate $G_\lambda(z)$ can be obtained by solving the radiative transfer equation [35]. Several methods of solution exist [8,116,129]. However, for one-dimensional flat-plate PBRs with transparent front window containing strongly forward scattering microalgae, the two-flux approximation yields satisfactory results [41,116]. In the case of normally incident radiation $G_{\lambda,0}$, the local fluence rate $G_\lambda(z)$ at depth z can be expressed as

$$\frac{G_\lambda(z)}{G_{\lambda,0}} = 2\frac{[\rho_\lambda(1+\alpha_\lambda)e^{-\delta_\lambda L} - (1-\alpha_\lambda)e^{-\delta_\lambda L}]e^{\delta_\lambda z} + [(1+\alpha_\lambda)e^{\delta_\lambda L} - \rho_\lambda(1-\alpha_\lambda)e^{\delta_\lambda L}]e^{-\delta_\lambda z}}{(1+\alpha_\lambda)^2 e^{\delta_\lambda L} - (1-\alpha_\lambda)^2 e^{-\delta_\lambda L} - \rho_\lambda(1-\alpha_\lambda^2)e^{\delta_\lambda L} + \rho_\lambda(1-\alpha_\lambda^2)e^{-\delta_\lambda L}} \tag{5.2}$$

where ρ_λ is the diffuse reflectance of the PBR's back wall while the coefficients α_λ and δ_λ are expressed as [41]

$$\alpha_\lambda = \sqrt{\frac{\bar{A}_{abs,\lambda}}{\bar{A}_{abs,\lambda} + 2b_\lambda \bar{S}_{sca,\lambda}}} \quad \text{and} \quad \delta_\lambda = X\sqrt{\bar{A}_{abs,\lambda}\left(\bar{A}_{abs,\lambda} + 2b_\lambda \bar{S}_{sca,\lambda}\right)} \tag{5.3}$$

Here, $\bar{S}_{sca,\lambda}$ (in m^2/kg) is the average spectral mass scattering cross-section of the microalgae suspension. The biomass concentration is denoted by X and expressed in kg of dry weight per m^3 of suspension. The backward scattering ratio b_λ is defined as the fraction of the radiation scattered backwards and is estimated from the suspension's scattering phase function [41]. It is approximately constant over the PAR region and was recently measured to be 0.002 for *N. oculata* [114]. The PAR-averaged fluence rate $G_{PAR}(z)$ can be expressed as

$$G_{PAR}(z) = \int\limits_{400}^{700} G_\lambda(z)\mathrm{d}z. \tag{5.4}$$

Note that in batch cultivation, absorption and scattering cross-sections of the microalgae as well as the biomass concentration are all time-dependent.

Finally, the areal TG-FA productivity R (in g/m^2·day) of a culture can be expressed as

$$R(t) = L\frac{d[\text{TG-FA}](t)}{dt} \tag{5.5}$$

where $[\text{TG-FA}](t)$ (in kg/m^3) corresponds to the culture's TG-FA concentration at time t. In practice, with daily sampling of the culture, the areal daily average TG-FA productivity $\bar{R}$ of a batch culture can be written as

$$\bar{R}(t_i) = L\frac{[\text{TG-FA}](t_i) - [\text{TG-FA}](t_{i-1})}{(t_i - t_{i-1})} \tag{5.6}$$

where t_i and t_{i-1} correspond to two consecutive sampling times 24 hours apart.

5.2.4 Determination of radiation characteristics

5.2.4.1 Experimental determination

The average spectral mass absorption and scattering cross-sections $\bar{A}_{abs,\lambda}$ and $\bar{S}_{sca,\lambda}$ can be experimentally measured according to a procedure reviewed by Pilon *et al.* [8]. In this method, the normal-normal and normal-hemispherical transmissions of several dilute microalgae suspensions with different known concentrations are measured using a spectrometer equipped with an integrating sphere. First, the apparent extinction coefficient ξ_λ can be obtained from normal-normal transmittance $T_{n,\lambda}$ measurements of cuvettes, of pathlength t, filled with microalgae suspension $T_{n,\lambda,X}$ or with the reference medium $T_{n,\lambda,ref}$

$$\xi_\lambda = -\frac{1}{t}ln\left(\frac{T_{n,\lambda,X}}{T_{n,\lambda,ref}}\right) \tag{5.7}$$

Similarly, the apparent absorption coefficient $\xi_{h,\lambda}$ can be defined from the hemispherical transmittance $T_{h,\lambda}$ by

$$\xi_{h,\lambda} = -\frac{1}{t}ln\left(\frac{T_{h,\lambda,X}}{T_{h,\lambda,ref}}\right) \tag{5.8}$$

The apparent extinction coefficient ξ_λ can be expressed as a function of the actual absorption κ_λ and scattering $\sigma_{s,\lambda}$ coefficients

$$\xi_\lambda = \kappa_\lambda + (1 - \epsilon_n)\sigma_{s,\lambda}. \tag{5.9}$$

106

Here, ϵ_n represents the fraction of light scattered in the forward direction and detected by the spectrometer. Ideally, ϵ_n is equal to unity. However, due to the finite size of the acceptance angle of the detector, ϵ_n is typically smaller than 1 and is assumed to be constant over the PAR region. It is estimated from microorganism scattering phase function $\Phi_\lambda(\Theta)$ as follows

$$\epsilon_n = \frac{1}{2} \int_0^{\Theta_a} \Phi_\lambda(\Theta) sin(\Theta) d\Theta \qquad (5.10)$$

where Θ_a is the half acceptance angle of the detector. The actual extinction coefficient $\beta_\lambda = \kappa_\lambda + \sigma_{s,\lambda}$ can then be determined according to

$$\beta_\lambda = \frac{\xi_\lambda - \epsilon_n \kappa_\lambda}{1 - \epsilon_n} \qquad (5.11)$$

Similarly, the apparent absorption coefficient $\xi_{h,\lambda}$ can be related to the real absorption κ_λ and scattering $\sigma_{s,\lambda}$ coefficients as

$$\xi_{h,\lambda} = \kappa_\lambda + (1 - \epsilon_h)\sigma_{s,\lambda} \qquad (5.12)$$

Here, ϵ_h is the fraction of the scattered light detected by the detector. Ideally, when all the scattered light is accounted for, ϵ_h is equal to unity. Moreover, at $\lambda = 750$ nm the microorganisms are assumed to be non-absorbing, i.e., $\kappa_{750} = 0$ m^{-1}. Then, Equations (5.9) and (5.12) at 750 nm simplify to

$$\xi_{h,750} = (1 - \epsilon_h)\sigma_{s,750} \quad \text{and} \quad \xi_{750} = (1 - \epsilon_n)\sigma_{s,750} \qquad (5.13)$$

Combining Equations (5.11) to (5.13) yields

$$\kappa_\lambda = \xi_{h,\lambda} - \xi_{h,750}\frac{\xi_\lambda - \xi_{h,\lambda}}{\xi_{750} - \xi_{h,750}} \quad \text{and} \quad \sigma_{s,\lambda} = \frac{\xi_\lambda - \epsilon_n \kappa_\lambda}{1 - \epsilon_n} - \kappa_\lambda \qquad (5.14)$$

Finally, the average mass absorption $\bar{A}_{abs,\lambda}$ and scattering $\bar{S}_{sca,\lambda}$ cross-sections of the microalgae are defined as

$$\bar{A}_{abs,\lambda} = \kappa_\lambda/X \quad \text{and} \quad \bar{S}_{sca,\lambda} = \sigma_{s,\lambda}/X \qquad (5.15)$$

5.2.4.2 Semi-empirical determination

Alternatively, the average mass absorption cross-section $\bar{A}_{abs,\lambda}$ of a phytoplanktonic suspension can be estimated as a weighted sum of the effective mass absorption cross-sections $a_{i,\lambda}^*$ of pigment i present in the microalgae cells [42, 159, 160]

$$\bar{A}_{abs,\lambda} = \sum_{i=1}^{n} C_i a_{i,\lambda}^* + \omega_\lambda \tag{5.16}$$

Here, C_i is the concentration of pigment i and ω_λ is a semi-empirical function independent of any pigment concentration [159, 160]. This average mass absorption cross-section takes into account the package effect responsible for a decrease in the effective absorption cross-section of the pigments once they are packaged into the cells [159, 160]. It can be estimated by considering the ratio of the *in-vivo* and *ex-vivo* absorption cross-sections of the cell's pigments [160]. Bricaud *et al.* [160] and Nelson *et al.* [159] measured the absorption cross-section $\bar{A}_{abs,\lambda}$ of various microalgae cells as well as the cells' pigment concentrations using high precision liquid chromatography (HPLC). The authors then compared the measured absorption cross-section $\bar{A}_{abs,\lambda}$ to that predicted by Equation (5.16) accounting for 20 different pigments. To minimize the error between the predicted and measured average spectral absorption cross-sections $\bar{A}_{abs,\lambda}$, both studies reported the necessity to introduce the term ω_λ in Equation (5.16) [159, 160]. However, there is no clear consensus in the literature on the origin of this term. It has been attributed to (i) intracellular pigments that cannot be extracted by solvents such as methanol or acetone [160] and (ii) to absorption by the cell walls and cytoplasm that are filtered out during pigment extraction [160, 161].

5.2.4.3 Theoretical predictions

Theoretical predictions of $\bar{A}_{abs,\lambda}$ and $\bar{S}_{sca,\lambda}$ can be obtained by Lorenz-Mie theory based on the cell size distribution and on the effective complex index of refraction of the microalgae on spectral basis over the PAR region [35, 41, 78]. Flynn *et al.* [155] observed a 30% increase in the volume of *N. oculata* cells during NH_4^+ starvation. Unfortunately, changes in the real part of the complex index of refraction due to nitrogen starvation have not been reported

in the literature. However, it is a function of the cell's composition including lipid, protein, and carbohydrates mass fractions [35]. Thus, a large increase in cell lipid content would lead to changes in the cell's effective refraction index and therefore in its average spectral scattering cross-section. Therefore, experimentally measuring the absorption and scattering cross-sections appeared to provide a more reliable and accurate method of accounting for changes in composition and cell size distribution during nitrogen starvation.

5.3 Materials and methods

5.3.1 Species and culture medium

A strain of *Nannochloropsis oculata* was obtained from Alphabiotech collection (Asserac, France). The microalgae were cultivated in a modified Conway medium using an artificial seawater (ASW) base [162] with salinity of 25 g/L. The Conway medium composition was (in mM): $Na_2EDTA \cdot 2H_2O$, 0.36; H_3BO_3, 1.63; NaH_2PO_4, 1.50; $FeCl_3 \cdot 6H_2O$, 0.01; $MnCl_2 \cdot 4H_2O$, 0.91; $ZnCl_2$, 0.023; $CoCl_2 \cdot 6H_2O$, 0.013; $CuSO_4 \cdot 5H_2O$, 0.012; $Na_2MoO_4 \cdot 5H_2O$, 0.008. The medium was filter-sterilized using 0.22 μm liquid filter (AcroPak 20, Pall Corp., Port Washington, NY).

Sudden starvation experiments were performed by inoculating the PBRs with *N. oculata* produced by a continuous PBR illuminated with 150 μmol$_{h\nu}$/m^2·s. A specific volume of culture was harvested and centrifuged at 10,000 g (ThermoScientific Sorvall RC 6 Plus, Massachusetts, USA) for 5 minutes at 4°C, washed with nitrogen-free Conway medium and injected into the PBR filled with the nitrogen-free medium. The volume of culture was chosen based on the desired initial biomass concentration of the nitrogen starvation batch.

5.3.2 Photobioreactor

The nitrogen starvation experiments were performed in batch mode in a 1L airlift-type flat-panel PBR with thickness of 3 cm. The PBR was described in more detail by Pruvost *et al.* [151]. Illumination was provided on one face of the PBR by a white LED light panel

(P4 Cool White, Seoul Semiconductor) with adjustable PFD. The illuminated surface of the PBR was made of transparent polymethyl methacrylate (PMMA) and the backwall of diffuse stainless steel with diffuse reflectance ρ_λ of 0.2 over the PAR region [158]. The incident PFD was measured over the PAR region at 12 different locations on the inside surface of the PBR using a quantum light sensor (LI-250A, LI-COR, Lincoln, NE). The measured PFD varied by less than 10% for the different locations measured the average PFDs was reported. The pH was continuously measured using a pH sensor (Mettler Toledo SG 3253) and was maintained at 8 by automatic CO_2 injection when the culture pH exceeded 8. Mixing in the PBR was provided by injecting air at a flow rate of 80 mL/min. The PBR was maintained at room temperature (approximately 22.5^{o}C) by forced air convection on the back of the PBR. Before starting each experiment, the PBR was sterilized for 30 minutes using a 5 mM peroxyacetic acid solution and rinsed twice with sterile deionized water.

5.3.3   Biomass concentration

Microorganisms dry biomass concentration X was determined gravimetrically by filtering 5 mL of culture through a pre-dried and pre-weighed 0.45 μm pore size glass-fiber filter (Whatman GF/F). The filters were dried overnight in an oven at 105°C and weighed after being cooled in a desiccator for 20 minutes. The samples were analyzed in triplicates and the reported biomass concentration corresponded to the mean value.

5.3.4   Pigment concentration

Pigments were extracted in pure methanol and quantified spectrophotometrically. A volume of 0.5 mL of culture was first centrifuged at 13,400 rpm (12,100 g) for 15 minutes. The medium was discarded and the cells were resuspended in 1.25 mL pure methanol and sonnicated for 10 seconds. Pigments were extracted for a period of 1 hour at 45°C and the extract was centrifuged. The optical density OD_λ of the supernatant was measured at wavelengths 750, 665, 652, and 480 nm using a UV-VIS-NIR spectrophotometer (Agilent

Cary 5000, Santa Clara, CA). All extractions were performed in triplicates. Chlorophyll a concentration, denoted by C_{chla}, was estimated according to the correlation [163]

$$C_{chla}[mg/L] = -8.0962(OD_{652} - OD_{750}) + 16.5169(OD_{665} - OD_{750}) \qquad (5.17)$$

Similarly, photo-protective carotenoid (PPC) concentration C_{PPC} was estimated according to [50]

$$C_{PPC}[mg/L] = 4(OD_{480} - OD_{750}) \qquad (5.18)$$

5.3.5 Radiation characteristics

The radiation characteristics of the microalgae were measured experimentally using the method reviewed by Pilon *et al.* [8]. The normal-normal transmission measurements were performed using a UV-VIS-NIR spectrophotometer (Agilent Cary 5000, Santa Clara, CA). The normal-hemispherical transmission measurements were performed using an integrating sphere attachment (Agilent Cary DRA-2500, Santa Clara, CA) to the aforementioned spectrophotometer. The experimental setup and procedure and the data analysis were successfully validated by comparing the measured scattering cross-sections of polystyrene spheres 2.02 and 4.5 μm in diameter to those predicted by Lorenz-Mie theory according to the analysis presented by Berberoğlu *et al.* [45] (see Appendix B). To avoid absorption and scattering by the growth medium, the microalgae were centrifuged at 13,400 rpm for 20 minutes and washed twice with phosphate buffer saline (PBS) solution and suspended in PBS. The measurements were performed in 1 cm pathlength quartz cuvettes (110-10-40 Hellma Analytics, Müllheim, Germany) in the wavelength range from 350 to 750 nm. The microalgae suspensions were diluted to ensure that single scattering prevailed. The average mass absorption and mass scattering cross-sections of microalgae suspensions were measured for three biomass concentrations between 0.03 and 0.10 kg/m^3 to ensure that they were independent of microalgae concentration X. The cross-sections reported correspond to the mean of the three measurements.

5.3.6 Lipid extraction

Lipid extraction was performed according to the whole cell analytic method outlined by Van Vooren *et al.* [39]. Briefly, 2 mL of culture were centrifuged for 10 minutes at 3,600 g and the supernatant was discarded. The cells were then resuspended in chloroform/methanol mixture (2:1 by volume) and sonicated for 30 seconds followed by 6 hours of light agitation on a tube roller. The extracts were dried under pure nitrogen and recovered with 1 mL of chloroform/methanol mixture (2:1 by volume). Triglyceride lipids were separated from the other lipids by solid phase extraction. Finally, the lipids were transesterified and their concentration was measured by gas chromatography with a flame ionization detector (Thermo-Fisher).

5.4 Results

Three sudden starvation experiments were performed with different initial biomass concentrations X_0. In all cases, the front face of the PBR was exposed to an incident PFD of 250 $\mu\text{mol}_{h\nu}/\text{m}^2\cdot\text{s}$.

5.4.1 Biomass concentration

Figure 5.1a shows the temporal evolution of the biomass concentration of *N. oculata* grown in batch mode and subjected to sudden nitrogen starvation with initial biomass concentrations X_0 of 0.23, 0.41, and 0.85 kg/m^3. It indicates that the biomass concentration increased nearly linearly with time in the nitrogen-free medium. Cells were able to divide despite the absence of nitrogen as previously demonstrated and discussed by Flynn *et al.* [155]. Note that nitrogen starved *N. oculata* cells featured approximately one to two orders of magnitude smaller biomass productivity than those cultivated in nitrogen replete media. The three batches reached biomass concentrations of 0.84, 1.3, and 2.18 kg/m^3 after 96 hours of cultivation, respectively. For comparison purposes, biomass concentrations reported by Van Vooren *et al.* [39] for experiments with initial concentration X_0 equal to 0.23 and 0.41

kg/m^3 were added to Figure 5.1. The values obtained in the present study agreed with those reported by Van Vooren *et al.* [39] for identical growth conditions. This confirms the repeatability of the measurements. The present study provides additional and more detailed information on the temporal evolution of *N. oculata* during nitrogen starvation.

5.4.2 Pigment concentrations

Figures 5.1b and 5.1c show the temporal evolution of chl*a* and carotenoid concentrations during sudden starvation cultivation for the three different initial biomass concentrations X_0 considered. They indicate that the cell pigment concentration decreased immediately after the microalgae were suspended in the nitrogen-free medium. Most of this decrease occurred within the first 24 hours. Here also, the pigment concentrations were similar to those reported by Van Vooren *et al.* [39]. Moreover, it is apparent that the rate of pigment loss was correlated with the initial biomass concentration. In fact, after 96 hours of cultivation, the chl*a* concentration C_{chla} in culture with X_0=0.23 kg/m^3 was 0.23 wt.% compared with 0.31 and 0.59 wt.% for cells cultivated in the same PBR with initial concentration X_0 of 0.41 and 0.85 kg/m^3, respectively. This was due to the fact that batches with smaller initial biomass concentration had larger cell growth rates. This resulted in faster decrease of cell nitrogen content thus increasing the rate of chl*a* loss in cells. Indeed, by 96 hours, the biomass concentration had grown by 3.6 times for the batch with initial concentration X_0 of 0.23 kg/m^3 while it had increased by only 3.1 and 2.4 times for batches with X_0 equal to 0.41 and 0.85 kg/m^3, respectively. These corresponded to a time-averaged growth rates of 27.6 $\times 10^{-3}$, 22.6 $\times 10^{-3}$, and 16.2 $\times 10^{-3}$ 1/h, respectively.

5.4.3 Stress index

The stress index is defined as the ratio of the optical densities (OD) of the cells' pigment extract at wavelengths 480 and 665 nm [154]. It is an indicator of the "nutrient status" of the cells as proposed by Heath *et al.* [154]. It is an indirect measure of the carotenoid to
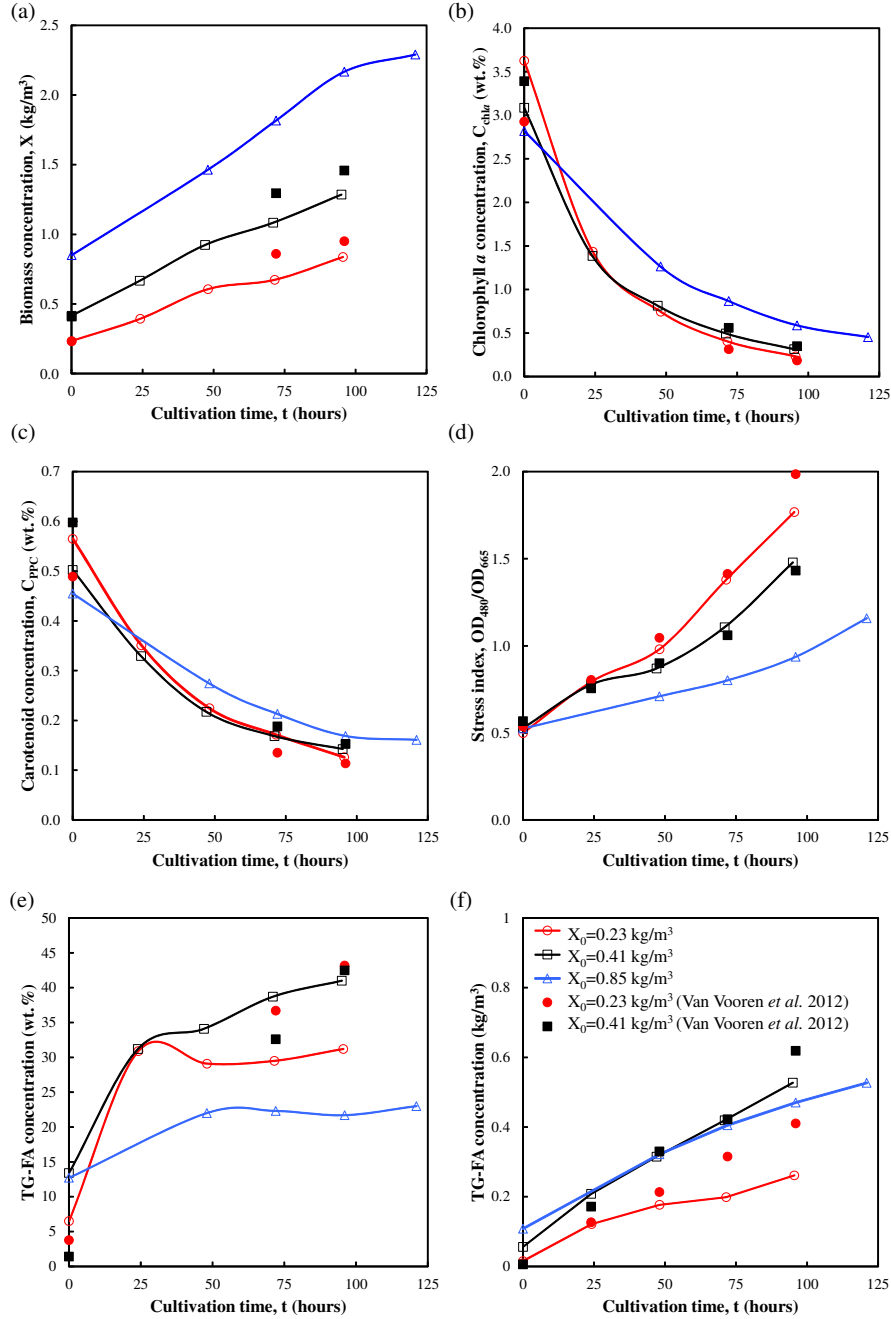
Figure 5.1: Temporal evolution of (a) biomass concentration X, (b) chlorophyll a concentration C_{chla}, (c) carotenoid concentration C_{PPC}, (d) the stress index, (e) TG-FA concentration (dry wt.%), and (f) TG-FA concentration (kg/m^3) during sudden nitrogen starvation of batch culture exposed to 250 μmol$_{h\nu}$/m^2·s with initial biomass concentrations X_0 equal to 0.23, 0.41, and 0.85 kg/m^3. Data reported by Van Vooren et $al.$ [39] for experiments with initial concentration $X_0 = 0.23$ and 0.41 kg/m^3 were added for reference.

chl$a$ ratio and it is inversely correlated to the C/N ratio of the cells [154]. Figure 5.1d shows the stress index for the three batch cultivations previously described. In nutrient replete conditions, corresponding to cultivation time $t =0$, the stress index was approximately 0.5. For all sudden starvation experiments it increased with time and was larger for cultures with smaller initial biomass concentration X_0. In fact, the stress index after 96 hours of cultivation was 1.8, 1.5, and 0.9 for cultures with initial biomass concentration X_0 of 0.23, 0.41 and 0.85 kg/m^3, respectively. This indicates that cells in the culture with initial concentration $X_0 = 0.23$ kg/m^3 had undergone more cell divisions and thus featured a larger C/N ratio.

5.4.4 TG-FA concentration

Figures 5.1e and 5.1f show the temporal evolution of the TG-FA concentration in dry wt.% and in kg/m^3, respectively, for *N. oculata* grown in batch mode and subjected to sudden nitrogen starvation with initial biomass concentrations X_0 of 0.23, 0.41, and 0.85 kg/m^3. It indicates an immediate increase in TG-FA concentration in cells following their suspension in nitrogen-free medium. Indeed, experiments with initial concentration X_0 of 0.23, 0.41, and 0.85 kg/m^3 featured cells that reached a TG-FA concentration of 30, 31, and 21 dry wt.% after 24 hours, respectively. The culture with initial concentration X_0 equal to 0.41 kg/m^3 reached a final TG-FA concentration of 41.2 dry wt.%. This compared well with the TG-FA concentration of 42 dry wt.% reported by Van Vooren *et al.* [39] for an identical experiment. On the other hand Van Vooren *et al.* [39] reported a final TG-FA concentration of 43% for sudden starvation experiment with initial biomass concentration X_0 of 0.23 k/m^3. This was significantly different from the 30 dry wt.% obtained here. In addition, it is unusual to observe a decrease in the TG-FA concentration such as that seen after 48 hours of cultivation in continuously illuminated cultures. This may be attributed to experimental uncertainties in the lipid extraction or analysis. Note, however, that other measurements (Figure 5.1a to 5.1d) were consistent with data reported by Van Vooren *et al.* [39].

5.4.5   Radiation characteristics

Figures 5.2a and 5.2b show the temporal evolution of the measured average mass absorption and scattering cross-sections in the spectral region from 350 to 750 nm for *N. oculata* during sudden nitrogen starvation of the batch culture with an initial biomass concentration X_0 of 0.23 kg/m^3. Overall, the mass absorption cross-section decreased as a function of time for all wavelengths in the PAR region. Similar results were obtained for experiments with different initial biomass concentrations (see Appendix B). The decrease in absorption cross-section was consistent with the continuous decrease in pigment concentrations over time observed in Figures 5.1b and 5.1c. For example, the chl*a* absorption peak at 676 nm decreased from 544 m^2/kg at the start of cultivation to only 43 m^2/kg after 96 hours for the culture with initial concentration X_0=0.23 kg/m^3. During the same time period, the chl*a* concentration decreased from 3.6 wt.% to 0.23 wt.%. Such sharp decrease in the mass absorption cross-section had a significant effect on the PAR-averaged fluence rate $G_{PAR}(z)$ in the PBR.

Moreover, the magnitude and shape of the average mass scattering cross-section changed slightly over time. For example, it decreased by 20% at 555 nm corresponding to the lowest absorption cross-section. However, it increased by 5.5% at wavelength 437 nm corresponding to one of chlorophyll *a* absorption peaks. Changes in the scattering cross-section overtime could be due to changes in size, shape, cellular composition, and pigment concentrations of the cells [35]. However, it is difficult to attribute the observed changes specifically to any one or more of those parameters due to the complexity of the biological response to nitrogen starvation [155].

In the present study, the concentrations of chlorophyll *a* C_{chla} and the photo-protective carotenoids C_{PPC} were measured. Then Equation (5.16) can be written as

$$\bar{A}_{abs,\lambda} = a^*_{chla,\lambda}C_{chla} + a^*_{PPC,\lambda}C_{PPC} + \omega_\lambda \tag{5.19}$$

Here, $a^*_{chla,\lambda}$ and $a^*_{PPC,\lambda}$ (in m^2/kg) correspond to the effective specific absorption cross-sections of chl*a* and PPC, respectively. Figure 5.2c presents the coefficients $a^*_{chla,\lambda}$, $a^*_{PPC,\lambda}$, and ω_λ obtained by fitting 15 experimentally measured spectral mass absorption cross-
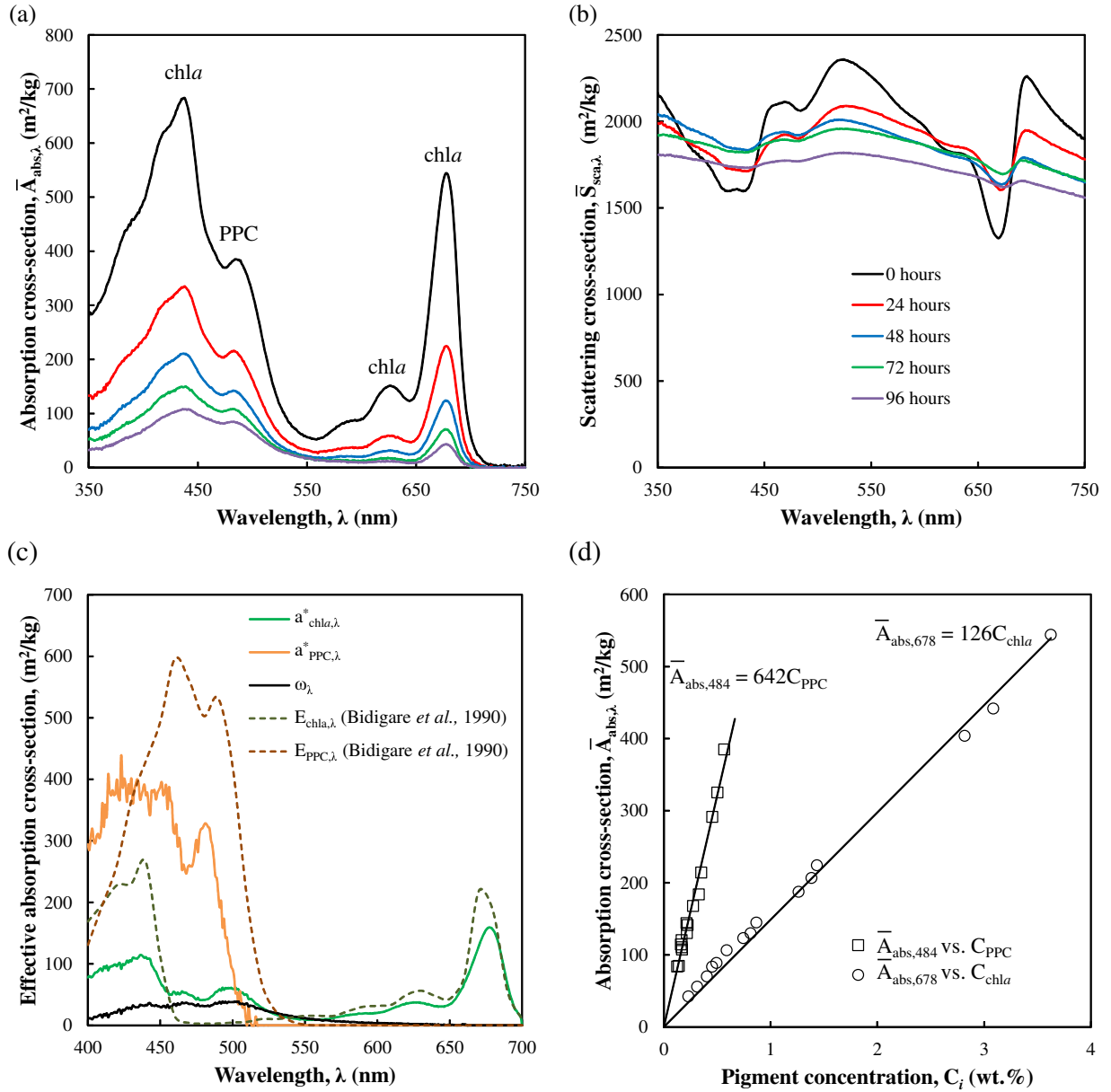
Figure 5.2:   Average mass (a) absorption and (b) scattering cross-sections of *N. oculata* after 0, 24, 48, 72, and 96 hours of cultivation during sudden nitrogen starvation of batch culture exposed to 250 $\mu mol_{h\nu}/m^2\cdot s$ with an initial biomass concentration $X_0 = 0.23$ kg/m^3. (c) Retrieved pigment effective absorption cross-sections $a^*_{chla,\lambda}$, $a^*_{PPC,\lambda}$, and coefficient ω_λ used in Equation (5.19). (d) Absorption cross-section at 676 nm $\bar{A}_{abs,676}$ as a function of chl*a* concentration C_{chla} and absorption cross-section at 484 nm $\bar{A}_{abs,484}$ as a function of carotenoid concentration C_{PPC} compiled from all three experiments.

sections to Equation (5.19) using the least squares method. It also shows the *ex-vivo* absorption cross-sections of chl$a$, $Ea_{chla,\lambda}$, and PPC, $Ea_{PPC,\lambda}$, (in m²/kg) reported by [42]. The retrieved pigment effective absorption cross-sections $a^*_{chla,\lambda}$ and $a^*_{PPC,\lambda}$ show similar trends but were smaller than those reported by Bidigare *et al.* [42]. The differences can be attributed to the package effect and was indirectly accounted for by $a^*_{i,\lambda}$ and ω_λ. Note that during nitrogen starvation the specific types of carotenoid pigments in the cells change shifting the wavelength and the magnitude of their absorption peaks [33]. However, this cannot be accounted for with spectrophotometric pigment measurements. Consequently, the absorption cross-section of carotenoids $a^*_{PPC,\lambda}$ should be considered as a mean cross-section for the various carotenoids produced by *N. oculata* during nitrogen starvation. Figure 5.2d show the measured average mass absorption cross-sections $\bar{A}_{abs,676}$ and $\bar{A}_{abs,484}$ at wavelengths 676 and 484 nm versus the simultaneously measured chl$a$ and PPC concentrations C_{chla} and C_{PPC}, respectively. Linear relationships were found between $\bar{A}_{abs,676}$ and C_{chla} and between $\bar{A}_{abs,484}$ and C_{PPC} with coefficient of determination R^2 exceeding 0.98. This provided confidence in the accuracy and the consistency of the measured radiation characteristics as well as the measured pigment concentrations for the different experiments.

5.4.6 Fluence rate and MVREA

Figure 5.3a shows the PAR-averaged fluence rate $G_{PAR}(z)$ predicted by Equations (5.2) to (5.4) as a function of PBR depth z using the radiation characteristics measured after 0 and 96 hours during sudden starvation experiments with initial biomass concentration X_0 of 0.23, 0.41, and 0.85 kg/m³. As expected, the fluence rate $G_{PAR}(z)$, at any given time, was larger for the cultures with smaller biomass concentration. In addition, for all three batches, the fluence rate after 96 hours of cultivation was larger than the initial fluence rate despite the significantly larger biomass concentration (Figure 5.1a). This was due to the decrease in the absorption cross-section (Figure 5.2a) whose magnitude was significantly larger than the increase in biomass concentration. A similar increase in fluence rate as a function of time was experimentally observed by Pruvost *et al.* [151] during nitrogen starvation cultivation of

Neochloris oleoabundans in a flat-plate PBR. However, the fluence rate alone is not indicative of the amount of light absorbed by the cells [74]. Indeed, the absorption cross-section must also be considered as it accounts for the average amount of light absorbed by the cells. In fact, this is an important consideration during nitrogen starvation given the sharp decrease in absorption cross-section and the simultaneous increase in biomass concentration.

Figure 5.3b shows the mean volumetric rate of energy absorption (MVREA) $\langle \mathscr{A} \rangle$, as a function of time for each sudden nitrogen starvation cultivation. It was estimated by Equations (5.1) to (5.3) using the corresponding experimentally measured average spectral mass absorption and scattering cross-sections $\bar{A}_{abs,\lambda}$ and $\bar{S}_{sca,\lambda}$. Here also, $\langle \mathscr{A} \rangle$ was larger for batches with smaller initial biomass concentration at all times. This could be attributed to the correspondingly larger fluence rate in the PBR (Figure 5.3a). In addition, $\langle \mathscr{A} \rangle$ decreased with time for all three experiments. For example, in the sudden nitrogen starvation experiment with $X_0 = 0.23$ kg/m^3, $\langle \mathscr{A} \rangle$ was 24 $\mu mol_{h\nu}$/g·s initially but decreased to 6.6 and 5.4 $\mu mol_{h\nu}$/g·s after 72 and 96 hours, respectively. This may seem counterintuitive since the fluence rate increased during nitrogen starvation (Figure 5.3a). However, the decrease in the absorption cross-section dominated over the increase in the fluence rate. As previously suggested, MVREA $\langle \mathscr{A} \rangle$ is indicative of the amount of energy absorbed by the microalgae, unlike the fluence rate $G_{PAR}(z)$. The decrease in MVREA $\langle \mathscr{A} \rangle$ demonstrates that, on average, the energy absorbed per cell decreased during nitrogen starvation. This may negatively impact both cell division and lipid synthesis [74]. Indeed, microalgae rely on the absorption of incident photons to carry out biochemical reactions. Their inability to absorb light could reduce their efficacy in performing photosynthesis and in fixating inorganic carbon [17].

5.4.7   TG-FA productivity

As previously discussed, cells synthesize TG-FA to store carbon and energy. Thus, the rate of TG-FA production should correlate with the mean volumetric rate of energy absorption (MVREA). The daily areal average productivity $\bar{R}(t_i)$ was estimated from experimental

119

(a)

(b)
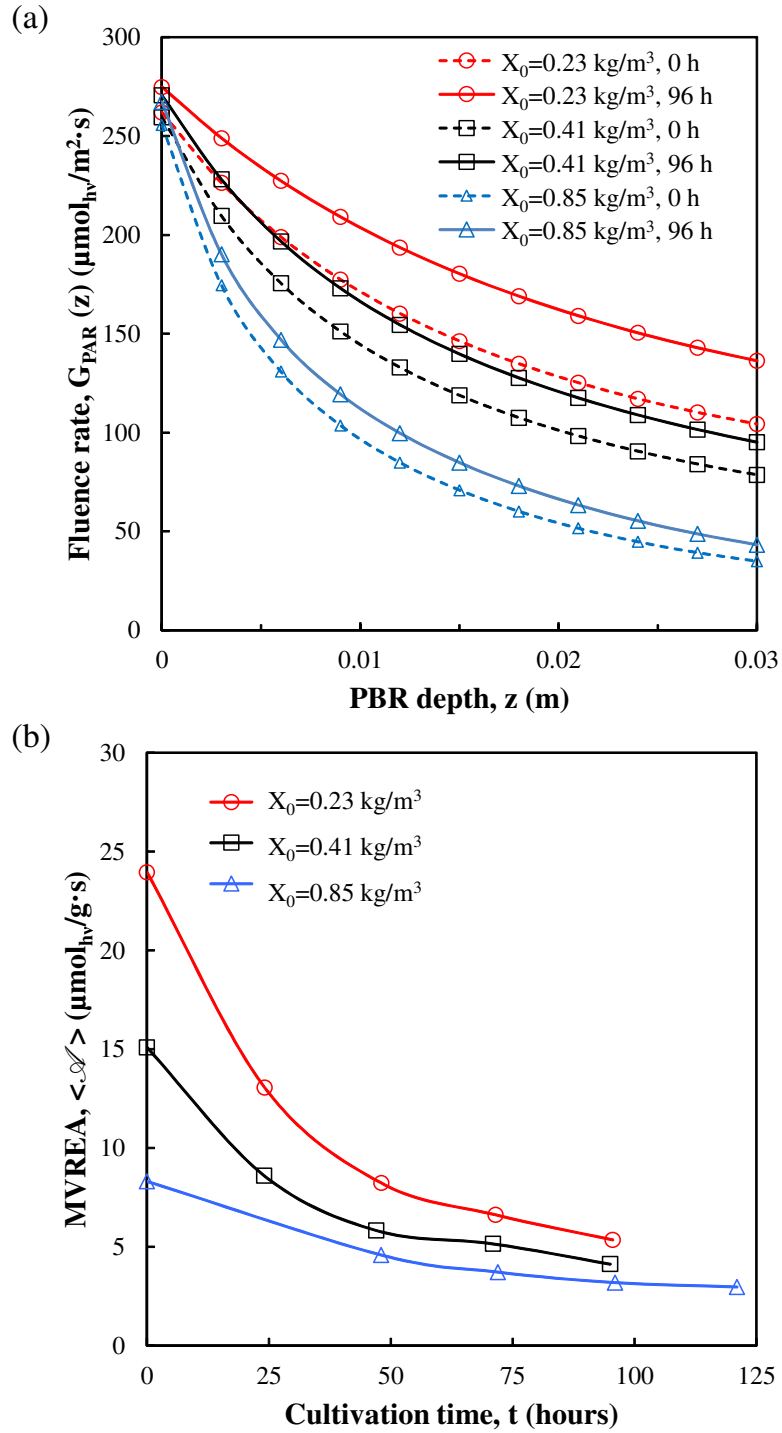
Figure 5.3: (a) Fluence rate $G_{PAR}(z)$ in the PBR at the start of the cultivation (0 hours) and after 96 hours and (b) temporal evolution of MVREA $\langle \mathscr{A} \rangle$ for sudden starvation experiments with initial biomass concentration X_0 equal to 0.23, 0.41, and 0.85 kg/m³.

measurements at discrete time t_i according to Equation (5.6). Similarly, the average daily MVREA was defined as $\langle\bar{\mathscr{A}}\rangle(t_i) = [\langle\mathscr{A}\rangle(t_i) + \langle\mathscr{A}\rangle(t_{i-1})]/2$ where $t_i - t_{i-1} = 24$ hours. Figure 5.4 shows the daily average areal TG-FA production rate $\bar{R}$ versus the daily average MVREA $\langle\bar{\mathscr{A}}\rangle$ for the sudden starvation experiments with three different initial concentrations X_0. For each experiment, the maximum daily productivity corresponded to the maximum MVREA $\langle\bar{\mathscr{A}}\rangle$ occurring on the first day of cultivation. Interestingly, data for the different experiments were consistent with one another. A parabolic relationship between TG-FA productivity $\bar{R}$ and daily average MVREA $\langle\bar{\mathscr{A}}\rangle$ was fitted to the experimental data for convenience and for a lack of a better model. The peak productivity of 4.6 g/m²·day was observed for MVREA equal to 13 $\mu\text{mol}_{h\nu}$/g·s.

This relationship indicates that nitrogen starvation alone does not guarantee large TG-FA production rate. The TG-FA biosynthesis kinetics appears to be limited by the photon absorption rate represented by MVREA $\langle\bar{\mathscr{A}}\rangle$. This is analogous to microalgae grown under optimal growth conditions (i.e., without nutrient deprivation) when biomass productivity is only limited by light. Increasing MVREA per unit mass of microalgae can be achieved by reducing the biomass concentration. However, below a certain optimum value, the biomass productivity decreases and the light incident on the PBR is not fully absorbed [74, 75]. In this so-called kinetic regime, biomass productivity is limited by the biosynthesis rate of the microalgae. Similarly, increasing the daily average MVREA beyond its optimal value resulted in a decrease in the daily TG-FA productivity $\bar{R}$. However, due to the reduction in pigment content and in absorption cross-section, it was not possible to achieve complete light absorption in the PBR during nitrogen starvation. Here, the process was biologically limited by the maximum TG-FA accumulation allowed in cells. For example, increasing daily average MVREA $\langle\bar{\mathscr{A}}\rangle$ on the first day of cultivation from 15 to 24 $\mu\text{mol}_{h\nu}$/g·s was achieved by lowering the initial biomass concentration X_0 from 0.41 to 0.23 kg/m³. Both experiments yielded cells with 31 dry wt.% TG-FA concentration after 24 hours of cultivation. However, the corresponding TG-FA concentration in the PBR was 0.21 and 0.12 kg/m³, respectively. Thus, increasing MVREA $\langle\bar{\mathscr{A}}\rangle$ did not affect the TG-FA concentration per cell but resulted
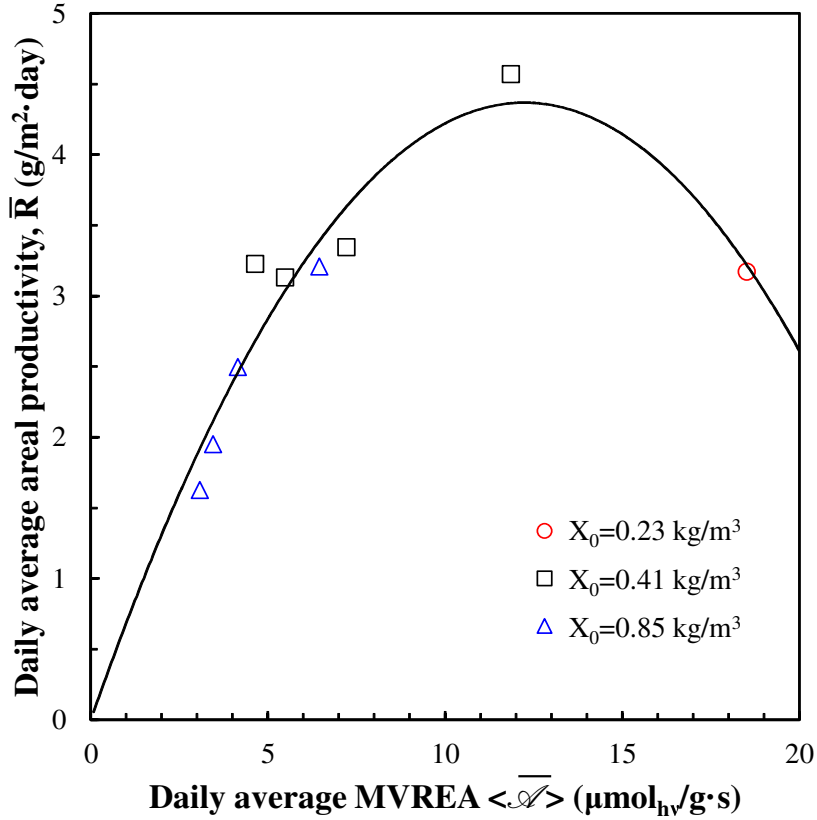
Figure 5.4: Daily average areal TG-FA productivity $\bar{R}$ (in g/m$^2\cdot$day) versus daily average MVREA $\langle\bar{\mathscr{A}}\rangle$ for sudden starvation experiments with incident PDF of 250 μmol$_{h\nu}$/m$^2\cdot$s and initial biomass concentrations X_0 equal to 0.23, 0.41, and 0.85 kg/m^3.

in a smaller PBR daily TG-FA productivity due to the smaller biomass concentration.

Furthermore, there was a large difference in the temporal evolution of biomass concentration for experiments with initial biomass concentration X_0 of 0.41 and 0.85 kg/m^3 for the duration of the batch culture. By contrast, both experiments featured a similar TG-FA concentration after 24 and 48 hours of cultivation. However, the daily TG-FA productivity of the PBR with X_0=0.41 kg/m^3 during the first 24 hours of cultivation was much larger than that of the PBR with X_0=0.85 kg/m^3 due to its lower initial TG-FA concentration. On the other hand, between 24 and 48 hours both experiments featured a similar TG-FA concentration and therefore a similar daily TG-FA productivity. It is interesting to note

that they both featured similar values of daily average MVREA $\langle \bar{\mathscr{A}} \rangle$. This was illustrated in Figure 5.4 for daily average MVREA $\langle \bar{\mathscr{A}} \rangle$ values of 5.5-7.5 $\mu\mathrm{mol}_{h\nu}/\mathrm{g}\cdot\mathrm{s}$ where data from both experiments were clustered. This exemplifies the value of our proposed method of correlating the MVREA with the TG-FA productivity. Despite the differing biomass and pigment concentrations, cultures with comparable values in MVREA featured similar TG-FA productivities.

Finally, During sudden starvation batch cultivations the TG-FA productivity $R(t)$ decreased due to the decrease in MVREA $\langle \mathscr{A} \rangle$ (Figure 5.3b). Thus, in batch cultivation it is not possible to maintain a constant TG-FA productivity. Instead, the TG-FA productivity can be optimized through the initial value of MVREA denoted by $\langle \mathscr{A}_0 \rangle$. The latter can be adjusted by changing the initial biomass concentration according to the incident PFD and PBR thickness.

5.4.8 TG-FA accumulation

Here, the data reported by Van Vooren *et al.* [39] was used in addition to those reported in this study to elucidate the relationship between initial value of MVREA $\langle \mathscr{A}_0 \rangle$ and TG-FA cell content. The authors performed a total of fourteen progressive and sudden starvation experiments using the same microalgae species, strain, and PBR as those used in the present study. The pigment and biomass concentrations were analyzed using the same protocols. In addition, the authors reported the pigment concentrations and the TG-FA concentrations in the cells for a wide range of nitrogen starvation experiments. However, they did not measure the radiation characteristics of *N. oculata*. Therefore, in order to extend the present light transfer analysis to experiments reported by Van Vooren *et al.* [39], Equation (5.19) was used to estimate the average mass absorption cross-section of cultures based on the reported pigment concentrations.

5.4.8.1 Sudden nitrogen starvation

Van Vooren *et al.* [39] performed a total of four sudden starvation experiments in a PBR exposed to 250 $\mu mol_{h\nu}/m^2 \cdot s$. The initial biomass concentrations were 0.23, 0.41, 0.65, and 0.75 kg/m^3. The four experiments yielded cultures with a TG-FA concentration of 44, 45, 14, and 13 dry wt.%, after 96 hours respectively. Figure 5.5 shows the TG-FA cell content (in wt.%) after 96 hours as a function of the initial MVREA $\langle \mathscr{A}_0 \rangle$ for sudden starvation experiments performed in the present study and those reported by Van Vooren *et al.* [39].
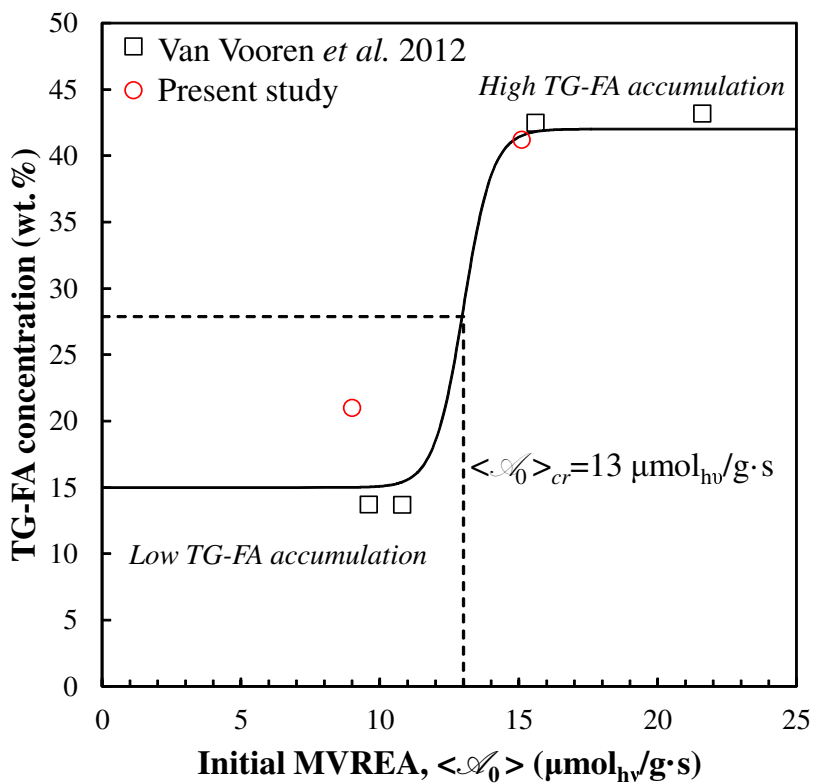
Figure 5.5: TG-FA concentration (in wt.%) after 96 hours of sudden nitrogen starvation as a function of initial MVREA $\langle \mathscr{A}_0 \rangle$. A critical value $\langle \mathscr{A}_0 \rangle_{cr}$ of 13 $\mu mol_{h\nu}/g \cdot s$ was necessary to trigger large TG-FA accumulation in cells.

It suggests that there exists a critical initial MVREA $\langle \mathscr{A}_0 \rangle_{cr}$ beyond which the cells accumulated large amounts of TG-FA. Here, $\langle \mathscr{A}_0 \rangle_{cr}$ was estimated to be 13 $\mu mol_{h\nu}/g \cdot s$. Note

that it is generally not possible to exceed this critical initial MVREA $\langle \mathscr{A}_0 \rangle_{cr}$ on the second day of sudden starvation cultivation. Indeed, a sharp decrease in $\langle \mathscr{A} \rangle$ was observed in the first 24 hours of cultivation (Figure 5.3b) due to the rapid decrease in pigment concentrations (Figures 5.1b and 5.1c) and increase in biomass concentration. Therefore, in order to produce cells with large TG-FA content in a batch culture, the initial mass concentration X_0 of the batch culture must be adjusted carefully in order to achieve values of $\langle \mathscr{A}_0 \rangle$ that exceed the critical MVREA $\langle \mathscr{A}_0 \rangle_{cr} = 13~\mu\mathrm{mol}_{h\nu}/\mathrm{g\cdot s}$.

The critical MVREA under nitrogen starvation could correspond to conditions when the cells' TG-FA synthesis rate increases with respect to the synthesis rate of carbohydrate, protein, etc. In fact, the TG-FA synthesis pathway is activated under nitrogen starvation to act as an electron sink and prevent creation of excess free-radicals in the photosynthetic electron transport chain [149]. In addition, it takes twice as much light energy to produce TG-FA as it does to produce protein or carbohydrate of equal mass [149]. However, it remains unclear how cells distribute the absorbed energy during nitrogen starvation [149]. By setting the initial MVREA in excess of $\langle \mathscr{A}_0 \rangle_{cr}$ in batch experiments, the average MVREA was sufficient to ensure the average production rate of TG-FA was at least 40-45% of the biomass production rate for the duration of the experiment and produced cells with 40-45 dry wt.% TG-FA.

The similarity between the critical initial MVREA $\langle \mathscr{A}_0 \rangle_{cr}$ for maximum TG-FA cell content and the daily MVREA $\langle \bar{\mathscr{A}} \rangle$ corresponding to peak daily average areal productivity $\bar{R}$ is interesting but unsurprising. It can be explained by the fact that the largest increase in TG-FA concentration in cells and maximum daily productivity for each cultivation occurred in the first 24 hours of nitrogen starvation. Since, the daily average MVREA $\langle \bar{\mathscr{A}} \rangle$ for the first 24 hours of cultivation corresponded approximately to the initial MVREA $\langle \mathscr{A}_0 \rangle$, the optimum values for both were equal.

5.4.8.2 Progressive starvation

Van Vooren *et al.* [39] performed a total of 10 progressive starvation experiments as summarized in Table 2 of their manuscript. Experiments no. 9 and 10 used a modified Conway medium with an initial NO_3^- concentration of 0.92 and 1.65 mM, respectively. In both cases, the initial biomass concentration was 0.02 kg/m^3 and the microorganisms were cultivated in a 150 L PBR, 5 cm in thickness, exposed to a PFD of 222 μmol$_{h\nu}$/m^2·s. Note that the biomass concentration at the culture's onset of nitrogen starvation was not reported in experiments no. 1 to 8. Therefore, it was not possible to estimate the radiation characteristics and the MVREA $\langle \mathscr{A} \rangle$ for those experiments.

Figures 5.6a and 5.6b respectively present the temporal evolution of the MVREA $\langle \mathscr{A} \rangle$ and of the cellular TG-FA concentration during the course of experiments no. 9 and 10. The approximate time at which nitrogen starvation began was estimated from elemental analysis assuming that *N. oculata* was composed of 10 dry wt.% nitrogen in nutrient replete conditions [75]. Nitrogen starvation occurred later in experiment no. 10 than in experiment no. 9 because of the larger initial nitrate concentration. For both experiments, the extrapolated MVREA $\langle \mathscr{A}_0 \rangle$ at the onset of the nitrogen starvation fell between 12 and 15 μmol$_{h\nu}$/g·s. This corresponded, approximately, to the value of the critical MVREA $\langle \mathscr{A}_0 \rangle_{cr}$ observed in the sudden starvation experiments. The intracellular TG-FA concentration increased sharply after nitrogen starvation began and reached 28 dry wt.%. It is remarkable that both progressive and sudden starvation experiments had a similar MVREA at the onset of nitrogen starvation since it is not possible to control and set MVREA at the onset of nitrogen starvation $\langle \mathscr{A}_0 \rangle$ for progressive nitrogen starvation experiments. This provided further evidence in the relevance of MVREA $\langle \mathscr{A}_0 \rangle$ in predicting the TG-FA accumulation in cells.

Along with nitrogen starvation, the term "light stress" has often been used in the literature as a necessary condition for large TG-FA productivity [149]. However, the concept of "light stress" has remained qualitative. The present study addressed this issue by defining

(a)

(b)
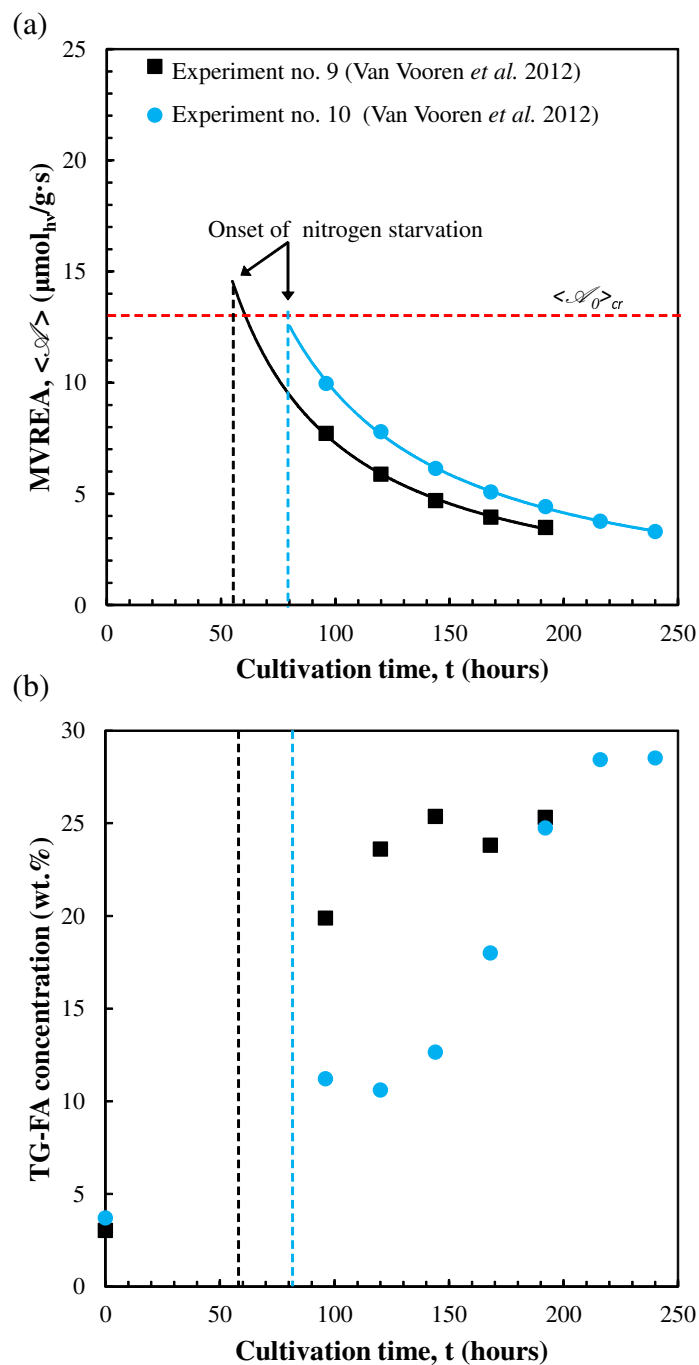
Figure 5.6:   Temporal evolution of (a) MVREA $\langle \mathscr{A} \rangle$ and (b) cellular TG-FA concentration for progressive starvation batch cultures grown in a 150 L PBR, 5 cm in thickness, in modified Conway medium with an initial NO_3^- concentration of 0.93 mM (experiment no. 9) and 1.65 mM (experiment no. 10) by Van Vooren *et al.* [39]. The dashed lines indicate the estimated time at which nitrogen starvation began.

the physical variable to quantify "light stress", namely the specific volumetric rate of energy absorption (MVREA). It also reported the critical value of the MVREA necessary for large TG-FA productivity.

The maximum batch averaged areal TG-FA and biomass productivities achieved were respectively 2.9 and 7.5 g/m²·day, obtained for the experiment with initial biomass concentration X_0=0.41 kg/m³. The associated volumetric TG-FA and biomass productivities were 0.1 and 0.25 kg/m³·day, respectively. These productivities could be significantly increased by optimizing the MVREA in the PBR using the proposed relation between TG-FA productivity R and MVREA $\langle \mathscr{A} \rangle$. The latter can also be used to predict the TG-FA productivity of PBRs of all scales and optimize them as long as rigorous radiation transfer analysis is performed to estimate MVREA $\langle \mathscr{A} \rangle$. Pruvost and Cornet [74] validated this approach by optimizing and predicting both biomass concentration and productivity of microorganisms in PBRs scaling from 1 to 150 L.

Future studies should focus on validating the present observations and quantitative analysis for other microalgae species and developing novel methods of optimizing the instantaneous TG-FA production rate R with respect to MVREA $\langle \mathscr{A} \rangle$. The latter depends on biomass concentration, cell pigment content, and incident PFD. These parameters are dynamic and interdependent. They will be difficult to control, especially in a batch cultivation exposed to solar radiation. Therefore, while an optimum value of MVREA exists that maximizes TG-FA productivity, it may not be trivial to control and optimize MVREA $\langle \mathscr{A} \rangle$. Moreover, the optimum and critical MVREA may depend on culture conditions such as medium salinity, pH, or temperature. In the present study, the microalgae were cultivated under conditions leading to maximal biomass and TG-FA productivity reported by Van vooren *et al.* [39] and Pruvost *et al.* [151]. The methodology presented here could be extended to investigate the effects of cultivation conditions on the optimal and critical MVREA.

5.5   Chapter summary

This study demonstrated the existence of a relation between the mean volumetric rate of energy absorption (MVREA) per unit mass of microalgae and the daily TG-FA productivity of *N. oculata* cultures. It indicated that TG-FA synthesis in the PBR was physically limited by the photon absorption rate per unit mass of microalgae. The TG-FA productivity reached a maximum of 4.5 g/m^2·day corresponding to MVREA equal to 13 μmol$_{h\nu}$/g·s. In addition, a critical initial MVREA $\langle \mathscr{A}_0 \rangle_{cr}$ in excess of also 13 μmol$_{h\nu}$/g·s was required to trigger a large accumulation of TG-FA in cells in both sudden and progressive nitrogen starvation.

CHAPTER 6

Summary and Recommendations

6.1   Summary

The two objective of the study were (1) to study the interaction between light and photosynthetic microoranisms and (2) to optimize light transfer conditions in PBRs to maximize microalgal biomass and lipid production.

The first objective was achieved by measuring the absorption and scattering cross-sections and retrieving the optical properties of *N. oculata* for cells grown under white light and red LEDs with illuminance ranging from 2,000 to 10,000 lux. The microalgae average equivalent diameter ranged from 2.52 to 2.63 μm. Their cross-sections and optical constants were statically identical over most of the PAR region. *N. oculata* grown in 2 vol.% CO_2 injected PBRs featured lower pigment concentration and significantly smaller absorption cross-section and absorption index due to nutrient limited growth conditions. By contrast, the refraction index was identical for all conditions considered, falling between 1.365 and 1.376. Moreover, this study demonstrated that the radiation characteristics of fractal microalgae aggregates and colonies consisting of optically soft spherical monomers can be approximated as coated spheres with equivalent volume and average projected area. Very good agreement in aggregate radiation characteristics was found between the superposition T-matrix predictions and the volume and average projected area equivalent coated sphere approximation for size parameters between 0.01 and 20 and for aggregates of fractal dimension ranging from 2.0 to 3.0. On the other hand, the Rayleigh-Debye-Gans approximation suffered from excessive errors for size parameters larger than 1, for N_s larger than 100, and for strongly absorbing monomers. In addition, the use of Henyey-Greenstein approximate phase function estimated

using the asymmetry factor for the equivalent coated sphere yielded acceptable predictions for all monomer size parameters and numbers considered. Finally, the equivalent coated spheres featured scattering matrix element ratios significantly different from those of the aggregates they were approximating. Overall, these results could be used for predicting the radiation characteristics of fractal aggregates or retrieving their optical properties from absorption and scattering cross-section measurements.

The second objective was met by developing a versatile and general control methodology for maintaining maximum microorganism growth rate during a batch cultivation. It consisted of (i) a model-free optimal search based on Brent's method and (ii) a feed-forward inversion control of incident irradiance based on continuous mass concentration measurements. For demonstration purposes, marine microalgae *N. oculata* was grown in batch mode in 1 cm thick flat-plate PBRs exposed to red light from both sides. The optimal search successfully estimated the optimum average fluence rate as 236 $\mu mol_{h\nu}/m^2 \cdot s$ corresponding to a specific growth rate of 0.06 h^{-1}. The microalgae exposed to controlled incident irradiance had a very short lag time and reached saturation mass concentration of 2.25 kg/m^3. The method demonstrated in this study can be used for any microorganism species and PBR design, as well as for operating parameters other than incident irradiance such as the pH and the medium composition. Finally, this study demonstrated the existence of a relation between the mean volumetric rate of energy absorption (MVREA) per unit mass of microalgae and the daily TG-FA productivity of *N. oculata* cultures. It indicated that TG-FA synthesis in the PBR was physically limited by the photon absorption rate per unit mass of microalgae. The TG-FA productivity reached a maximum of 4.5 $g/m^2 \cdot day$ corresponding to MVREA equal to 13 $\mu mol_{h\nu}/g \cdot s$. In addition, a critical initial MVREA $<\mathscr{A}_0>_{cr}$ in excess of also 13 $\mu mol_{h\nu}/g \cdot s$ was required to trigger a large accumulation of TG-FA in cells in both sudden and progressive nitrogen starvation.

6.2 Recommendations for future research

6.2.1 Radiation characteristics determination

The model predicted absorption cross-sections in Chapter 2 (Figure 2.7) was in poor agreement with the experimental measurements. This indicates that Equation (2.1) proposed by Pottier *et al.* [41] predicting absorption index k_λ may be inaccurate and new model relating pigment dry mass concentration to absorption index may be needed. In addition, the specific mass absorption cross-sections of various photosynthetic pigments reported by Bidigare *et al.* [42] and shown in Figure 2.1 may be incomplete or inaccurate. For example, it only provides the specific mass absorption cross-sections for one type of carotenoid. However, during nitrogen starvation, the microalgae cells produce several types of carotenoids such as β-carotene [33], violaxanthin [33], and vaucherxanthin [33] whose absorption spectra are not available and must be measured.

Chapter 2 presented the effect of illuminance on the average absorption and scattering cross-sections of the *N. oculata* grown in batch mode. These effects must also be investigated in continuous cultures as it is an important process in industrial microalgae production [74]. Takache *et al.* [75] investigated pigment adaptation and biomass productivity of the microalgae *C. reinhardtii* cultivated in continuous mode in 1.4 L torus shaped flat-plate PBR exposed to while LEDs with PFD ranging from 50 to 1000 $\mu\mathrm{mol}_{h\nu}/\mathrm{m}^2{\cdot}\mathrm{s}$. The authors also investigated the effects of culture dilution rate on the pigment concentration and the steady-state biomass concentration. A similar study could be performed for *N. oculata* to investigate the effects of pigment concentration, biomass productivity as well as absorption and scattering cross-sections of the microalgae.

6.2.2 PBR and process design improvements

The control scheme and optimum identification method developed in Chapter 4 can be applied to determine the optimum CO_2 concentration and continuously adjusting the CO_2 injection rate. Further improvements in biomass productivity may also require controlling

the dissolved concentrations of individual nutrients in the growth medium to avoid inhibition or limitation by one or several nutrient ingredients.

The relation between MVREA and lipid productivity reported in Chapter 5 must be validated for other microalgae species using the quantitative analysis presented. Moreover, the optimum and critical MVREA may depend on culture conditions such as medium salinity, pH, or temperature. In the present study, the microalgae were cultivated under conditions leading to maximal biomass and TG-FA productivity. However, the effects of cultivation conditions on the optimal and critical MVREA must be investigated.

Lee *et al.* [116] numerically simulated light transfer in PBRs exposed to solar radiation and predicted biomass productivity for a given initial biomass concentration of microalgae. A similar study could be performed to predict lipid productivity of microalgae exposed to solar radiation using the relationship between MVREA and the TG-FA productivity presented in Chapter 5. Such a study can be used to determine the optimum initial biomass concentration of the sudden starvation cultivation.

Moreover, the effect of periods of non-illumination of cells on their biochemical composition must be investigated. The loss of lipids, accumulated by the microalgae, during the night is an important consideration for large-scale outdoor microalgae cultivation. Indeed, cell composition changes when the microalgae are kept in a dark environment. Then, they consume their lipid reserves and use them as an energy source for respiration [68]. The lipid consumption rate by the microalgae during dark periods must be quantified in order to assess the productivity loss during the night and optimal harvesting time of cultures grown in batch mode.

Novel methods of optimizing the instantaneous TG-FA production rate R with respect to MVREA $<\mathscr{A}>$ must also be developed. For example, the control scheme presented in Chapter 4 can be used for controlling the incident irradiance on PBRs used for cultivating nitrogen starved *N. oculata* to increase TG-FA productivity in indoor PBRs exposed to artificial light. However, due to significant changes in cell pigment concentration during nitrogen starvation, the radiation transfer model must take into account the fact that

133

absorption and scattering cross-sections of the cells change during the batch process. This requires a model predicting the cell pigment concentration during nitrogen starvation. Then, the semi-empirical model [Equation (5.19)] developed in Chapter 5 can be used to estimate the absorption cross-section using the pigment concentration predictions.

APPENDIX A

Absorption and scattering by fractal aggregates and by their equivalent coated spheres (Supplementary Material)

A.1 Scattering matrix element ratios

Figures A.1 shows the scattering matrix element ratios (a) $F_{21}(\Theta)/F_{11}(\Theta)$, (b) $F_{22}(\Theta)/F_{11}(\Theta)$, (c) $F_{33}(\Theta)/F_{11}(\Theta)$, (d) $F_{34}(\Theta)/F_{11}(\Theta)$, and (e) $F_{44}(\Theta)/F_{11}(\Theta)$ predicted by the superposition T-matrix method as a function of scattering angle Θ for randomly oriented aggregates of fractal dimension D_f of 2.25, relative complex index or refraction $m = 1.0165 + i0.003$, and consisting of 9 monomers with size parameter χ_s of 2.5, 5.0, or 10. It illustrates that the number of resonance angles increased with increasing size parameter. For example, all the scattering matrix element ratios had 1, 2, or 6 resonance peaks for aggregates composed of 9 monomers with size parameter 2.5, 5, or 10, respectively.

Figures A.2 shows the scattering matrix element ratios (a) $F_{21}(\Theta)/F_{11}(\Theta)$, (b) $F_{22}(\Theta)/F_{11}(\Theta)$, (c) $F_{33}(\Theta)/F_{11}(\Theta)$, (d) $F_{34}(\Theta)/F_{11}(\Theta)$, and (e) $F_{44}(\Theta)/F_{11}(\Theta)$ predicted by the superposition T-matrix method as a function of scattering angle Θ for randomly oriented aggregates of fractal dimension D_f of 2.25 and consisting 9, 36, and 100 monomers of size parameter χ_s=2.5 and $m = 1.0165 + i0.003$. All scattering matrix element ratios featured a resonance peak at the scattering angle Θ of 125°. Here also, no clear relationship was observed between the magnitude of the resonance peak and the number of monomers N_s in the aggregate.
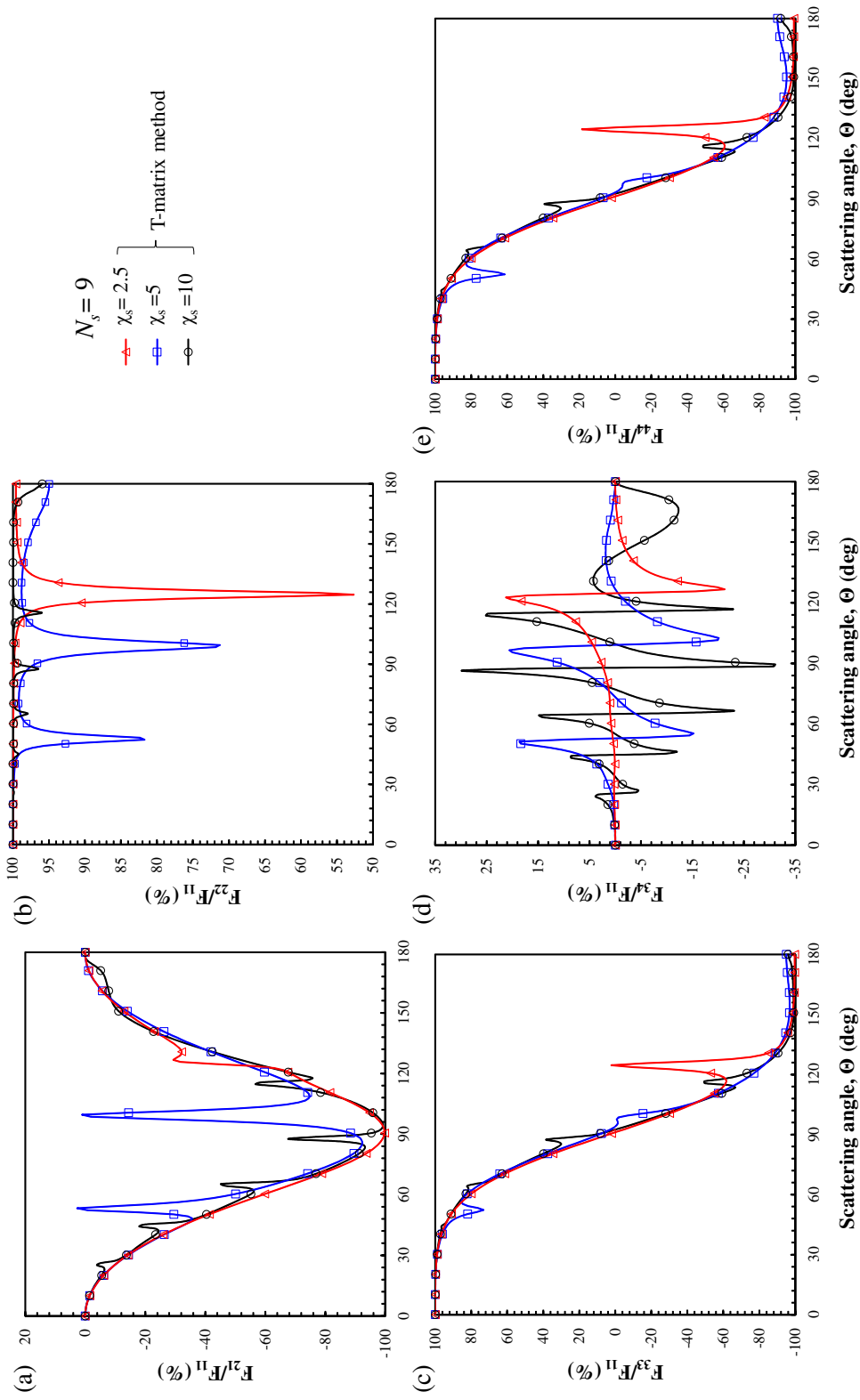
Figure A.1: Scattering matrix element ratios (a) $F_{21}(\Theta)/F_{11}(\Theta)$, (b) $F_{22}(\Theta)/F_{11}(\Theta)$, (c) $F_{33}(\Theta)/F_{11}(\Theta)$, (d) $F_{34}(\Theta)/F_{11}(\Theta)$, and (d) $F_{44}(\Theta)/F_{11}(\Theta)$ of randomly oriented aggregates with fractal dimension $D_f = 2.25$ containing 9 monodisperse monomers with size parameter $\chi_s = 2.5$, 5, and 10 and $m = 1.0165 + i0.003$ predicted using the superposition T-matrix method.

136
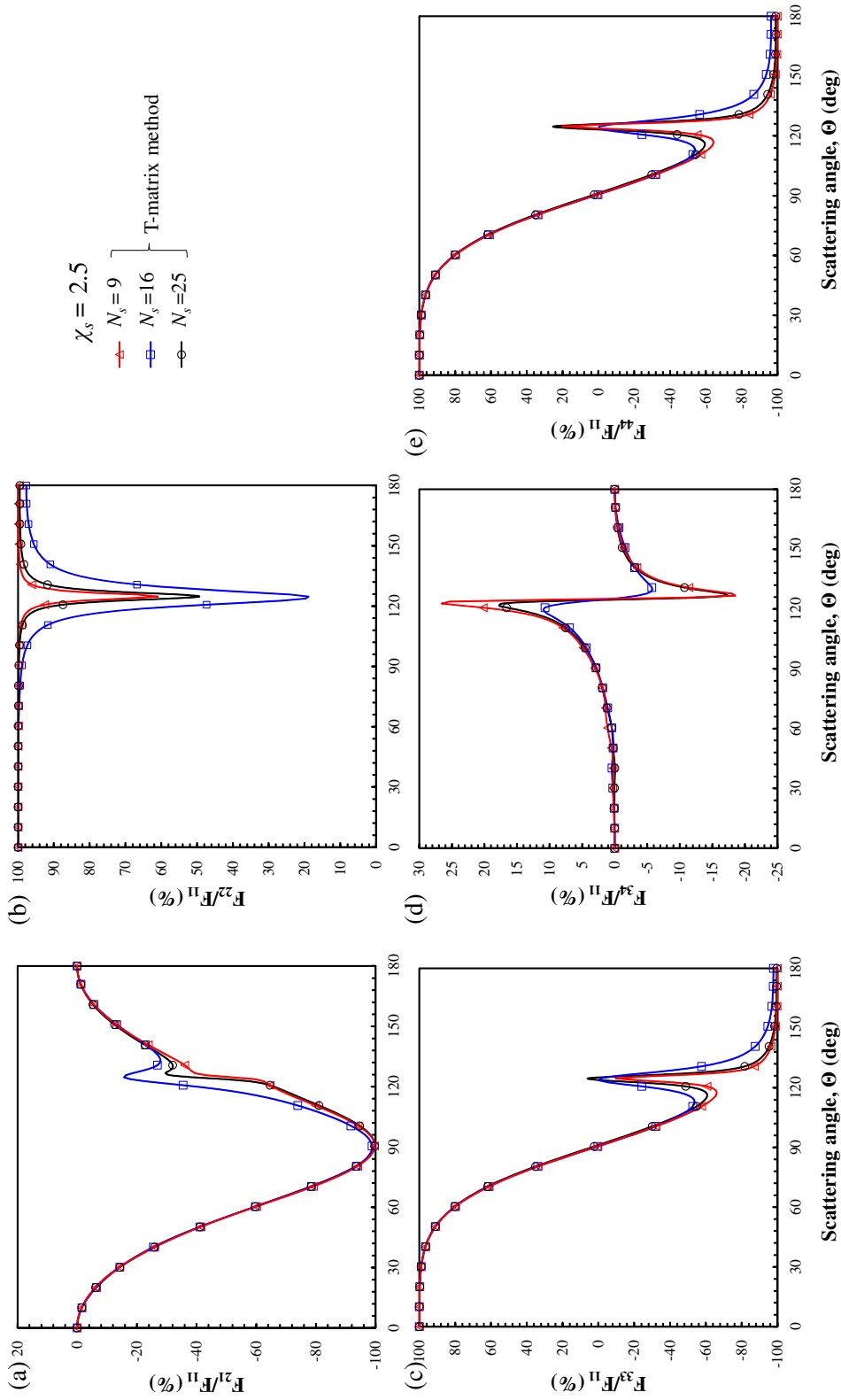
Figure A.2: Scattering matrix element ratios (a) $F_{21}(\Theta)/F_{11}(\Theta)$, (b) $F_{22}(\Theta)/F_{11}(\Theta)$, (c) $F_{33}(\Theta)/F_{11}(\Theta)$, (d) $F_{34}(\Theta)/F_{11}(\Theta)$, and (d) $F_{44}(\Theta)/F_{11}(\Theta)$ of randomly oriented aggregates with fractal dimension $D_f = 2.25$ containing $N_s = 9$, 16, and 25 monodisperse monomers with size parameter $\chi_s = 2.5$ and $m = 1.0165 + i0.003$ predicted using the superposition T-matrix method.

137

APPENDIX B

Influence of Light Absorption Rate by *Nannochloropsis oculata* on Triglyceride Production During Nitrogen Starvation (Supplementary Material)

B.1   Validation of spectrophotometer

Figures B.1a and B.1b compare the experimentally measured scattering cross-section $C_{sca,\lambda}$ of mono-disperse latex spheres of 2.02 and 4.5 μm diameter, respectively, with Lorenz-Mie theory predictions using the complex index of refraction of latex reported by [46]. The good agreement between theoretical and experimental results successfully validated the experimental setup and data analysis.

B.2   Radiation characteristics of *N. oculata*

Figures B.2a and B.2b show the measured average mass absorption and scattering cross-sections in the spectral region from 350 to 750 nm for *N. oculata* during sudden nitrogen starvation for the experiments with an initial biomass concentration X_0 of 0.41 kg/m^3. Similarly, Figures B.2c and B.2d, respectively, show the absorption and scattering cross-sections for the experiment with initial biomass concentration X_0 of 0.85 kg/m^3.
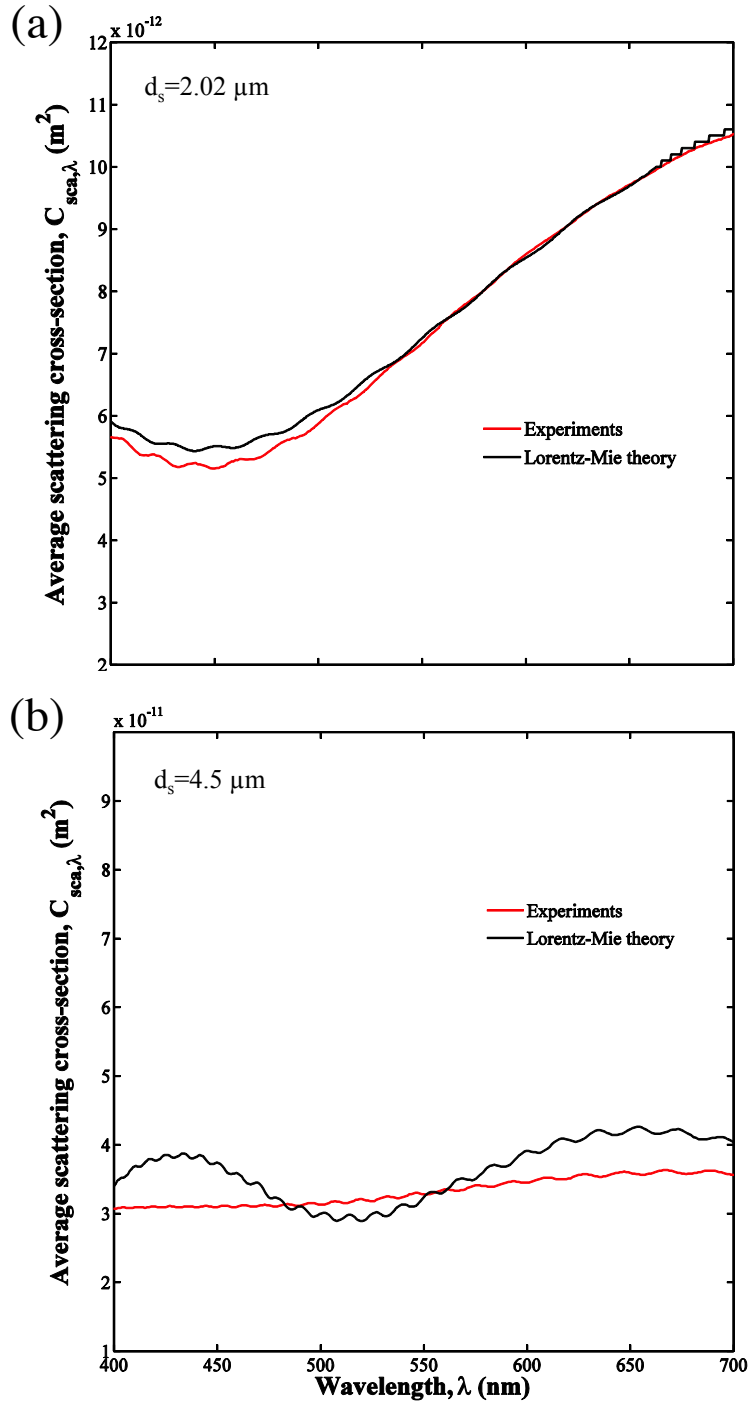
Figure B.1: Experimental measurement and Lorenz-Mie theory predictions of scattering cross-section $C_{sca,\lambda}$ of polystyrene microspheres between 400 and 700 nm with diameters d_s equal to (a) 2.02 μm and (b) 4.5 μm. Here, $C_{abs,\lambda}$=0 m^2.

139
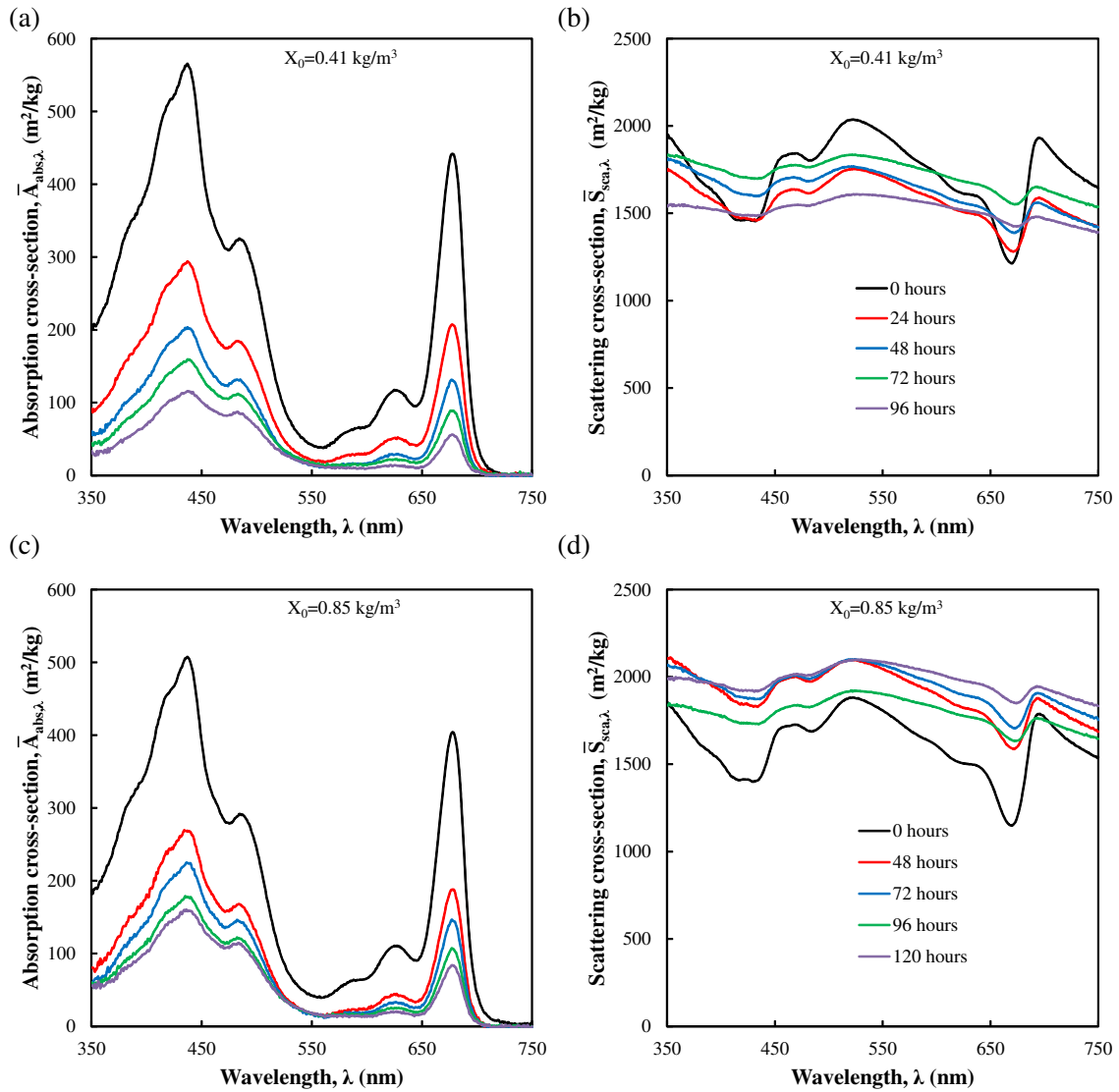
Figure B.2: Average spectral mass (a) Absorption and (b) scattering cross-sections of *N. oculata* with $X_0 = 0.41$ kg/m^3 after 0, 24, 48, 72, and 96 hours of cultivation during sudden nitrogen starvation of batch culture exposed to 250 μmol$_{h\nu}$/m^2·s. Average spectral mass (c) absorption and (d) scattering cross-sections of *N. oculata* with $X_0 = 0.85$ kg/m^3 after 0, 48, 72, 96 and 120 hours of cultivation.

APPENDIX C

Matlab scripts

C.1   LTA.m

```
clear all
close all

load LED_SPECTRUM.txt

load RC.txt

%assign absorption and scattering cross-section m2/kg
A=RC(:,2);
S=RC(:,3);

%incident irradiance umol/m2s
PFD=250;

%backward scattering ratio
b=0.002;

%biomass concentration g/l
X=1;
```

```
%wavelength nm
W=(400:700);


%PBR Thickness m
L=0.03;


%two flux function inputs [Wavelength, normalized LED emission intensity, PFD,
%absorption cross-section, scattering cross-section, backward scattering
%ratio, biomass concentration, PBR thickness]
[z,G(:,:)]=twoflux(LED_SPECTRUM(:,1),LED_SPECTRUM(:,2),PFD,A(:),S(:),b,X,L);


for k=1:301
    R(:,k)=G(:,k).*A(k)*X;
end


for j=1:length(z)
    VREA(j)=trapz(W,R(j,:))./300;
    G_PAR(j)=trapz(W,G(j,:));
end


MVREA=trapz(z,VREA(:))./0.03;
```

C.2   twoflux.m

```
function [z,G]=twoflux(W,N,Gin,A,S,b,C,L)


%alpha
a=sqrt(A./(A+2*b.*S));
%delta
```

```matlab
d=C*sqrt(A.*(A+2*b.*S));
%backwall reflectivity
Rs=0.20;



z=(0:L/100:L);


p=(1+a);
m=(1-a);
lp=exp(d.*L);
lm=exp(-d.*L);


for i=1:length(W)

    %G(:,i)=Gin*N(i).*exp(-d(i).*z);


    G(:,i)=2*Gin*N(i).*((Rs*(1+a(i))-(1-a(i))).*exp(d(i).*(z-L))+((1+a(i))-...
Rs*(1-a(i))).*exp(d(i).*(L-z)))/((1+a(i))^2*exp(d(i)*L)-(1-a(i))^2*exp(-d(i)*L)...
+Rs*(1-a(i)^2)*(exp(-d(i)*L)-exp(d(i)*L)));
end
```

C.3   LEDSPECTRUM.txt

400 0.000141217931182256

401 0.000144144868242441

402 0.000147071805302627

403 0.000150773282195445

404 0.000154850663193693

405 0.000158928044191941

406 0.000163903272635106

407 0.000170623953187500

408 0.000177344633739895

409 0.000184097376938901

410 0.000196538116473333

411 0.000208978856007765

412 0.000221419595542197

413 0.000240349095596392

414 0.000262459074325937

415 0.000284569053055482

416 0.000311926703174568

417 0.000349650954831024

418 0.000387375206487481

419 0.000425115440278865

420 0.000487656671636745

421 0.000550197902994624

422 0.000612739134352503

423 0.000697426964867554

424 0.000793282850165662

425 0.000889138735463770

426 0.000999483647945937

427 0.00113944988039983

428 0.00127941611285373

429 0.00141938234530763

430 0.00161645517509276

431 0.00181400246124416

432 0.00201154974739555

433 0.00226516399747076

434 0.00254835606768970

435 0.00283154813790864

436 0.00315436128098486

437 0.00356248618146836

438 0.00397061108195187

439 0.00437873598243537

440 0.00491025882903744

441 0.00544439618200363

442 0.00597853353496982

443 0.00651556651721269

444 0.00705422126496312

445 0.00759287601271355

446 0.00806381516907252

447 0.00837852803375174

448 0.00869324089843095

449 0.00900795376311017

450 0.00895859135302950

451 0.00889540446296073

452 0.00883221757289196

453 0.00858451944471564

454 0.00822569761014905

455 0.00786687577558247

456 0.00748301752379114

457 0.00703619239768091

458 0.00658936727157068

459 0.00614254214546045

460 0.00576578354533103

461 0.00539313780649304

462 0.00502049206765504

463 0.00469976746710312

464 0.00441303933999002

465 0.00412631121287693

466 0.00385563974118395

467 0.00362978330469680

468 0.00340392686820965

469 0.00317807043172250

470 0.00299602107479525

471 0.00281762815533662

472 0.00263923523587800

473 0.00248755689427582

474 0.00235507498262820

475 0.00222259307098058

476 0.00210027579382205

477 0.00201005276398497

478 0.00191982973414789

479 0.00182960670431080

480 0.00176983563491569

481 0.00171348803322696

482 0.00165714043153823

483 0.00161477428276378

484 0.00158352309912981

485 0.00155227191549584

486 0.00152649015926239

487 0.00152067184419612

488 0.00151485352912985

489 0.00150903521406357

490 0.00152712945244509

491 0.00154870920128132

492 0.00157028895011754

493 0.00160787839945314

494 0.00165964759769850

495 0.00171141679594386

496 0.00176802446291560

497 0.00184557956047764

498 0.00192313465803969

499 0.00200068975560174

500 0.00209575241261842

501 0.00219403165111509

502 0.00229231088961175

503 0.00239732617499662

504 0.00250902997626274

505 0.00262073377752886

506 0.00273366053452051

507 0.00285307575146289

508 0.00297249096840528

509 0.00309190618534767

510 0.00321064024997361

511 0.00332921996538317

512 0.00344779968079274

513 0.00356418583958398

514 0.00367811617290279

515 0.00379204650622160

516 0.00390453337280003

517 0.00400720442594636

518 0.00410987547909269

519 0.00421254653223903

520 0.00430573287095582

521 0.00439631369214431

522 0.00448689451333280

523 0.00457109059126749

524 0.00464718305964531

525 0.00472327552802312

526 0.00479807945010524

527 0.00486085700977566

528 0.00492363456944608

529 0.00498641212911650

530 0.00503968176054248

531 0.00508982899830538

532 0.00513997623606828

533 0.00518504085581256

534 0.00522275281480877

535 0.00526046477380497

536 0.00529766365863979

537 0.00532743394471773

538 0.00535720423079568

539 0.00538697451687362

540 0.00541116510455146

541 0.00543319049410486

542 0.00545521588365826

543 0.00547397499402693

544 0.00548731872372097

545 0.00550066245341501

546 0.00551388080547061

547 0.00552330555320529

548 0.00553273030093997

549 0.00554215504867465

550 0.00554849294824225

551 0.00555342930904312

552 0.00555836566984399

553 0.00556168521600134

554 0.00556191448317180

555 0.00556214375034226

556 0.00556237301751271

557 0.00555989860406140

558 0.00555742211881546

559 0.00555494563356952

560 0.00555011969796160

561 0.00554405626997913

562 0.00553799284199666

563 0.00553090013491837

564 0.00552152494911766

565 0.00551214976331695

566 0.00550277457751623

567 0.00549069939794557

568 0.00547853100659171

569 0.00546636261523785

570 0.00545124452943583

571 0.00543433777129767

572 0.00541743101315951

573 0.00539930509700757

574 0.00537802008989971

575 0.00535673508279184

576 0.00533545007568398

577 0.00531186143784799

578 0.00528811127064316

579 0.00526436110343833

580 0.00523879234146601

581 0.00521196281445104

582 0.00518513328743607

583 0.00515697732380526

584 0.00512477261153371

585 0.00509256789926216

586 0.00506036318699060

587 0.00502699243288431

588 0.00499349652385057

589 0.00496000061481684

590 0.00492459600608843

591 0.00488768858015883

592 0.00485078115422923

593 0.00481321813852190

594 0.00477327601167317

595 0.00473333388482444

596 0.00469339175797571

597 0.00465035397206293

598 0.00460686468029773

599 0.00456337538853252

600 0.00451714172950575

601 0.00446846994304781

602 0.00441979815658986

603 0.00437090369773133

604 0.00432103820188524

605 0.00427117270603915

606 0.00422130721019305

607 0.00417002051097100

608 0.00411847053090871

609 0.00406692055084643

610 0.00401511151780651

611 0.00396304451680910

612 0.00391097751581168

613 0.00385910037938767

614 0.00380823058308867

615 0.00375736078678967

616 0.00370649099049068

617 0.00365582521250905

618 0.00360520533599467

619 0.00355458545948031

620 0.00350398211580861

621 0.00345339709691213

622 0.00340281207801565

623 0.00335211627209926

624 0.00330069502629675

625 0.00324927378049425

626 0.00319785253469174

627 0.00314869819470514

628 0.00310014314727672

629 0.00305158809984830

630 0.00300326473846985

631 0.00295522502395269

632 0.00290718530943553

633 0.00285944807130789

634 0.00281419564383027

635 0.00276894321635265

636 0.00272369078887503

637 0.00267808870014752

638 0.00263238082203330

639 0.00258667294391908

640 0.00254134532533567

641 0.00249652753909303

642 0.00245170975285039

643 0.00240683573194694

644 0.00236137153165639

645 0.00231590733136584

646 0.00227044313107529

647 0.00222652786934395

648 0.00218313699260538

649 0.00213974611586680

650 0.00209632996700701

651 0.00205287706982520

652 0.00200942417264340

653 0.00196612802291258

654 0.00192497323620591

655 0.00188381844949925

656 0.00184266366279259

657 0.00180205400812910

658 0.00176164672402218

659 0.00172123943991527

660 0.00168160828426948

661 0.00164318759201960

662 0.00160476689976972

663 0.00156649200452448

664 0.00153085077517970

665 0.00149520954583492

666 0.00145956831649014

667 0.00142633503097000

668 0.00139406345354191

669 0.00136179187611381

670 0.00133030026081719

671 0.00130009688575679

672 0.00126989351069639

673 0.00123979155659011

674 0.00121212136851751

675 0.00118445118044491

676 0.00115678099237231

677 0.00113076961776973

678 0.00110545785424311

679 0.00108014609071649

680 0.00105541314675601

681 0.00103167815771806

682 0.00100794316868010

683 0.000984292312312752

684 0.000963249491200020

685 0.000942206670087288

686 0.000921163848974556

687 0.000900357785327965

688 0.000879655207538863

689 0.000858952629749762

690 0.000838808216055337

691 0.000819652262323675

692 0.000800496308592014

693 0.000781370634886208

694 0.000763361864755102

695 0.000745353094623995

696 0.000727344324492889

697 0.000709948256750336

698 0.000692824423836962

699 0.000675700590923587

700 0.000659336144382113

C.4   RC.txt

400 323.048571300000 1738.13783900000

401 325.762536100000 1735.04469000000

402 327.132648700000 1733.78101300000

403 329.206018300000 1731.55570800000

404 331.226166500000 1730.51335800000

405 334.258387300000 1728.72983100000

406 337.647824000000 1727.65231300000

407 341.016699100000 1729.14011300000

408 344.387309800000 1728.37588600000

409 347.689919300000 1729.79315500000

```
410 351.381655700000 1731.52270500000
411 355.557078800000 1733.71543500000
412 358.529940700000 1736.26703000000
413 362.657147700000 1739.28839200000
414 365.994404700000 1743.01289200000
415 368.890657700000 1746.73134500000
416 372.246916800000 1750.38152100000
417 375.131603500000 1753.42867500000
418 376.969329300000 1756.82832500000
419 379.496592300000 1760.34664900000
420 381.212953000000 1762.65862100000
421 382.770201500000 1765.23984400000
422 384.330925600000 1767.65642500000
423 386.402248500000 1769.75075900000
424 387.361437600000 1771.90363900000
425 389.277727200000 1773.51204400000
426 390.989628000000 1774.89088500000
427 392.528528600000 1777.15157000000
428 394.451906000000 1779.29410700000
429 397.639260300000 1782.29856900000
430 400.643123600000 1785.17347300000
431 403.481140700000 1788.97094600000
432 406.848733400000 1793.98714900000
433 410.923491000000 1799.43183700000
434 414.819051000000 1805.70448000000
435 418.356954700000 1812.44117000000
436 422.475376600000 1819.55915900000
437 426.273271900000 1827.57689200000
```

```
438  429.597438300000  1835.67651400000
439  432.441784500000  1844.64825700000
440  434.986636800000  1852.51104700000
441  436.457231200000  1860.89008600000
442  437.523626400000  1869.26779100000
443  437.262294100000  1876.86224300000
444  435.122135100000  1884.27588100000
445  432.206973800000  1891.05807900000
446  427.737881900000  1897.15073000000
447  423.109105700000  1901.95457400000
448  416.403726000000  1906.99888000000
449  408.780726100000  1910.20682600000
450  400.776553700000  1912.94079900000
451  394.288967200000  1914.07585000000
452  386.254112400000  1914.81673300000
453  378.909481400000  1914.43549700000
454  371.738303100000  1914.09205500000
455  365.353263400000  1911.93131600000
456  359.551560900000  1910.40941500000
457  355.181623400000  1908.65243100000
458  350.789747200000  1906.49726800000
459  347.208452200000  1904.13880900000
460  343.090624200000  1902.89780400000
461  339.584708900000  1900.94062800000
462  336.669712000000  1899.20929500000
463  333.207248600000  1897.86320900000
464  329.751798000000  1897.26721200000
465  326.369864500000  1895.89256000000
```

466 323.707236600000 1894.25731400000

467 320.271044200000 1892.83230300000

468 317.222977800000 1890.85776900000

469 314.314376400000 1889.06110200000

470 311.672710000000 1886.65109900000

471 308.735999900000 1884.44776400000

472 306.615746700000 1881.47452000000

473 304.894090100000 1878.87893300000

474 304.350727300000 1874.79354800000

475 302.819830000000 1872.87013100000

476 302.236073600000 1870.13109900000

477 303.569697900000 1866.50973500000

478 304.090699700000 1864.01190200000

479 304.596198100000 1862.63944700000

480 304.884909600000 1862.10429200000

481 308.223232000000 1860.03025200000

482 308.657265500000 1860.58257800000

483 310.552179400000 1860.44794300000

484 311.640974100000 1861.13236600000

485 311.489624100000 1863.14352800000

486 312.176076200000 1864.48599100000

487 312.476447400000 1865.96892400000

488 311.083678400000 1869.23720900000

489 311.382428100000 1871.13439200000

490 309.752508500000 1873.80202700000

491 308.169557500000 1876.04974400000

492 306.012219100000 1878.75589400000

493 303.895187000000 1881.59050700000

```
494  300.913457000000  1883.72734400000
495  297.799585200000  1886.79403900000
496  294.583895500000  1889.67684200000
497  291.577704800000  1892.25069100000
498  287.926302000000  1894.22145700000
499  284.288287100000  1896.48510500000
500  277.444552100000  1900.67149700000
501  273.139684300000  1902.45593400000
502  268.756260900000  1903.93574900000
503  261.861685800000  1907.19984900000
504  255.479339300000  1909.47997000000
505  248.083989500000  1911.33115000000
506  242.822723200000  1912.56564300000
507  235.738715100000  1913.60992400000
508  228.348145100000  1914.94143400000
509  220.294976300000  1916.37314700000
510  212.460577600000  1916.98027300000
511  205.926938300000  1916.93016200000
512  197.639402900000  1917.12746700000
513  190.714026900000  1915.91028000000
514  182.368637000000  1915.99794900000
515  175.838871100000  1914.47384900000
516  168.520506900000  1913.30210000000
517  162.938688300000  1910.86659300000
518  154.125276800000  1911.05543000000
519  148.408815800000  1908.18913000000
520  141.766167000000  1906.14408500000
521  138.051662300000  1902.75964200000
```

```
522  131.128818400000  1900.88961900000
523  125.763676500000  1897.36411200000
524  120.624416400000  1893.90440300000
525  117.086621100000  1890.40503800000
526  111.425071100000  1887.61248200000
527  107.717498100000  1883.81130800000
528  103.530260300000  1880.58249300000
529  99.6274555900000  1876.86215500000
530  95.5962816800000  1872.72376000000
531  93.1051953200000  1868.57886500000
532  90.6394230400000  1864.30693100000
533  86.6781764600000  1861.27646200000
534  85.0892268300000  1856.54557000000
535  80.3409877600000  1853.70613500000
536  78.8713953700000  1848.96882100000
537  76.7312203700000  1844.61315400000
538  74.9034467700000  1840.58438500000
539  71.6225253600000  1837.14615600000
540  70.5446811800000  1832.19650700000
541  68.9861625700000  1828.28017400000
542  68.5840691800000  1823.05058800000
543  66.4339315700000  1819.30190000000
544  63.5959436300000  1815.79454500000
545  64.0939030700000  1810.38054700000
546  61.1574776600000  1806.88964200000
547  60.1213968200000  1802.95921600000
548  57.8878420500000  1799.42565400000
549  58.2386136000000  1793.78127300000
```

```
550  58.1171228700000  1789.46309400000
551  56.4787832500000  1785.85216800000
552  54.7093878600000  1781.79125100000
553  54.3973295800000  1777.27366900000
554  52.9672204700000  1773.41355000000
555  53.6321293900000  1768.43609500000
556  51.7555159900000  1764.60486200000
557  51.4831469700000  1760.21964100000
558  50.5265202000000  1756.32330100000
559  52.3417106900000  1750.39803300000
560  51.0103844900000  1746.61901900000
561  51.0839546300000  1742.19699800000
562  51.2150589900000  1737.27024800000
563  52.1710067600000  1732.74797100000
564  51.7205128500000  1728.62348400000
565  52.1838285400000  1724.21069700000
566  53.5623984500000  1719.53368200000
567  54.6676849500000  1714.99777500000
568  53.9300568800000  1711.72540100000
569  55.6682533600000  1707.28991000000
570  55.6186025900000  1704.43847000000
571  57.7988045700000  1699.88772000000
572  59.4137390000000  1695.60276300000
573  60.0297085100000  1692.23636700000
574  61.8972709300000  1687.48182900000
575  61.6044924200000  1685.36965700000
576  62.0125462200000  1681.95490500000
577  63.4557871500000  1679.09285300000
```

```
578  66.0752298700000  1674.42440100000
579  66.1739520400000  1671.67886100000
580  66.3490124600000  1669.61036000000
581  67.5560958500000  1666.31872400000
582  67.7861225500000  1663.88584300000
583  68.8318901200000  1660.49873300000
584  68.7159127000000  1658.47231500000
585  69.2846221700000  1655.52063700000
586  69.2470132700000  1653.09055600000
587  69.9078785300000  1650.24394100000
588  70.3768684800000  1647.35000700000
589  70.5112813900000  1644.79927600000
590  70.3289198400000  1642.35809700000
591  70.2516249900000  1639.54784900000
592  70.4493713700000  1636.32065300000
593  69.0557284900000  1634.35195700000
594  69.7628453500000  1630.66905900000
595  69.8149576400000  1627.28603200000
596  69.9622939000000  1623.85331200000
597  69.1831382000000  1620.36588700000
598  68.8737507100000  1617.14106100000
599  69.2250125400000  1613.26830200000
600  70.6442583500000  1608.25828600000
601  70.0107309500000  1605.16831000000
602  71.1477430200000  1600.71078000000
603  71.3690924200000  1596.87526600000
604  73.6290032600000  1591.69728000000
605  74.3486303100000  1588.03977400000
```

```
606  76.4877863900000  1583.73800000000
607  77.7136463800000  1580.23396400000
608  80.3297704800000  1576.21828500000
609  81.2198900700000  1573.94283000000
610  84.2598516300000  1569.76493600000
611  86.7909002400000  1566.67205300000
612  88.6405322800000  1564.70930900000
613  91.0420572000000  1562.59231500000
614  92.9702884900000  1560.69040300000
615  95.2442063600000  1559.06330100000
616  97.1712433600000  1557.83155900000
617  98.5719703400000  1557.04823500000
618  100.869363800000  1555.15850800000
619  101.996403400000  1554.82761800000
620  102.965600800000  1553.89291000000
621  103.416956900000  1553.51758400000
622  104.990096300000  1552.08112600000
623  105.988551200000  1551.12116900000
624  105.891771100000  1551.05336400000
625  106.244980700000  1549.98662700000
626  106.668782400000  1549.17554700000
627  105.997828500000  1548.91001600000
628  105.686501500000  1547.98825300000
629  105.122176800000  1547.26166400000
630  104.846818000000  1545.47170200000
631  104.659165300000  1543.49430000000
632  102.920253100000  1541.71061000000
633  101.523004800000  1540.37462400000
```

```
634  99.9488993300000  1538.01728000000
635  98.4920780000000  1535.20113200000
636  96.1797540300000  1532.24881100000
637  93.9894681700000  1528.87780200000
638  93.1402907200000  1523.93209600000
639  90.8556727200000  1519.13940200000
640  88.6829067400000  1514.00810900000
641  86.9390245400000  1508.32239400000
642  85.2805152600000  1501.63120800000
643  83.5818762000000  1495.58301700000
644  82.8968140300000  1487.94589300000
645  82.5618907100000  1479.87009100000
646  82.3637628100000  1471.55086700000
647  82.4653872800000  1463.59832700000
648  83.6153092600000  1453.85826100000
649  85.9843818200000  1443.71428800000
650  86.6046823900000  1435.44709300000
651  89.2591148300000  1426.02550900000
652  93.2395743400000  1416.13464600000
653  97.4933528400000  1407.40503800000
654  101.777633200000  1398.76210800000
655  107.769628900000  1390.34618000000
656  113.963097500000  1383.99814700000
657  119.965870900000  1378.59597100000
658  127.742413400000  1374.63008000000
659  134.669229200000  1372.15307000000
660  143.679763300000  1371.17632700000
661  151.634219300000  1372.34689300000
```

```
662  159.818671100000  1375.03420900000
663  168.725291200000  1379.89499700000
664  176.981549500000  1386.07710800000
665  185.965542300000  1394.30287000000
666  195.347131900000  1403.84082500000
667  203.959085800000  1415.76059300000
668  213.580806500000  1429.42329400000
669  222.926286500000  1445.01825800000
670  233.023737100000  1461.28410200000
671  243.501217700000  1480.23424300000
672  253.487715400000  1501.26957100000
673  264.588317900000  1523.27258100000
674  275.908045300000  1547.40371800000
675  287.644069900000  1572.32981400000
676  298.104585800000  1598.42921400000
677  308.026791000000  1624.08605200000
678  317.359675600000  1649.76823500000
679  325.832064300000  1674.16726300000
680  331.812085100000  1699.92032700000
681  336.973126000000  1723.16345700000
682  338.434576800000  1746.75064200000
683  337.688375600000  1770.37846500000
684  333.446364000000  1790.64865400000
685  324.657727700000  1810.87392300000
686  310.429705500000  1828.19551400000
687  291.316293200000  1842.68714200000
688  269.326963800000  1853.08267900000
689  243.717791600000  1858.96646800000
```

690 218.144538100000 1861.41029000000

691 192.578546800000 1860.23211100000

692 169.460789700000 1854.83562400000

693 146.621696000000 1848.22758600000

694 127.290104800000 1839.42148900000

695 111.185298300000 1827.89091600000

696 94.9696793800000 1818.78245700000

697 84.7989791700000 1806.28680200000

698 71.6465230600000 1796.19179000000

699 62.0394293100000 1784.64494100000

700 56.1361669400000 1772.16820100000

References

[1] BP, "Energy outlook 2035", bp.com/energyoutlook, 2014.

[2] United States Energy Information Administration, "Annual energy review", "http://www.eia.gov/totalenergy/data/monthly/pdf/sec1_3.pdf", 2013.

[3] IPCC, *Climate Change 2007: Impacts, Adaptation and Vulnerability. Contribution of Working Group II to the Fourth Assessment Report of the Intergovernmental Panel on Climate Change*, Cambridge University Press, Cambridge, UK, 2007.

[4] J. Ferrell and V. Sarisky-Reed, "National Algal Biofuels Technology Roadmap", Tech. Rep. DOE/EE-0332, Department of Energy, Office of Energy Efficiency and Renewable Energy, Biomass Program, Maryland, Washington DC, 2010.

[5] Y. Chisti, "Biodiesel from microalgae", *Biotechnology Advances*, vol. 25, no. 3, pp. 294 – 306, 2007.

[6] A.J. Liska, H. Yang, M. Milner, S. Goddard, H. Blanco-Canqui, M.P. Pelton, X.X. Fang, H. Zhu, and A.E. Suyker, "Biofuels from crop residue can reduce soil carbon and increase CO_2 emissions", *Nature Climate Change*, vol. 4, pp. 398–401, 2014.

[7] X. Liu, B. Saydah, P. Eranki, L.M. Colosi, B.G. Mitchell, J. Rhodes, and A.F. Clarens, "Pilot-scale data provide enhanced estimates of the life cycle energy and emissions profile of algae biofuels produced via hydrothermal liquefaction", *Bioresource Technology*, vol. 148, pp. 163 – 171, 2013.

[8] L. Pilon, H. Berberoğlu, and R. Kandilian, "Radiation transfer in photobiological carbon dioxide fixation and fuel production by microalgae", *Journal of Quantitative Spectroscopy and Radiative Transfer*, vol. 112, no. 17, pp. 2639–2660, 2011.

[9] A. Carvalho, S. Silva, J. Baptista, and F. Malcata, "Light requirements in microalgal photobioreactors: an overview of biophotonic aspects", *Applied Microbiology and Biotechnology*, vol. 89, pp. 1275–1288, 2011.

[10] B. Ke, *Photosynthesis: Photobiochemistry and Photobiophysics*, Advances in Photosynthesis. Kluwer Academic Publishers, Dordrecht, The Netherlands, 2001.

[11] I. Akkerman, M. Janssen, J. Rocha, and R.H. Wijffels, "Photobiological hydrogen production: photochemical efficiency and bioreactor design", *International Journal of Hydrogen Energy*, vol. 27, no. 11–12, pp. 1195 – 1208, 2002.

[12] H. Berberoğlu, J. Jay, and L. Pilon, "Effect of nutrient media on photobiological hydrogen production by anabaena variabilis ATCC 29413", *International Journal of Hydrogen Energy*, vol. 33, no. 4, pp. 1172–1184, 2008.

[13] K. Skjånes, P. Lindblad, and J. Muller, "Bio CO_2 - a multidisciplinary, biological approach using solar energy to capture CO_2 while producing H_2 and high value products", *Biomolecular Engineering*, vol. 24, no. 4, pp. 405–413, 2007.

[14] P. Hodgson, R. Henderson, J. Sargent, and J. Leftley, "Patterns of variation in the lipid class and fatty acid composition of *Nannochloropsis oculata* (eustigmatophyceae) during batch culture", *Journal of Applied Phycology*, vol. 3, pp. 169–181, 1991.

[15] L. Rodolfi, G. Chini Zittelli, N. Bassi, G. Padovani, N. Biondi, G. Bonini, and M. R. Tredici, "Microalgae for oil: Strain selection, induction of lipid synthesis and outdoor mass cultivation in a low-cost photobioreactor", *Biotechnology and Bioengineering*, vol. 102, no. 1, pp. 100–112, 2009.

[16] E.D. Frank, A. Elgowainy, J. Han, and Z. Wang, "Life cycle comparison of hydrothermal liquefaction and lipid extraction pathways to renewable diesel from algae", *Mitigation and Adaptation Strategies for Global Change*, vol. 18, no. 1, pp. 137–158, 2013.

[17] P. J. le B. Williams and L.M.L. Laurens, "Microalgae as biodiesel and biomass feedstocks: Review and analysis of the biochemistry, energetics and economics", *Energy Environmental Science*, vol. 3, pp. 554–590, 2010.

[18] J.R. Benemann, J.C. Weissman, B.L. Koopman, and W.J. Oswald, "Energy production by microbial photosynthesis", *Nature*, vol. 268, pp. 19–23, 1977.

[19] E. Molina Grima, J. M. Fernandez Sevilla, J. A. Sanchez Perez, and F. Garcia Camacho, "A study on simultaneous photolimitation and photoinhibition in dense microalgal cultures taking into account incident and averaged irradiances", *Journal of Biotechnology*, vol. 45, no. 1, pp. 59 – 69, 1996.

[20] Israel Seambiotic Ltd., "Open ponds", http://www.seambiotic.com/.

[21] Arizona state university, "Vertical flat-plate photobioreactors", http://biofuels.asu.edu/biomaterials.shtml.

[22] Y. Chisti, "Constraints to commercialization of algal fuels", *Journal of Biotechnology*, vol. 167, no. 3, pp. 201–214, 2013.

[23] C.S. Jones and S.P. Mayfield, "Algae biofuels: versatility for the future of bioenergy", *Current Opinion in Biotechnology*, vol. 23, no. 3, pp. 346–351, 2012.

[24] Y. Chisti, "Raceways-based production of algal crude oil", in *Microalgal Biotechnology: Potential and Production*, C. Posten and C. Walter, Eds., pp. 113–144. De Gruyter, Berlin, Germany, 2012.

[25] E. Stephens, I.L. Ross, Z. King, J.H. Mussgnug, O. Kruse, C. Posten, M.A. Borowitzka, and B. Hankamer, "An economic and technical evaluation of microalgal biofuels", *Nature Biotechnology*, vol. 28, no. 2, pp. 126–128, 2010.

[26] H.C.P. Matthijs, H. Balke, U.M. van Hes, B.M.A. Kroon, L.R. Mur, and R.A. Binot, "Application of light-emitting diodes in bioreactors: Flashing light effects and energy economy in algal culture *Chlorella pyrenoidosa*", *Biotechnology and Bioengineering*, vol. 50, no. 1, pp. 98–107, 1996.

[27] I. Baroli and A. Melis, "Photoinhibition and repair in *Dunaliella salina* acclimated to different growth irradiances", *Planta*, vol. 198, pp. 640–646, 1996.

[28] J. Neidhardt, J. R. Benemann, L. Zhang, and A. Melis, "Photosystem-II repair and chloroplast recovery from irradiance stress: relationship between chronic photoinhibition, light-harvesting chlorophyll antenna size and photosynthetic productivity in *Dunaliella salina* (green algae)", *Photosynthesis Research*, vol. 56, pp. 175–184, 1998.

[29] O. Björkman, "Responses to different quantum flux densities", in *Physiological Plant Ecology I: Responses to the Physical Environment*, O.L. Lange, P.S. Nobel, C.B. Osmond, and H. Ziegler, Eds., vol. 12A of *Encyclopedia of Plant Physiology New Series*, pp. 57–107. Springer-Verlag, Berlin, 1981.

[30] Z. Dubinsky and N. Stambler, "Photoacclimation processes in phytoplankton: mechanisms, consequences, and applications", *Aquatic Microbial Ecology*, vol. 56, pp. 163–176, 2000.

[31] L. M. Lubián, O. Montero, I. Moreno-Garrido, I. E. Huertas, C. Sobrino, M. Gonzalez del Valle, and G. Pares, "*Nannochloropsis* (eustigmatophyceae) as source of commercially valuable pigments", *Journal of Applied Phycology*, vol. 12, pp. 249–255, 2000.

[32] M.-P. Gentile and H. W. Blanch, "Physiology and xanthophyll cycle activity of *Nannochloropsis gaditana*", *Biotechnology and Bioengineering*, vol. 75, no. 1, pp. 1–12, 2001.

[33] Z. Cohen, *Chemicals from Microalgae*, Taylor & Francis, London, UK, 1999.

[34] T. Fisher, J. Minnaard, and Z. Dubinsky, "Photoacclimation in the marine alga *Nannochloropsis* sp. (eustigmatophyte): a kinetic study", *Journal of Plankton Research*, vol. 18, no. 10, pp. 1797–1818, 1996.

[35] M. Jonasz and G. Fournier, *Light Scattering By Particles In Water: Theoretical and Experimental Foundations*, Academic Press, San Diego, CA, 2007.

[36] N. Zou and A. Richmond, "Light-path length and population density in photoacclimation of *Nannochloropsis sp.* (eustigmatophyceae)", *Journal of Applied Phycology*, vol. 12, pp. 349–354, 2000.

[37] M.F. Modest, *Radiative Heat Transfer*, Academic Press, San Diego, CA, 2003.

[38] E. Lee, R.-L. Heng, and L. Pilon, "Spectral optical properties of selected photosynthetic microalgae producing biofuels", *Journal of Quantitative Spectroscopy and Radiative Transfer*, vol. 114, pp. 122–135, 2013.

[39] G. Van Vooren, F. Le Grand, J. Legrand, S. Cuine, G. Peltier, and J. Pruvost, "Investigation of fatty acids accumulation in *Nannochloropsis oculata* for biodiesel application", *Bioresource Technology*, vol. 124, pp. 421–432, 2012.

[40] R. R. Bidigare, R. C. Smith, K. S. Baker, and J. Marra, "Oceanic primary production estimates from measurements of spectral irradiance and pigment concentrations", *Global Biogeochemical Cycles*, vol. 1, no. 3, pp. 171–186, 1987.

[41] L. Pottier, J. Pruvost, J. Deremetz, J.F. Cornet, J. Legrand, and C.G. Dussap, "A fully predictive model for one-dimensional light attenuation by *Chlamydomonas reinhardtii* in a torus photobioreactor", *Biotechnology and Bioengineering*, vol. 91, no. 5, pp. 569–582, 2005.

[42] R. R. Bidigare, M. E. E. Ondrusek, J. H. H. Morrow, and D. A. A. Kiefer, "*In-vivo* absorption properties of algal pigments", *Proceedings of the SPIE*, vol. 1302, pp. 290–302, 1990.

[43] A. A. Gitelson, Y. A. Grits, D. Etzion, Z. Ning, and A. Richmond, "Optical properties of *Nannochloropsis sp.* and their application to remote estimation of cell mass", *Biotechnology and Bioengineering*, vol. 69, no. 5, pp. 516–525, 2000.

[44] R . J. Davies-Colley, R. D. Pridmore, and J . E. Hewitt, "Optical properties of some freshwater phytoplanktonic algae", *Hydrobiologia*, vol. 133, no. 2, pp. 165–178, 1986.

[45] H. Berberoğlu, L. Pilon, and A. Melis, "Radiation characteristics of *Chlamydomonas reinhardtii* CC125 and its truncated chlorophyll antenna transformants *tla1, tlaX* and *tla1-CW+*", *International Journal of Hydrogen Energy*, vol. 33, no. 22, pp. 6467–6483, 2008.

[46] X. Ma, J.Q. Lu, R.S. Brock, K.M. Jacobs, and X.-H. Hu, "Determination of complex refractive index of polystyrene microspheres from 370 to 1610 nm", *Physics in Medicine and Biology*, vol. 48, no. 24, pp. 4165–4172, 2003.

[47] O. Zhernovaya, O. Sydoruk, V. Tuchin, and A. Douplik, "The refractive index of human hemoglobin in the visible range", *Physics in Medicine and Biology*, vol. 56, no. 13, pp. 4013–4021, 2011.

[48] P. Charbonneau, "Genetic algorithms in astronomy and astrophysics", *The Astrophysical Journal Supplement Series*, vol. 101, pp. 309–334, 1995.

[49] A.R. Wellburn, "The spectral determination of chlorophyll *a* and chlorophyll *b*, as well as total carotenoids, using various solvents with spectrophotometers of different resolution", *Journal of Plant Physiology*, vol. 144, no. 3, pp. 307–313, 1994.

[50] J.D.H. Strickland and T.R. Parsons, *A Practical Handbook of Seawater Analysis: Pigment Analysis*, Bulletin of Fisheries Research Board of Canada. Fisheries Research Board of Canada, 1968.

[51] R.A. Andersen, *Algal Culturing Techniques*, Elsevier/Academic Press, San Diego, CA, 2005.

[52] H. Berberoğlu, P. S. Gomez, and L. Pilon, "Radiation characteristics of *Botryococcus braunii, Chlorococcum littorale*, and *Chlorella sp.* used for fixation and biofuel production", *Journal of Quantitative Spectroscopy and Radiative Transfer*, vol. 110, no. 17, pp. 1879–1893, 2009.

[53] T.R. Parsons, K. Stephens, and J.D.H. Strickland, "On the chemical composition of eleven species of marine phytoplanktons", *Journal of Fisheries Research Board of Canada*, vol. 18, pp. 1001–1016, 1961.

[54] D. Simionato, E. Sforza, E. C. Carpinelli, A. Bertucco, G. M. Giacometti, and T. Morosinotto, "Acclimation of *Nannochloropsis gaditana* to different illumination regimes: Effects on lipids accumulation", *Bioresource Technology*, vol. 102, no. 10, pp. 6026 – 6032, 2011.

[55] K.N. Liou, Y. Takano, and P. Yang, "Light absorption and scattering by aggregates: Application to black carbon and snow grains", *Journal of Quantitative Spectroscopy and Radiative Transfer*, vol. 112, no. 10, pp. 1581–1594, 2011.

[56] C.M. Sorensen, "Light scattering by fractal aggregates: A review", *Aerosol Science and Technology*, vol. 35, no. 2, pp. 648–687, 2001.

[57] Y. Takano, K.N. Liou, M. Kahnert, and P. Yang, "The single-scattering properties of black carbon aggregates determined from the geometric-optics surface-wave approach and the T-matrix method", *Journal of Quantitative Spectroscopy and Radiative Transfer*, vol. 125, pp. 51–56, 2013.

[58] H. Kimura, L. Kolokolova, and I. Mann, "Optical properties of cometary dust", *Astronomy and Astrophysics*, vol. 407, no. 1, pp. L5–L8, 2003.

[59] T.J. Norman, C.D. Grant, D. Maganaand J.Z. Zhang, J. Liu, D. Cao, F. Bridges, and A. Van Buuren, "Near infrared optical absorption of gold nanoparticle aggregates", *The Journal of Physical Chemistry B*, vol. 106, no. 28, pp. 7005–7012, 2002.

[60] J. Guan, T.D. Waite, R. Amal, H. Bustamante, and R. Wukasch, "Rapid determination of fractal structure of bacterial assemblages in wastewater treatment: Implications to process optimisation", *Water Science and Technology*, vol. 38, no. 2, pp. 9–15, 1998.

[61] Q. Jiang and B. E. Logan, "Fractal dimensions of aggregates determined from steadstate size distribution", *Environmental Science and Technology*, vol. 25, no. 12, 1991.

[62] G.A. Jackson, R. Maffione, D.K. Costello, A.L. Alldredge, B.E. Logan, and H.G. Dam, "Particle size spectra between 1 μm and 1 cm at Monterey Bay determined using multiple instruments", *Deep Sea Research Part I: Oceanographic Research Papers*, vol. 44, no. 11, pp. 1739–1767, 1997.

[63] S. Friedlander and C. Sioutas, "Final report: Measurement of the "effective surface area of ultrafine and accumulation mode PM (pilot project)", Tech. Rep. R827352, United States Environmental Protection Agency, Los Angeles, CA, 2006.

[64] Electron and Agricultural Research Service Confocal Microscopy Laboratory, *Rime and Graupel*, United States Department of Agriculture, Beltsville, MD, 2006, http://emu.arsusda.gov/snowsite/rimegraupel/rg.html.

[65] Jet Propulsion Laboratory, *A 10 micron interplanetary dust collected in the stratosphere*, National Aeronautic and Space Administration, Pasadena, CA, 2003, http://stardust.jpl.nasa.gov/science/sd-particle.html#idp-s.

[66] F.D.A. Keene, *Clusters of roughly 30-nanometer gold nanoparticles imaged by transmission electron microscopy*, National Institute of Standards and Technology, Gaithersburg, MD, 2011, http://www.nist.gov/mml/biochemical/cluster-102511.cfm.

[67] J. Carr, *Micrococcus luteus 9757*, Centers for Disease Control and Prevention: Public Health Image Library, Atlanta, GA, 2007.

[68] L. Brennan and P. Owende, "Biofuels from microalgae: A review of technologies for production, processing, and extractions of biofuels and co-products", *Renewable and Sustainable Energy Reviews*, vol. 14, no. 2, pp. 557 – 577, 2010.

[69] C. Dayananda, R. Sarada, M. Usha Rani, T.R. Shamala, and G.A. Ravishankar, "Autotrophic cultivation of *Botryococcus braunii* for the production of hydrocarbons and exopolysaccharides in various media", *Biomass and Bioenergy*, vol. 31, no. 1, pp. 87–93, 2007.

[70] M. Demura, M. Ioki, M. Kawachi, N. Nakajima, and M. Watanabe, "Desiccation tolerance of *Botryococcus braunii* (trebouxiophyceae, chlorophyta) and extreme temperature tolerance of dehydrated cells", *Journal of Applied Phycology*, vol. 26, no. 1, pp. 49–53, 2014.

[71] K. C. Díaz Bayona and L. A. Garcés, "Effect of different media on exopolysaccharide and biomass production by the green microalga *Botryococcus braunii*", *Journal of Applied Phycology*, 2014, (in press).

[72] A. Souliés, J. Pruvost, J. Legrand, C. Castelain, and T.I. Burghelea, "Rheological properties of suspensions of the green microalga *Chlorella vulgaris* at various volume fractions", *Rheologica Acta*, vol. 52, no. 6, pp. 589–605, 2013.

[73] J-F. Cornet and C-G. Dussap, "A simple and reliable formula for assessment of maximum volumetric productivities in photobioreactors", *Biotechnology Progress*, vol. 25, no. 2, pp. 424–435, 2009.

[74] J. Pruvost and J.F. Cornet, "Knowledge models for the engineering and optimization of photobioreactors", in *Microalgal Biotechnology: Potential and Production*, C. Posten and C. Walter, Eds., pp. 181–224. De Gruyter, Berlin, Germany, 2012.

[75] H. Takache, J. Pruvost, and J.-F.Cornet, "Kinetic modeling of the photosynthetic growth of *Chlamydomonas reinhardtii* in a photobioreactor", *Biotechnology Progress*, vol. 28, no. 3, pp. 681–692, 2012.

[76] D. Stramski, A. Morel, and A. Bricaud, "Modeling the light attenuation and scattering by spherical phytoplanktonic cells: a retrieval of the bulk refractive index", *Applied Optics*, vol. 27, no. 19, pp. 3954–3956, Oct 1988.

[77] A. Quirantes and S. Bernard, "Light-scattering methods for modeling algal particles as a collection of coated and/or nonspherical scatterers", *Journal of Quantitative Spectroscopy and Radiative Transfer*, vol. 100, no. 1-3, pp. 315–324, 2006.

[78] H. Berberoğlu, J. Yin, and L. Pilon, "Light transfer in bubble sparged photobioreactors for H_2 production and CO_2 mitigation", *International Journal of Hydrogen Energy*, vol. 32, no. 13, pp. 2273–2285, 2007.

[79] R. J. Davies-Colley, "Optical properties and reflectance spectra of 3 shallow lakes obtained from a spectrophotometric study", *New Zealand Journal of Marine and Freshwater Research*, vol. 17, no. 4, pp. 445–459, 1983.

[80] D.W. Mackowski and M.I. Mishchenko, "A multiple sphere t-matrix fortran code for use on parallel computer clusters", *Journal of Quantitative Spectroscopy and Radiative Transfer*, vol. 112, no. 13, pp. 2182–2192, 2011.

[81] Y.-L. Xu, "Electromagnetic scattering by an aggregate of spheres: far field", *Applied Optics*, vol. 36, no. 36, pp. 9496–9508, 1997.

[82] M. F. Iskander, H. Y. Chen, and J. E. Penner, "Optical scattering and absorption by branched chains of aerosols", *Applied Optics*, vol. 28, no. 15, pp. 3083–3091, 1989.

[83] M. Kahnert, T. Nousiainen, and H. Lindqvist, "Review: Model particles in atmospheric optics", *Journal of Quantitative Spectroscopy and Radiative Transfer*, vol. 146, pp. 41–58, 2014.

[84] B.L. Drolen and C.L. Tien, "Absorption and scattering of agglomerated soot particulate", *Journal of Quantitative Spectroscopy and Radiative Transfer*, vol. 37, no. 5, pp. 433–448, 1987.

[85] E. Lee and L. Pilon, "Absorption and scattering by long and randomly oriented linear chains of spheres", *Journal of Optical Society of America A*, vol. 30, no. 9, pp. 1892–1900, 2013.

[86] T.L. Farias, Ü.Ö. Köylü, and M.G. Carvalho, "Effects of polydispersity of aggregates and primary particles on radiative properties of simulated soot", *Journal of Quantitative Spectroscopy and Radiative Transfer*, vol. 55, no. 3, pp. 357 – 371, 1996.

[87] C. M. Sorensen, J. Cai, and N. Lu, "Light-scattering measurements of monomer size, monomers per aggregate, and fractal dimension for soot aggregates in flames", *Applied Optics*, vol. 31, no. 30, pp. 6547–6557, 1992.

[88] Ü. Ö. Köylü, G.M. Faeth, T.L. Farias, and M.G. Carvalho, "Fractal and projected structure properties of soot aggregates", *Combustion and Flame*, vol. 100, no. 4, pp. 621–633, 1995.

[89] T. L. Farias, Ü. Ö. Köylü, and M. G. Carvalho, "Range of validity of the Rayleigh-Debye-Gans theory for optics of fractal aggregates", *Applied Optics*, vol. 35, no. 33, pp. 6560–6567, 1996.

[90] M. Lapuerta, F.J. Martos, and G. Martín-González, "Geometrical determination of the lacunarity of agglomerates with integer fractal dimension", *Journal of Colloid and Interface Science*, vol. 346, no. 1, pp. 23–31, 2010.

[91] J. Mroczka, M. Woźniak, and F.R.A. Onofri, "Algorithms and methods for analysis of the optical structure factor of fractal aggregates", *Metrology and Measurement Systems*, vol. 19, no. 3, pp. 459–470, 2012.

[92] M. Woźniak, F.R.A. Onofri, S. Barbosa, J. Yon, and J. Mroczka, "Comparison of methods to derive morphological parameters of multi-fractal samples of particle aggregates from TEM images", *Journal of Aerosol Science*, vol. 47, pp. 12–26, 2012.

[93] M.I. Mishchenko, L.D. Travis, and A.A. Lacis, *Scattering, Absorption, and Emission of Light by Small Particles*, Cambridge University Press, Cambridge, UK, 2002.

[94] D. W. Mackowski, "A simplified model to predict the effects of aggregation on the absorption properties of soot particles", *Journal of Quantitative Spectroscopy and Radiative Transfer*, vol. 100, no. 1–3, pp. 237–249, 2006.

[95] C.F. Bohren and D.R. Huffman, *Absorption and Scattering of Light by Small Particles*, Wiley, New York, NY, 1983.

[96] S. Manickavasagam and M. P. Mengüç, "Scattering matrix elements of fractal-like soot agglomerates", *Applied Optics*, vol. 36, no. 6, pp. 1337–1351, 1997.

[97] B. Yang and Ü. Ö. Köylü, "Soot processes in a strongly radiating turbulent flame from laser scattering/extinction experiments", *Journal of Quantitative Spectroscopy and Radiative Transfer*, vol. 93, no. 1-3, pp. 289–299, 2005.

[98] G. Wang and C.M. Sorensen, "Experimental test of the Rayleigh-Debye-Gans theory for light scattering by fractal aggregates", *Applied Optics*, vol. 41, no. 22, pp. 4645–4651, 2002.

[99] G. Bushell, "Forward light scattering to characterize structure of flocs composed of large particles", *Chemical Engineering Journal*, vol. 111, no. 23, pp. 145–149, 2005.

[100] F. Liu, C. Wong, D.R. Snelling, and G.J. Smallwood, "Investigation of absorption and scattering properties of soot aggregates of different fractal dimension at 532 nm using RDG and GMM", *Aerosol Science and Technology*, vol. 47, no. 12, pp. 1393–1405, 2013.

[101] F. Liu, D.R. Snelling, and G.J. Smallwood, "Effects of the fractal prefactor on the optical properties of fractal soot aggregates", in *ASME 2009 2nd Micro/Nanoscale Heat & Mass Transfer International Conference*, Shanghai, China, 2009, MNHMT2009-18473.

[102] M.A. Yurkin and A.G. Hoekstra, "The discrete dipole approximation: an overview and recent developments", *Journal of Quantitative Spectroscopy and Radiative Transfer*, vol. 106, pp. 558–589, 2007.

[103] L. Liu and M.I. Mishchenko, "Effects of aggregation on scattering and radiative properties of soot aerosols", *Journal of Geophysical Research: Atmospheres*, vol. 110, no. D11211, 2005.

[104] L. Liu and M. I. Mishchenko, "Scattering and radiative properties of complex soot and soot-containing aggregate particles", *Journal of Quantitative Spectroscopy and Radiative Transfer*, vol. 106, no. 1–3, pp. 262–273, 2007.

[105] L. Liu, M. I. Mishchenko, and W. P. Arnott, "A study of radiative properties of fractal soot aggregates using the superposition t-matrix method", *Journal of Quantitative Spectroscopy and Radiative Transfer*, vol. 109, no. 15, pp. 2656–2663, 2008.

[106] J.M. Dlugach, M.I. Mishchenko, and D.W. Mackowski, "Numerical simulations of single and multiple scattering by fractal ice clusters", *Journal of Quantitative Spectroscopy and Radiative Transfer*, vol. 112, no. 11, pp. 1864–1870, 2011.

[107] P. Latimer, "Experimental tests of a theoretical method for predicting light scattering by aggregates", *Applied Optics*, vol. 24, no. 19, pp. 3231–3239, 1985.

[108] C. Oh and C.M. Sorensen, "The effect of overlap between monomers on the determination of fractal cluster morphology", *Journal of Colloid and Interface Science*, vol. 193, no. 1, pp. 17–25, 1997.

[109] R.-L. Heng, K.C. Sy, and L. Pilon, "Absorption and scattering by bispheres, quadspheres, and circular rings of spheres and their equivalent coated spheres", *Journal of Optical Society of America A*, 2014, (under review).

[110] A. Bricaud, A.L. Bedhomme, and A. Morel, "Optical properties of diverse phytoplanktonic species: experimental results and theoretical interpretation", *Journal of Plankton Research*, vol. 10, no. 8, pp. 51–73, 2008.

[111] A. Morel and Y.H. Ahn, "Optics of heterotrophic nanoflagellates and ciliates: a tentative assessment of their scattering role in oceanic waters compared to those of bacterial and algal cells", *Journal of Marine Research*, vol. 49, pp. 177–202, 1991.

[112] K. Skorupski, J. Mroczka, T. Wriedt, and N. Riefler, "A fast and accurate implementation of tunable algorithms used for generation of fractal-like aggregate models", *Physica A: Statistical Mechanics and its Applications*, vol. 404, pp. 106–117, 2014.

[113] C. Mätzler, *MATLAB Functions for Mie Scattering and Absorption Version 2*, Institut f ur Angewandte Physik, Bern, Switzerland, 2002, Report No. 2002-11.

[114] R. Kandilian, E. Lee, and L. Pilon, "Radiation and optical properties of *Nannochloropsis oculata* grown under different irradiances and spectra", *Bioresource Technology*, vol. 137, pp. 63 – 73, 2013.

[115] R.-L. Heng and L. Pilon, "Time-dependent radiation characteristics of *Nannochloropsis oculata* during batch culture", *Journal of Quantitative Spectroscopy and Radiative Transfer*, vol. 144, pp. 154–163, 2014.

[116] E. Lee, J. Pruvost, X. He, R. Munipalli, and L. Pilon, "Design tool and guidelines for outdoor photobioreactors", *Chemical Engineering Science*, vol. 116, pp. 18–29, 2014.

[117] M.I. Mishchenko, *Electromagnetic Scattering By Particles and Particle Groups: An Introduction*, Cambridge University Press, New York, NY.

[118] M. Kerker, *The Scattering of Light, and Other Electromagnetic Radiation*, Academic Press, New York, NY, 1969.

[119] B.H.J. Mc Kellar and M.A. Box, "The scaling group of the radiative transfer equation", *Journal of the Atmospheric Sciences*, pp. 1063–1068, 1981.

[120] L.A. Dombrovski, J. Randrianalisoa, D. Baillis, and L. Pilon, "Use of Mie theory to analyze experimental data to identify infrared properties of fused quartz containing bubbles", *Applied Optics*, vol. 44, no. 33, pp. 7021–7031, 2005.

[121] M. Hammer, A.N. Yaroslavsky, and D. Schweitzer, "A scattering phase function for blood with physiological haematocrit", *Physics in medicine and biology*, vol. 46, no. 3, pp. 65–69, 2001.

[122] M. Friebel, A. Roggan, G. Mueller, and M. Meinke, "Determination of optical properties of human blood in the spectral range 250 to 1100 nm using Monte-Carlo simulations with hematocrit-dependent effective scattering phase functions", *Journal of Biomedical Optics*, vol. 11, no. 3, pp. 034021, 2006.

[123] V.I. Haltrin, "One-parameter two-term Henyey?Greenstein phase function for light scattering in seawater", *Applied Optics*, vol. 41, no. 6, pp. 1022–1028, 2002.

[124] C.D. Mobley, L.K. Sundman, and E. Boss, "Phase function effects on oceanic light fields", *Applied Optics*, vol. 41, no. 6, pp. 1035–1050, 2002.

[125] R. A. West, "Optical properties of aggregate particles whose outer diameter is comparable to the wavelength", *Applied Optics*, vol. 30, no. 36, pp. 5316–5324, 1991.

175

[126] D. W. Mackowski and M. I. Mishchenko, "Calculation of the T-matrix and the scattering matrix for ensembles of spheres", *Journal of Optical Society of America A*, vol. 13, no. 11, pp. 2266–2278, 1996.

[127] M.I. Mishchenko, D.W. Mackowski, and L.D. Travis, "Scattering of light by bispheres with touching and separated components", *Applied Optics*, vol. 34, no. 21, pp. 4589–4599, 1995.

[128] X. Chen, Q. Y. Goh, W. Tan, I. Hossain, W.N. Chen, and R. Lau, "Lumostatic strategy for microalgae cultivation utilizing image analysis and chlorophyll *a* content as design parameters", *Bioresource Technology*, vol. 102, no. 10, pp. 6005–6012, 2011.

[129] J. Dauchet, S. Blanco, J.F. Cornet, M. El Hafi, V. Eymet, and R. Fournier, "The practice of recent radiative transfer Monte Carlo advances and its contribution to the field of microorganisms cultivation in photobioreactors", *Journal of Quantitative Spectroscopy and Radiative Transfer*, vol. 128, pp. 52–59, 2013.

[130] B. Kong and R. D. Vigil, "Simulation of photosynthetically active radiation distribution in algal photobioreactors using a multidimensional spectral radiation model", *Bioresource Technology*, vol. 158, pp. 141–148, 2014.

[131] J.F. Cornet and J. Albiol, "Modeling photoheterotrophic growth kinetics of *Rhodospirillum rubrum* in rectangular photobioreactors", *Biotechnology Progress*, vol. 16, no. 2, pp. 199–207, 2000.

[132] F. G. Acien Fernandez, F. Garcia Camacho, J. A. Sanchez Perez, J. M. Fernandez Sevilla, and E. Molina Grima, "A model for light distribution and average solar irradiance inside outdoor tubular photobioreactors for the microalgal mass culture", *Biotechnology and Bioengineering*, vol. 55, no. 5, pp. 701–714, 1997.

[133] A. Sukenik, R. Levy, Y. Levy, P. Falkowski, and Z. Dubinsky, "Optimizing algal biomass production in an outdoor pond: a simulation model", *Journal of Applied Phycology*, vol. 3, pp. 191–201, 1991.

[134] B.D. Fernandes, G.M. Dragone, J.A. Teixeira, and A.A. Vicente, "Light regime characterization in an airlift photobioreactor for production of microalgae with high starch content", *Applied Biochemistry and Biotechnology*, vol. 161, no. 1-8, pp. 218–226, 2010.

[135] T.E. Murphy and H. Berberoğlu, "Effect of algae pigmentation on photobioreactor productivity and scale-up: A light transfer perspective", *Journal of Quantitative Spectroscopy and Radiative Transfer*, vol. 112, no. 18, pp. 2826 – 2834, 2011.

[136] S.Y. Chiu, C.Y. Kao, M.T. Tsai, S.C. Ong, C.H. Chen, and C.S. Lin, "Lipid accumulation and CO_2 utilization of *Nannochloropsis oculata* in response to CO_2 aeration", *Bioresource Technology*, vol. 100, no. 2, pp. 833–838, 2009.

[137] P. Spolaore, C. Joannis-Cassan, E. Duran, and A. Isambert, "Optimization of *Nannochloropsis oculata* growth using the response surface method", *Journal of Chemical Technology and Biotechnology*, vol. 81, no. 6, pp. 1049–1056, 2006.

[138] A. Converti, A. A. Casazza, E. Y. Ortiz, P. Perego, and M. Del Borghi, "Effect of temperature and nitrogen concentration on the growth and lipid content of *Nannochloropsis oculata* and *Chlorella vulgaris* for biodiesel production", *Chemical Engineering and Processing: Process Intensification*, vol. 48, no. 6, pp. 1146–1151, 2009.

[139] C.Y. Chen, K.L. Yeh, R. A., D.J. Lee, and J.S. Chang, "Cultivation, photobioreactor design and harvesting of microalgae for biodiesel production: A critical review", *Bioresource Technology*, vol. 102, no. 1, pp. 71–81, 2011.

[140] M. J. Barbosa, J. Hoogakker, and R. H. Wijffels, "Optimisation of cultivation parameters in photobioreactors for microalgae cultivation using the A-stat technique", *Biomolecular Engineering*, vol. 20, no. 4-6, pp. 115–123, 2003.

[141] M. Cuaresma, M. Janssen, E.J. van den End, C. Vlchezb, and R.H. Wijffels, "Luminostat operation: A tool to maximize microalgae photosynthetic efficiency in photobioreactors during the daily light cycle?", *Bioresource Technology*, vol. 102, no. 17, pp. 7871 – 7878, 2011.

[142] M. R. Melnicki, G. E. Pinchuk, E. A. Hill, L. A. Kucek, S. M. Stolyar, J. K. Fredrickson, A. E. Konopka, and A. S. Beliaev, "Feedback-controlled LED photobioreactor for photophysiological studies of cyanobacteria", *Bioresource Technology*, vol. 134, pp. 127–133, 2013.

[143] W.Y. Svrcek, D.P. Mahoney, and B.R. Young, *Advanced Topics in Classical Automatic Control*, pp. 131–146, John Wiley & Sons, Ltd, New York, NY, 2007.

[144] W.H. Press, S. A. Teukolsky, W. T. Vetterling, and B. P. Flannery, *Numerical Recipes: The Art of Scientific Computing*, Cambridge University Press, New York, NY, 2007.

[145] I. E. Huertas and L. M. Lubián, "Comparative study of dissolved inorganic carbon utilization and photosynthetic responses in *Nannochloris* (chlorophyceae) and *Nannochloropsis* (eustigmatophyceae) species", *Canadian Journal of Botany*, vol. 76, no. 6, pp. 1104–1108, 1998.

[146] J.M. Sandnes, T. Ringstad, D. Wenner, P.H. Heyerdahl, T. Kllqvist, and H.R. Gislerd, "Real-time monitoring and automatic density control of large-scale microalgal cultures using near infrared (NIR) optical density sensors", *Journal of Biotechnology*, vol. 122, no. 2, pp. 209–215, 2006.

[147] J.-F. Cornet, "Calculation of optimal design and ideal productivities of volumetrically lightened photobioreactors using the constructal approach", *Chemical Engineering Science*, vol. 65, no. 2, pp. 985–998, 2010.

[148] G. Olivieri, P. Salatino, and A. Marzocchella, "Advances in photobioreactors for intensive microalgal production: configurations, operating strategies and applications", *Journal of Chemical Technology & Biotechnology*, vol. 89, no. 2, pp. 178–195, 2014.

[149] Q. Hu, M. Sommerfeld, E. Jarvis, M. Ghirardi, M. Posewitz, M. Seibert, and A. Darzins, "Microalgal triacylglycerols as feedstocks for biofuel production: perspectives and advances", *The Plant Journal*, vol. 54, no. 4, pp. 621–639, 2008.

[150] D. Pal, I. Khozin-Goldberg, Z. Cohen, and S. Boussiba, "The effect of light, salinity, and nitrogen availability on lipid production by *Nannochloropsis sp.*", *Applied Microbiology and Biotechnology*, vol. 90, no. 4, pp. 1429–1441, 2011.

[151] J. Pruvost, G. Van Vooren, G. Cogne, and J. Legrand, "Investigation of biomass and lipids production with *Neochloris oleoabundans* in photobioreactor", *Bioresource Technology*, vol. 100, no. 23, pp. 5988–5995, 2009.

[152] G. Breuer, P. P. Lamers, D.E. Martens, R.B. Draaisma, and R.H. Wijffels, "Effect of light intensity, pH, and temperature on triacylglycerol (TAG) accumulation induced by nitrogen starvation in *Scenedesmus obliquus*", *Bioresource Technology*, vol. 143, pp. 1–9, 2013.

[153] C. Adams, V. Godfrey, B. Wahlen, L. Seefeldt, and B. Bugbee, "Understanding precision nitrogen stress to optimize the growth and lipid content tradeoff in oleaginous green microalgae", *Bioresource Technology*, vol. 131, no. 1, pp. 188–194, 2013.

[154] M.R. Heath, K. Richardson, and T. Kirboe, "Optical assessment of phytoplankton nutrient depletion", *Journal of Plankton Research*, vol. 12, no. 2, pp. 381–396, 1990.

[155] K.J. Flynn, K. Davidson, and A.J. Cunningham, "Relations between carbon and nitrogen during growth of *Nannochloropsis oculata* (droop) Hibberd under continuous illumination", *New Phytologist*, vol. 125, no. 4, pp. 717–722, 1993.

[156] L. Oeschger and C. Posten, "Construction and assessment parameters of photobioreactors", in *Microalgal Biotechnology: Potential and Production*, C. Posten and C. Walter, Eds., pp. 225–236. De Gruyter, Berlin, Germany, 2012.

[157] A.E. Cassano, C.A. Martin, R.J. Brandi, and O.M. Alfano, "Photoreactor analysis and design: Fundamentals and applications", *Industrial & Engineering Chemistry Research*, vol. 34, no. 7, pp. 2155–2201, 1995.

[158] H. Takache, G. Christophe, J.-F.Cornet, and J. Pruvost, "Experimental and theoretical assessment of maximum productivities for the microalgae *Chlamydomonas reinhardtii* in two different geometries of photobioreactors", *Biotechnology Progress*, vol. 26, no. 2, pp. 431–440, 2010.

[159] N.B. Nelson, B.B. Prezelinl, and R.R. Bidigare, "Phytoplankton light absorption and the package effect in California coastal waters", *Marine Ecology Progress Series*, vol. 94, pp. 217–227, 1993.

[160] A. Bricaud, H. Claustre, J. Ras, and K. Oubelkheir, "Natural variability of phytoplanktonic absorption in oceanic waters: Influence of the size structure of algal populations", *Journal of Geophysical Research*, vol. 109, no. C11, pp. 1947–1960, 2004.

[161] W.P. Bissett, J.S. Patch, K.L. Carder, and Z. Lee, "Pigment packaging and chlorophyll a-specific absorption in high-light oceanic waters", *Limnology and Oceanography*, vol. 42, no. 5, pp. 961–968, 1997.

[162] J.A. Berges, D.J. Franklin, and P.J. Harrison, "Evolution of an artificial seawater medium: Improvements in enriched seawater, artificial water over the last two decades", *Journal of Phycology*, vol. 37, no. 6, pp. 1138–1145, 2001.

[163] R.J. Ritchie, "Consistent sets of spectrophotometric chlorophyll equations for acetone, methanol and ethanol solvents", *Photosynthesis Research*, vol. 89, no. 1, pp. 27–41, 2006.